Optimization Based Analysis and Operation of Complex Nonlinear Energy Systems

Thesis for the degree
"Doctor of the Hungarian Academy of Sciences"

Attila Magyar

Department of Electrical Engineering and Information Systems,
University of Pannonia
Veszprém
2022

Acknowledgements

First of all, I would like to express my gratitude to Prof. Katalin M. Hangos, professor at the Department of Electrical Engineering and Information Systems of the Faculty of Information Technology, University of Pannonia (PE MIK) for the joint work on the topic of the thesis, and for her continuous encouragement and support to remain in the scientific field after obtaining my PhD. I am also grateful to Attila Fodor, the head of the Department of Electrical Engineering and Information Systems for continuously encouraging me to write my dissertation. Next, let me thank the joint work with all the members of the Electical Energy Systems Research Laboratory, it is a great pleasure leading this research group. I thank Prof. Ferenc Hartung, former dean of the Faculty of Information Technology for all his support and especially for providing us an excellent and undisturbed research environment in the institute. Many thanks to the administrative staff of PE MIK, especially to Szilvia Schmidt-Lényi for all her help through the years.

I'd like to thank all my co-authors not mentioned above (in alphabetical order): István Gusztáv Balázs, Dr. Attila Göllei, Dr. Péter Görbe, Márton Greber, György Károlyi, Prof. Lőrinc Márton, Dr. László Richárd Neukirchner, Prof. Dénes Petz, Dr. Anna Ibolya Pózna, Dr. László Ruppert and Prof. Gábor Szederkényi for sharing some interest in the topics I was working on, and for making essential contributions to the joint results.

I'm also grateful to my wife, Edina for all her patience and support, especially during thesis writing.

Finally, the financial support of the following institutions, grants and scholarships is also gratefully acknowledged. The Hungarian Scientific Research Fund (OTKA) through grants no. F046223 (Analysis based control of nonlinear dynamical systems), K67625 (Control and diagnosis of nonlinear systems based on first engineering principles), SNN120422 (Measurement based temperature dependency analysis of electrochemical energy systems), K131501 (Analysis and optimization of complex technological systems with energetic applications) and the Bolyai János Research Scholarship of the Hungarian Academy of Sciences: 2015-2018, and 2019-2022.

Contents

Notations

Generally used notations

$\mathbb{R}$	the set of real numbers
$\mathbb{Z}$	the set of integer numbers
$\mathbb{C}$	the set of complex numbers
$\mathbb{R}^n$	n-dimensional Euclidean space
$\mathbb{R}^n_+$	n-dimensional positive orthant
$\overline{\mathbb{R}}^n_+$	n-dimensional nonnegative orthant
$\overline{z}$	complex number
j	complex imaginary unit, $\mathrm{j} = \sqrt{-1}$
$\angle z$	phase angle of the complex number $\overline{z}$
$\lvert z \rvert$	magnitude of the complex number $\overline{z}$
$\boldsymbol{W}$	matrix
$\boldsymbol{v}$	vector
v_j	j^{th} element of a vector $\boldsymbol{v}$
W_{ij} or $W_{i,j}$	$(i,j)^{\mathrm{th}}$ element of a matrix $\boldsymbol{W}$ (indexing order: row, column)
$\boldsymbol{W}_{i,\cdot}$	i^{th} row of a matrix $\boldsymbol{W}$
$\boldsymbol{W}_{\cdot,j}$	j^{th} column of a matrix W
$\dot{x}$ or $\frac{dx}{dt}$	time derivative of x
J	cost function of an optimization problem
θ	general notation for a parameter, or a vector of parameters
$x(t)$	value of the continuous-time quantity x at time t
$x[k]$	value of the discrete-time quantity x at the k^{th} sampling instance, i.e. $x[k] = x(k\,\tau)$ where τ is the sampling time

Notations for energy systems

v	voltage
i	current
R	resistance of a resistor
C	capacitance of a capacitor
$\angle v$	phase angle ϕ of the sinusoidal voltage $v = \hat{v}\,\sin(\omega\,t + \phi)$
$\lvert v \rvert$	magnitude $\hat{v}$ of the sinusoidal voltage $v = \hat{v}\,\sin(\omega\,t + \phi)$
$\overline{v}$	complex phase vector $\overline{v} = \lvert v \rvert\, e^{\mathrm{j}\angle v}$ representing the sinusoidal voltage $v = \lvert v \rvert\,\sin(\omega\,t + \angle v)$
$\boldsymbol{v}_{abc}$	three-phase sinusoidal voltage $\boldsymbol{v}_{abc} = [v_a, v_b, v_c]^T$
$\boldsymbol{i}_{abc}$	three-phase sinusoidal current $\boldsymbol{i}_{abc} = [i_a, i_b, i_c]^T$
v_{RMS}	RMS value of the voltage v, $v_{RMS} = \sqrt{\frac{1}{T}\int_{t=0}^{T} \lvert v(t) \rvert^2 dt}$
$v^{[k]}$	k^{th} upper harmonic component of the voltage v
P	active power
Q	reactive power
ε_u	voltage unbalance factor
T	temperature
K	heat transfer coefficient
C	heat capacity (only used in Section 3.1)
S	switch
Q	capacity of a battery (only used in Section 3.2)

Notations for quasi-polynomial and Lotka-Volterra systems

$\boldsymbol{x}$	state variable of a dynamical system
$\boldsymbol{y}$	output variable of a dynamical system
$\boldsymbol{u}$	input variable of a dynamical system
$\boldsymbol{x}^*$	equilibrium point of a dynamical system
$\boldsymbol{A}$	$n \times m$ coefficient matrix of the QP system
$\boldsymbol{B}$	$m \times n$ exponent matrix of the QP system
$\boldsymbol{M}$	$m \times m$ coefficient matrix of the LV system ($\boldsymbol{M} = \boldsymbol{B}\,\boldsymbol{A}$)
V	Lyapunov function

Chapter 1

Introduction

If you optimize everything,
you will always be unhappy.
/Donald E. Knuth/

The daily life of modern mankind is strongly influenced by technology, which has undergone strong and rapid development in the recent decades. A significant part of the consumer goods are powered by electricity, for which a proper power supply is essential, be it the battery or the mains. Nowadays, the extent of the power transmission network can affect several continents, and its operation is a complex engineering challenge.

On the other hand, due to the rapid change in technology, the technological environment become more and more complex. Without the use of models, and model based methods the development (in some cases even the operation) of our everyday devices seems to be a highly complicated task. As the model based methods are getting more and more sophisticated the models itself are getting more and more complex and nonlinear in nature.

Optimization is a very important engineering tool that has been at the service of humanity since the antiquity. Its development to its present form started in the 19$^{\text{th}}$ century and boosted in the 20$^{\text{th}}$ century. Nowadays, optimization is present in every aspects of engineering as humanity constantly tries to find a bigger, a better, a faster, a cheaper, etc. solution to the problems raised by himself.

The aim of this thesis is to present optimization-based tools for different problems arising in the field of electrical energy.

1.1 Background and motivation

Partially because of the reduction of fossil energy sources due to the unfolding climate crisis, partially because of the nuclear disaster at Fukushima, the European Union has changed its electrical energy production strategy in the recent decade. Many nuclear power plants have stopped production. These changes greatly altered the structure of energy production throughout Europe. A significant portion of this lost power production is planned to be met by cleanly produced renewable energy sources, primarily wind and solar power facilities. The rapid increase in the number of small, domestic power plants (in the range of 1 kVA-5 kVA), was apparent. However, the high fluctuation in power input from these energy sources makes this system difficult to integrate into larger and existing electrical grids [8]. Despite the many challenges, renewable energy sources are being integrated into the development of smart grids in Europe [88].

In recent decades, several countries have changed their laws regulating power supply to allow for grid-tie inverter systems to provide spare power to local low voltage electrical grids. This power is utilized locally, decreasing electrical power loss due to transmission. In addition, grid-tie inverters are suitable for conditioning power lines, correcting accurate voltage forms, and repairing reactive power in the mains. This decreases losses further, given that nonlinear distortion in the mains induces losses in both the phase and the neutral conductor. This additional functionality does not require expensive changes to existing technology. Only the control methods and regulators need to be modified in order to allow for line conditioning. The cost of changing the controlling processor and control software in this system is negligible when compared to the cost of changing equipment.

An important element of a sustainable lifestyle on Earth is the management of energy consumed and produced by the household sector. With the spread of renewable energy sources, one of the biggest technical challenges today is the efficient planning and management of energy production and usage. To meet the challenges of sustainable energy consumption, numerous developments are taking place under the banner of smart grid technologies. In contrast to the limited availability of permanent energy sources and energy production capacity, together with rapidly growing and dynamically changing energy consumption, electricity providers and electricity network operators as well as electrical appliances offer smarter and smarter solutions for various economic, technical and environmental purposes which easily facilitates the development of smart grid technologies and solutions on both of the consumer's and service provider's side. An important factor influencing this development is the electricity market, which is constantly expanding and the amount of energy sold through it is increasing.

Lithium-ion batteries are popular energy sources of the everyday life because of their high energy density, low self-discharge and light weight. Portable electronic devices (mobile phones, laptops), home electronics, electronic tools and electric vehicles (EVs) all run on some type of lithium-ion battery. In applications like electrical vehicles, batteries are connected in parallel and series in order to meet the power needs. The optimal performance and safe operation of the set of battery cells are managed by the battery management system (BMS). Another essential role of the BMS is the state of charge (SOC) and state of health (SOH) estimation. The former quantity informs the driver on the remaining charge of the battery bank (i.e. the remaining mileage that can be traveled with the electrical vehicle), while the latter shows the remaining number of charges/discharges. Just like any other battery, the performance of the lithium-ion battery is not constant but slowly degrades during the operation and strongly depends on the environmental temperature. The battery health conditions cannot be measured directly therefore it should be estimated based on measurable quantities.

Quasi-polynomial (QP) and Lotka-Volterra models have proved to be one of the candidates for generally applicable canonical forms of nonlinear system models since the majority of smooth nonlinear systems occurring in practice can be transformed into these forms.

Although Lotka-Volterra (LV) models were originally used for describing the dynamical behavior of a few species living in the same habitat [69], it is also used in several topics connected to electrical energy. The article [66] proposes a plan of a smart energy station, and uses the Lotka-Volterra model to analyze the interaction mechanism between energy business and information business. The results show that there is a mutually beneficial symbiosis relationship between them similar to that in the population ecosystem. The authors of [105] have used Lotka-Volterra model to explore the feasibility of replacing fossil fuels with nuclear energy in the United States. By applying the Lyapunov functions to conduct equilibrium analysis, they have verified that the consumption of fossil fuels will ultimately be ten-fold the consumption of nuclear energy in the long term.

1.2 Aims of the work

Based on the above short introduction and motivation, the aims of the performed work presented in this thesis can be summarized as:

1. **Model based optimization based approaches for energy systems** The aim is to develop control methods for the cost optimal operation of a class of electrical home appliances in a day-ahead market environment. The field of model predictive control theory is used to find a cost optimal operation schedule of continuously operating electrical home appliances.

   The temperature-dependent parameters of lithium-ion batteries will be estimated using a parameter estimation method based on the minimization of the prediction error, at different temperatures. The point estimates of the parameters determined at different temperatures will then be used to find a temperature characteristics fitted on the estimated parameters.

2. **Model-free optimization based methods for electrical energy systems** With the growing popularity of distributed electricity generation, injecting current (mostly from renewable sources) into the electrical grid is getting widespread. The related research aim is to find an optimal way of current injection (single phase) to the grid so that the total harmonic distortion decrease. There supposed to be no information available from the grid that is why a model-free compensation method has to be developed.

   In a three-phase network, voltage unbalance is an important indicator of power quality. The above problem of optimal current injection to the grid is formulated and solved for the three phase network case where the optimality criterion is a measure of voltage unbalance.

3. **Optimization based analysis and control of general smooth nonlinear systems based on their QP and LV representation.** The so-called quasi-polynomial system class will be used for this purpose. QP systems has a very advantageous property, namely, the structure of their Lyapunov function is known. Using this fact will facilitate the global stability analysis of general energy systems since it is only necessary to find suitable parameters of a Lyapunov function of a given form in order to prove global asymptotic stability.

   As a next step, the QP system class will be used for synthesizing controllers which ensure the global stability of the closed loop system with respect to the given Lyapunov function family. Using the fact, that with a suitable feedback the closed loop system still belongs to the class of QP systems, the same type of Lyapunov function can be used.

1.3 Structure of the thesis

The structure of the thesis is the following. The basic notions and results previously known from literature and necessary to follow the forthcoming chapters are summarized in Chapter 2. Chapters 3-6 contain the contributions of the author. Chapter 3 presents model-based scheduling and parameter estimation methods formulated as optimization problems. Chapter 4 deals with power quality improvement in electrical networks in the lack of a system model. New results in the optimization-based global stability analysis and state feedback controller design for a wide class of nonlinear systems are shown in Chapter 5. A literature review presenting the state of the art and the most important publications of the corresponding research topic can be found at the beginning of Chapters 3-5. Finally, Chapter 6 summarizes the most important new scientific contributions of the thesis. The operation of presented methods and algorithms will be illustrated by simulation experiments, some of which can be found in the Appendix.

Chapter 2

Preliminaries

2.1 Electrical energy systems

As the number of grid-tie inverter systems providing spare power to local low voltage electrical grids is constantly growing, so does their potential for conditioning power lines, correcting accurate voltage forms, and repairing reactive power in the mains. Another field undergoing a fundamental change during this process of turning residential consumers to prosumers is the electricity market, which is constantly expanding and the amount of energy sold through it is increasing.

2.1.1 Power quality of electrical networks

Power quality is described by the European standard EN-50160, which defines, and describes the main characteristics of the voltage at the network users supply terminals (or point of connection) in public networks [21]. The most important factors are frequency, supply voltage variations, rapid voltage change, flicker, unbalance and harmonics. The framework of the present thesis does not allow for a detailed discussion (see Chapter 4 for a detailed literature review), therefore only total harmonic distortion and voltage unbalance will be examined below.

In a domestic network, three-phase electric power systems have at least three conductors carrying alternating voltages that are offset in time by one-third of the period. A three-phase system may be arranged in delta or star. A star system allows the use of two different voltages from all three phases, such as a 230/400 V system which provides 230 V between the neutral (center hub) and any one of the phases, and 400 V across any two phases displayed on Figure 2.1.

The three phase voltages v_a, v_b and v_c can be expressed as sinusoidal functions of time (2.1).

$$v_i(t) = \hat{v}_i \sin(\omega t + \phi_i), \quad i \in \{a, b, c\} \tag{2.1}$$

where $\hat{v}_i = \hat{v}$ is the voltage peak ($\hat{v} = 325\,\mathrm{V}$) and $\phi_a = 0°$, $\phi_b = 240°$ and $\phi_c = 120°$, respectively.

Sinusoidal networks can be conveniently represented by phase vectors (or phasors) where the signals of (2.1) are described as complex vectors (2.2) depicted in Figure 2.2.

$$\overline{v}_i = \hat{v}_i\, e^{\mathrm{j}\,\phi_i} \tag{2.2}$$

There are an increasing number of single phase electronic devices being used today with low power consumption and simple switching power supplies (e.g., mobile phone chargers, notebooks, networking products, small variable frequency motor

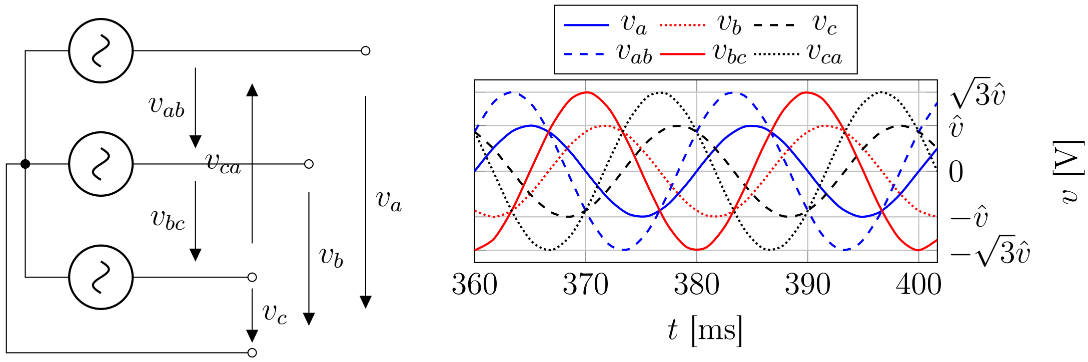

Figure 2.1: Phase voltages of a three-phase sinusoidal voltage source.

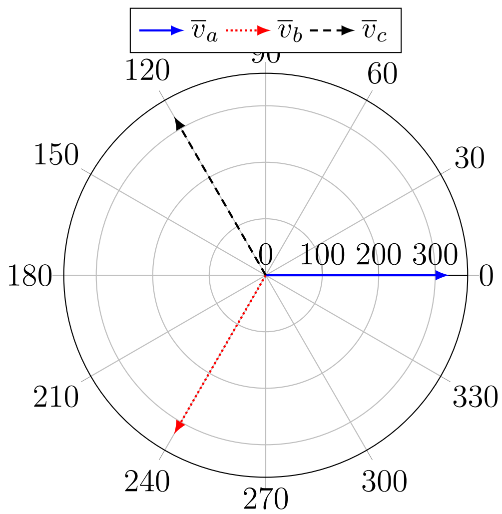

Figure 2.2: The phase vector diagram of a three-phase sinusoidal voltage. The voltage phasors $\overline{v}_a, \overline{v}_b$ and $\overline{v}_c$ form a regular triangle.

drives, consumer-grade telecommunication devices). These equipments are characterized by a performance capacitive input stage with a high nonlinear load as shown in Figure 2.3.

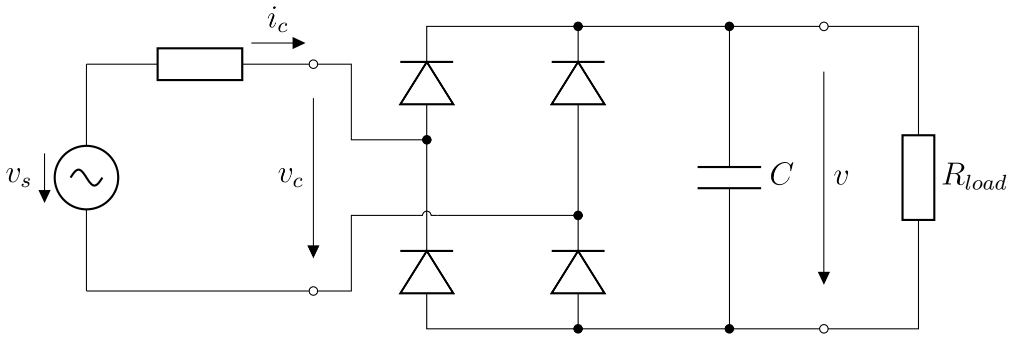

Figure 2.3: A model of a capacitive input stage causing the distortion of low consumption equipment with simple switching power supplies: a bridge rectifier with a smoothing capacitor C. A resistive load R_{load} is connected to the network.

Figure 2.4 depicts the time-domain shape of the periodic power and current signals of the capacitive input stage model (Figure 2.3), where the ideal sinusoidal voltage waveform v_s is distorted by the capacitive input stage model and results in the distorted voltage v_c. Figure 2.5 shows the frequency domain description of the above signals and indicates that there is a significant 3$^{\text{rd}}$ and 5$^{\text{th}}$ harmonic components in the current i_c. It is generally recognized that the reactive power of this nonlinear distorted voltage shape is difficult to regulate with traditional shunt capacitors (compensators). Higher-order harmonic components also have many undesirable effects on a power grid [128], causing, for example, faulty operation of the network and higher energy transportation losses and large neutral line current in three-phase networks.

Current harmonics are caused by nonlinear loads. When a nonlinear load, such as a bridge rectifier of Figure 2.3 is connected to the system, its current that is usually not sinusoidal. The Fourier series transformation allows the complex waveform to be decomposed into a series of simple sinusoids that begin at the fundamental frequency of the energy system and occur at integer multiples of the fundamental frequency.

Total harmonic distortion, or THD is a common measurement of the level of harmonic distortion present in power systems. The total harmonic distortion is defined as (2.3), [18]:

$$\mathrm{THD} = \sqrt{\frac{\sum_{k=2}^{\infty}(v_{RMS}^{[k]})^2}{(v_{RMS}^{[1]})^2}} \tag{2.3}$$

where $v_{RMS}^{[1]}$ is equal to the RMS value of the fundamental voltage and $v_{RMS}^{[k]}$ is the RMS value of the k^{th} harmonic voltage. In applications with a capacitive input stage, THD>0 holds. Note, that THD can also be defined for currents.

This type of distortion occurs in every mains plug in every home. This distortion, the nonlinear reactive power and the THD will probably increase in the near future due to the growing rate of simple switching-type power sources in household appliances as well as the rising number of CCFL bulbs and LED lamps.

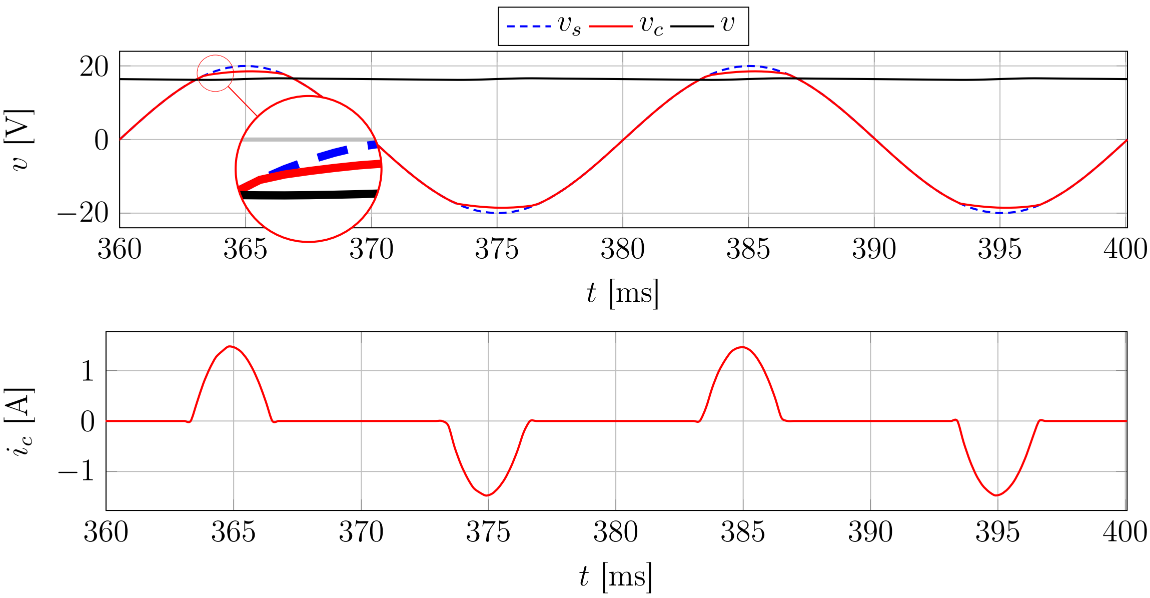

Figure 2.4: The distortion of the capacitive input stage model. The source voltage v_s is sinusoidal, while the voltage v_c measurable at the connection point is slightly distorted (top). The plot at the bottom shows the distorted current i_c flowing through the connection point.

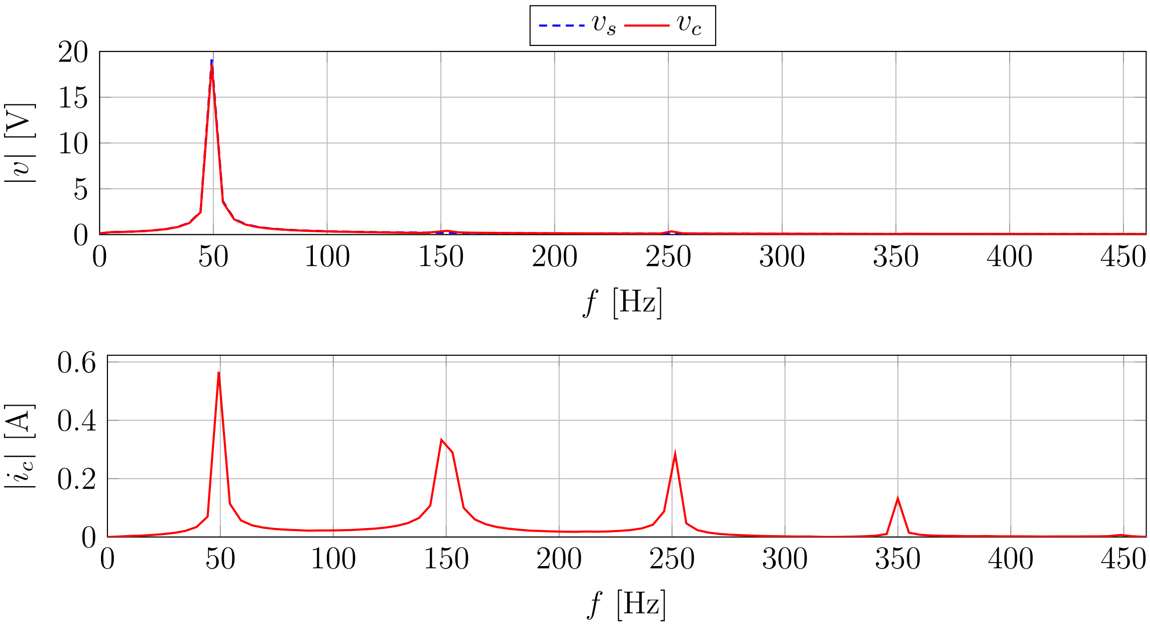

Figure 2.5: The frequency domain behavior of the bridge rectifier. The voltage v_s is purely sinusoidal, the voltage v_c has negligible upper harmonic components (top). The current i_c measurable a the connection point has significant 3rd (150 Hz) and 5th (250 Hz) upper harmonic components (bottom).

2.1.2 Voltage unbalance in three-phase networks

In a symmetric three-phase power system, three conductors each carry an alternating current of the same frequency and voltage amplitude relative to a common reference but with a phase difference of one third of a cycle between each (see Figure 2.1). The common reference is usually connected to ground and often to a current-carrying conductor called the neutral. Due to the phase difference, the voltage on any conductor reaches its peak at one third of a cycle after one of the other conductors and one third of a cycle before the remaining conductor. This phase delay gives constant power transfer to a balanced linear load.

In general symmetric three-phase systems described, are simply referred to as three-phase systems because, although it is possible to design and implement asymmetric three-phase power systems (i.e., with unequal voltages or phase shifts), they are not used in practice because they lack the most important advantages compared to the symmetric. In a three-phase system feeding a balanced and linear load, the sum of the instantaneous currents of the three conductors is zero. In other words, the current in each conductor is equal in magnitude to the sum of the currents in the other two, but with the opposite sign. The return path for the current in any phase conductor is the other two phase conductors.

Three-phase systems may also have a fourth wire, particularly in low-voltage distribution. This is the neutral wire. The neutral allows three separate single-phase supplies to be provided at a constant voltage and is commonly used for supplying groups of domestic properties which are each single-phase loads. The connections are arranged so that, as far as possible in each group, equal power is drawn from each phase. Further up the distribution system, the currents are usually well balanced. Transformers may be wired in a way that they have a four-wire secondary but a three-wire primary while allowing unbalanced loads and the associated secondary-side neutral currents [111].

This is observed as a frequently cited power quality issue in low-voltage domestic distribution networks and in systems that supply large single phase loads distributed unevenly among the phases. Effects of voltage unbalance are complex, but can be categorized as structural or functional. The former refers to the asymmetry in the three-phase impedances of transmission lines, cables, transformers, etc. It occurs because it is neither economical nor necessary to maintain distribution system with perfectly symmetrical impedances. The latter refers to uneven distribution of power consumption over the three phases. Although the term voltage unbalance is unambiguous, the root phenomenon may be various as well as the standard norms used to measure unbalance. Figure 2.6 shows voltage unbalance in the phase vector notation.

The voltage unbalance factor (VUF, ε_u) was defined by the International Electrotechnical Commission [86], [25]. From the theorem of symmetrical components [30], voltage unbalance can be considered as a phenomenon that positive sequence voltage (v_p) is disturbed by negative (v_n) and zero-sequence (v_0) voltages:

$$\begin{bmatrix} v_0 \\ v_p \\ v_n \end{bmatrix} = \tfrac{1}{3} \begin{bmatrix} 1 & 1 & 1 \\ 1 & a & a^2 \\ 1 & a^2 & a \end{bmatrix} \cdot \begin{bmatrix} v_a \\ v_b \\ v_c \end{bmatrix}, \tag{2.4}$$

Where $a = e^{j2\pi/3}$ is the Fortesque operator. Based on (2.4) the formula for voltage unbalance factor can be expressed as (2.5).

$$\varepsilon_u = \left| \frac{v_n}{v_p} \right| \times 100 \tag{2.5}$$

The three-phase voltages as well as the symmetrical components can be seen in Figure

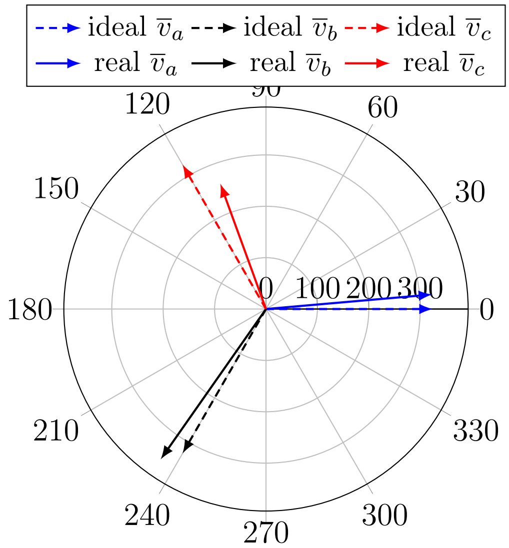

Figure 2.6: The phase vector diagram of an ideal and a real (unbalanced) three-phase voltage. The voltage phasors $\overline{v}_a, \overline{v}_b$ and $\overline{v}_c$ form a regular triangle. It can be seen that unbalance can be present due to phase difference from the one hand and from over (under) voltage on the other hand.

2.7 for two different unbalance cases.

This norm is currently in use world wide for voltage unbalance indication. The main focus in on the negative sequence component v_n, on which many studies attributes importance of the cause of negative effects the voltage unbalance causes. An extension of the VUF is the complex voltage unbalance factor (CVUF, $\overline{\varepsilon}_u$) that is defined by the ratio of the negative-sequence voltage phasor to the positive-sequence voltage phasor studied in [113], and [85]. The CVUF is a complex quantity having the magnitude and the angle. Although, CVUF has not yet been widely used by practicing engineers, it has been proposed in some studies (e.g., [114], [97], [19]) due to its richness of information on unbalance. The formula (2.6) of CVUF is similar to (2.6).

$$\overline{\varepsilon}_u = \frac{v_n}{v_p} = k_v \cdot e^{\mathrm{j}\theta_v} = k_v \angle \theta_v, \tag{2.6}$$

where k_v is the magnitude and θ_v is the angle of $\overline{\varepsilon}_u$.

The actual state of the art definition in use, VUF, is sensitive to the phase difference unbalance. Lastly CVUF considers also phase and magnitude of the voltage unbalance, but the two units (k_v, and θ_v) are hard to merge together as a singular optimization cost. To be able to employ CVUF as a successfully the weighting factor of the ratio of negative and positive symmetrical component's amplitude and phase shall be considered, which is non-trivial, and situation dependent (different network failure modes can be targeted with different weighting factors). Moreover, these definitions ignore zero sequence components and harmonic distortion that are always present in three-phase four-wire systems [9] hence, CVUF not in the scope of this thesis.

2.1.3 Electricity market

The energy needed for the operation of electrical appliances is taken from the electrical grid. The amount of energy is measured by power meters and the service provider bills the user for the price of the electrical energy consumed. If the unit price of the electrical

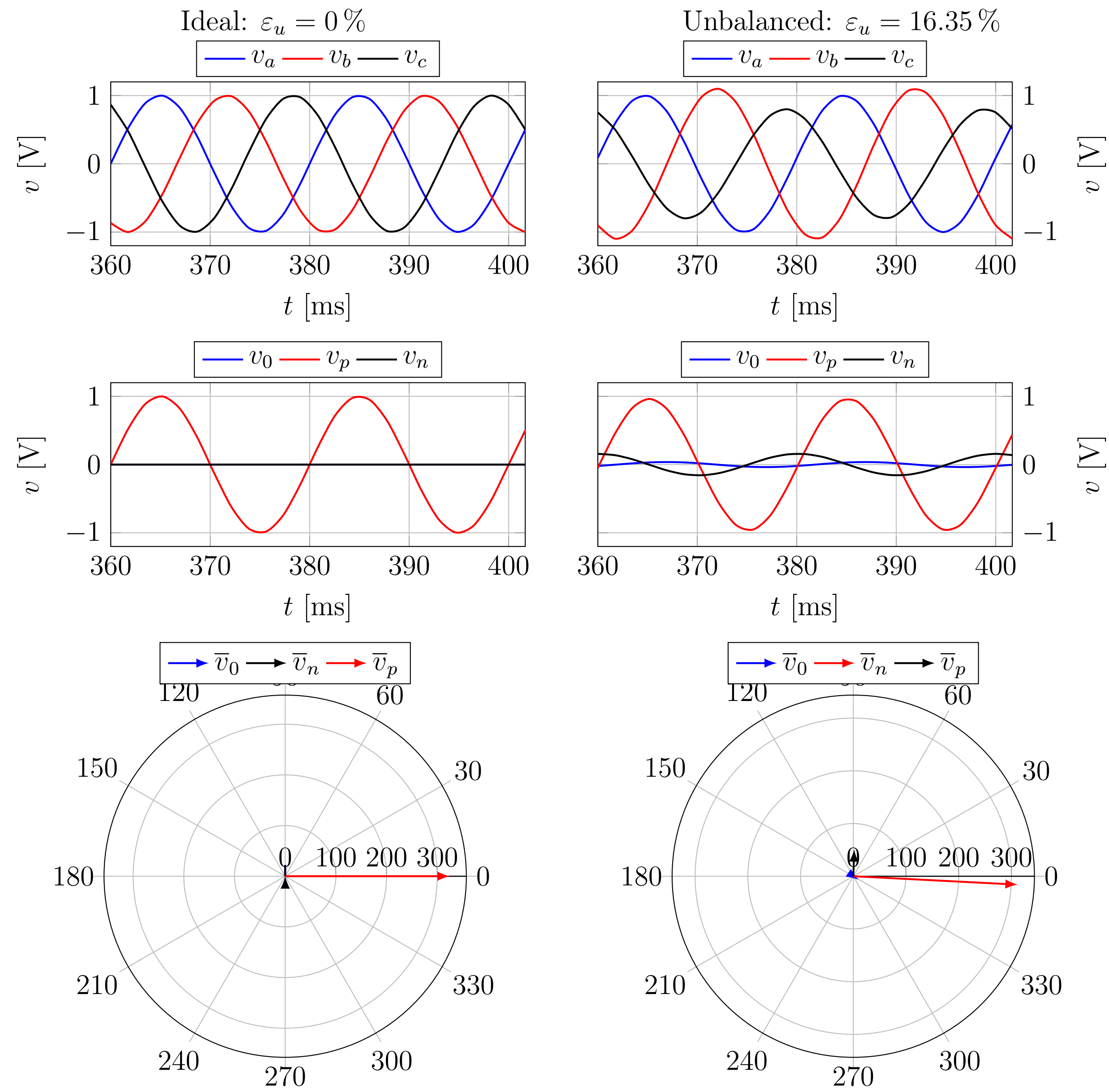

Figure 2.7: A balanced (left) and an unbalanced (right) three-phase voltage in three different views: phase voltages (top), symmetrical components as time functions (middle), and symmetrical components as phase vectors (bottom). The key role of the negative sequence voltage v_n in ε_u is apparent.

energy is the constant during the day, then the usage of the appliance for a unit of time implies the same cost. In Hungary, there are two tariffs for the purchase of electricity for residential consumers, the A1 tariff and the A2 tariff. In the case of the A1 tariff, the price of energy is the same at any time of the day, while in the case of the A2 tariff, it is slightly more expensive during peak periods (during the day) and slightly cheaper in the valley period (at night and on weekends). It is important to note that there are other tariffs as well, however, the types of equipments that can be operated from it is strictly specified by the service provider.

In northern European countries, it is possible to use a variable tariff package where the energy price is published one day in advance, taking into account the estimated production and consumption, and the unit price varies from hour to hour [48]. When the amount of energy consumed is expected to be close to the planned energy supplied to the grid, the unit price is higher, and when the consumption is lower than the planned energy fed to the grid by power plants (typically at night), this unit price is lower. The changes in such a variable energy market (or day-ahead market, DAM) are shown in Figure 2.8 using a full weekly data set [99].

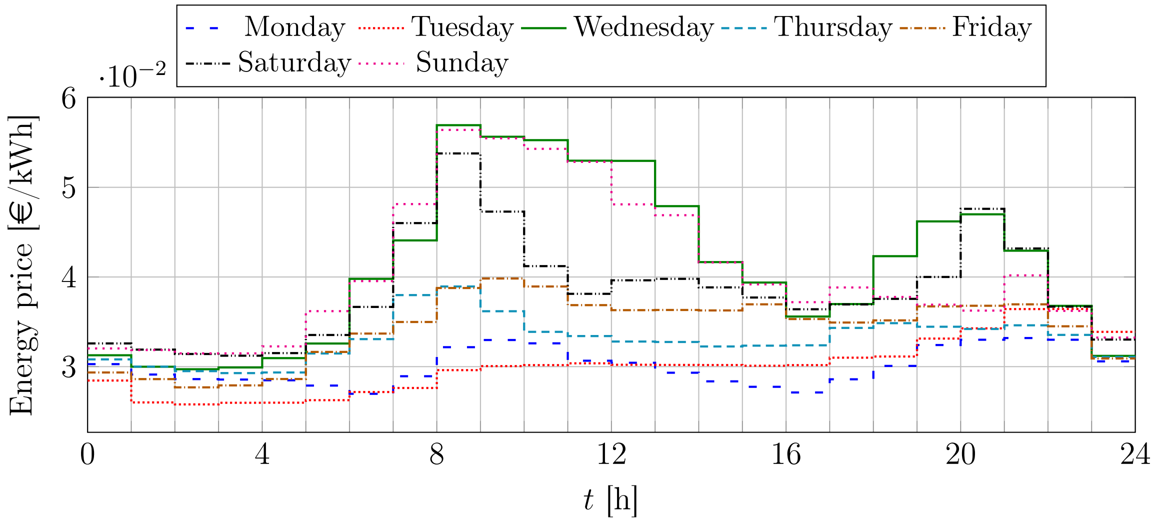

Figure 2.8: Electricity prices on a day-ahead market for a whole week. Source: [99]

It can be seen that the price of energy peaks in the morning and early evening. Two major peak periods can be observed in Figure 2.8. The first is because of the office jobs, shops, schools, which are open from morning to early afternoon. This is followed by the price of energy, as consumption is higher. The second peak period is in the early evening, when most consumers are already at home and using their electrical appliances.

2.2 Asymptotic stability of nonlinear dynamical systems

Asymptotic stability is a key property of any dynamical system and is the primary control aim of several compensation and control methods. Global stability analysis of general nonlinear systems is difficult due to the difficulties in finding a proper Lyapunov function for a general nonlinear system class.

2.2.1 Nonlinear dynamical systems

The quasi-polynomial and Lotka-Volterra system classes have a good representative potential since the majority of smooth nonlinear systems occurring in practice can be transformed into these forms, see Chapter 5 for a detailed literature review on quasi-polynomial and Lotka-Volterra systems.

The general notion of system allows us to treat physical objects originating from various fields of life: automotive systems, chemical processes, nuclear powerplants, etc. System- and control theory (see [5] for a deeper insight) allows us to examine and modify systems with mathematical tools.

General nonlinear autonomous ordinary differential equation (ODE)

$$\dot{\boldsymbol{x}}(t) = \boldsymbol{f}(\boldsymbol{x}(t)), \quad \boldsymbol{x}(t_0) = \boldsymbol{x_0} \tag{2.7}$$

in what follows, $\boldsymbol{f}$ is supposed to be a smooth, i.e. continuously differentiable nonlinear mapping.

In systems and control theory, the system is connected to its environment via its inputs and outputs, that is why the nonlinear state space model (2.8)-(2.9) has a greater practical importance.

$$\dot{\boldsymbol{x}}(t) = \boldsymbol{f}(\boldsymbol{x}(t), \boldsymbol{u}(t)), \quad \boldsymbol{x}(t_0) = \boldsymbol{x_0} \tag{2.8}$$
$$\boldsymbol{y}(t) = \boldsymbol{h}(\boldsymbol{x}(t), \boldsymbol{u}(t)) \tag{2.9}$$

where $\boldsymbol{x}(t) \in \mathbb{R}^n$, $\boldsymbol{u}(t) \in \mathbb{R}^p$ and $\boldsymbol{y}(t) \in \mathbb{R}^q$, furthermore,

$$\boldsymbol{f} : \mathbb{R}^n \times \mathbb{R}^p \to \mathbb{R}^n, \quad \boldsymbol{h} : \mathbb{R}^n \times \mathbb{R}^p \to \mathbb{R}^q$$

are smooth nonlinear mappings. A wide class of dynamical systems can be represented by the following input-affine state space model [108]:

$$\begin{aligned} \dot{\boldsymbol{x}}(t) &= \boldsymbol{f}(\boldsymbol{x}(t)) + \sum_{i=1}^{p} \boldsymbol{g_i}(\boldsymbol{x}(t)) u_i(t) \qquad \boldsymbol{x}(t_0) = \boldsymbol{x_0}, \\ \boldsymbol{y}(t) &= \boldsymbol{h}(\boldsymbol{x}(t)) \end{aligned} \tag{2.10}$$

where

$$\boldsymbol{f} : \mathbb{R}^n \to \mathbb{R}^n, \quad \boldsymbol{g_i} : \mathbb{R}^n \to \mathbb{R}^n, \ i = 1, \ldots, p, \quad \boldsymbol{h} : \mathbb{R}^n \to \mathbb{R}^q$$

are nonlinear functions. What makes (2.10) attractive is the fact that although the system is nonlinear in the states, it is linear in its inputs.

Lyapunov stability

Dynamical analysis of nonlinear systems needs advanced mathematical tools [108], [49]. Global stability analysis of nonlinear systems of the general form (2.7) calls for the searching of a suitable *Lyapunov function* V with the following properties:

- scalar valued function: $V : \mathbb{R}^n \to \mathbb{R}^+$
- positive: $V(\boldsymbol{x}(t)) > 0$
- dissipative: $\dfrac{d}{dt} V(\boldsymbol{x}(t)) = \dfrac{\partial V}{\partial \boldsymbol{x}} \dfrac{d\boldsymbol{f}(\boldsymbol{x})}{dt} < 0$

Although the form of the Lyapunov function is not known for a general nonlinear system (2.10), for some special system class it is possible to achieve results.

2.2.2 Quasi-polynomial and Lotka-Volterra systems

The elementary notions in the field of quasi-polynomial (QP) and Lotka-Volterra (LV) systems are introduced in this chapter. In order to emphasize the similarity of QP and LV systems, QP systems are also called *generalized Lotka-Volterra (GLV) systems.*

QP models Quasi-polynomial models are systems of ODEs of the following form

$$\dot{x}_i = x_i \left(\lambda_i + \sum_{j=1}^{m} A_{ij} \prod_{k=1}^{n} x_k^{B_{jk}} \right), \quad i = 1, \dots, n. \tag{2.11}$$

where $\boldsymbol{x} \in \mathrm{int}(\mathbb{R}_+^n)$, $\boldsymbol{A} \in \mathbb{R}^{n\times m}$, $\boldsymbol{B} \in \mathbb{R}^{m\times n}$, $\lambda_i \in \mathbb{R}$, $i = 1, \dots, n$. Furthermore, $\boldsymbol{\lambda} = [\lambda_1 \ \dots \ \lambda_n]^T$. The above model belongs to the class of nonlinear systems (2.7). Let us denote the equilibrium point of interest of (2.11) as $\boldsymbol{x}^* = [x_1^* \ x_2^* \ \dots \ x_n^*]^T$. It can be assumed without the loss of generality that $\mathrm{rank}(\boldsymbol{B}) = n$ and $m \geq n$ (see [44]).

Lotka-Volterra models The above family of models is split into classes of equivalence [43] according to the values of the products $\boldsymbol{M} = \boldsymbol{B}\,\boldsymbol{A}$ and $\boldsymbol{N} = \boldsymbol{B}\,\boldsymbol{\lambda}$. The *Lotka-Volterra form* known from the field of population biology [69], [109], gives the representative elements of these classes of equivalence. If $\mathrm{rank}(\boldsymbol{B}) = n$, then the set of ODEs in (2.11) can be embedded into the following m-dimensional set of equations, the so called Lotka-Volterra model:

$$\dot{z}_j = z_j \left(N_j + \sum_{i=1}^{m} M_{ji} z_i \right), \qquad j = 1, \dots, m \tag{2.12}$$

where

$$\boldsymbol{M} = \boldsymbol{B}\,\boldsymbol{A}, \quad \boldsymbol{N} = \boldsymbol{B}\,\boldsymbol{\lambda},$$

and each z_j represents a so called *quasi-monomial*:

$$z_j = \prod_{k=1}^{n} x_k^{B_{jk}}, \qquad j = 1, \dots, m. \tag{2.13}$$

Input-affine QP system models An input-affine nonlinear system model (2.10) is in QP-form if all of the functions $\boldsymbol{f}$, $\boldsymbol{g_i}$ and $\boldsymbol{h}$ are in QP-form. The general form of the state equation of an input-affine QP system model with p-inputs is:

$$\begin{aligned} \dot{x}_i \;=\; & x_i \left(\lambda_{0_i} + \sum_{j=1}^{m} A_{0_{ij}} \prod_{k=1}^{n} x_k^{B_{jk}} \right) + \\ & + \sum_{l=1}^{p} x_i \left(\lambda_{l_i} + \sum_{j=1}^{m} A_{l_{ij}} \prod_{k=1}^{n} x_k^{B_{jk}} \right) u_l \end{aligned} \tag{2.14}$$

where

$$i = 1, \dots, n, \quad \boldsymbol{A}_0, \boldsymbol{A}_l \in \mathbb{R}^{n\times m}, \quad \boldsymbol{B} \in \mathbb{R}^{m\times n},$$
$$\boldsymbol{\lambda}_0, \boldsymbol{\lambda}_l \in \mathbb{R}^n, \quad l = 1, \dots, p.$$

The corresponding input-affine Lotka-Volterra model is in the form

$$\dot{z}_j = z_j \left(N_{0_j} + \sum_{k=1}^{m} M_{0_{jk}} z_k \right) + \sum_{l=1}^{p} z_j \left(N_{l_j} + \sum_{k=1}^{m} M_{l_{jk}} z_k \right) u_l \tag{2.15}$$

where

$$j = 1, \dots, m, \quad \boldsymbol{M}_0, \boldsymbol{M}_l \in \mathbb{R}^{m\times m}, \quad \boldsymbol{N}_0, \boldsymbol{N}_l \in \mathbb{R}^m, \quad l = 1, \dots, p,$$

and the parameters can be obtained from the input-affine QP system's ones in the following way

$$\begin{array}{rcl} \boldsymbol{M}_0 & = & \boldsymbol{B}\,\boldsymbol{A}_0 \\ \boldsymbol{N}_0 & = & \boldsymbol{B}\,\boldsymbol{L}_0 \\ \boldsymbol{M}_l & = & \boldsymbol{B}\,\boldsymbol{A}_l \\ \boldsymbol{N}_l & = & \boldsymbol{B}\,\boldsymbol{\lambda}_l \end{array} \qquad l = 1, \ldots, p. \tag{2.16}$$

2.2.3 Embedding general smooth nonlinear systems into QP and LV forms

A wide class of nonlinear autonomous systems with smooth nonlinearities can be embedded into QP-form [42] if they satisfy two requirements.

1. The set of nonlinear ODEs should be in the form:

$$\dot{x}_s = \sum_{i_{s1},\ldots,i_{sn},j_s} a_{i_{s1}\ldots i_{sn}j_s} x_1^{i_{s1}} \ldots x_n^{i_{sn}} f(\boldsymbol{x})^{j_s}, \tag{2.17}$$

$$x_s(t_0) = x_s^0, \qquad s = 1, \ldots, n$$

   where $f(\boldsymbol{x})$ is some scalar valued function, which is not reducible to *quasi-monomial form* containing terms in the form of

$$\prod_{k=1}^{n} x_k^{\Gamma_{jk}}, \; j = 1, \ldots, m$$

   with $\boldsymbol{\Gamma}$ being a real matrix.

2. Furthermore, the partial derivatives of the model (2.17) have to fulfill:

$$\frac{\partial f}{\partial x_s} = \sum_{e_{s1},..,e_{sn},e_s} b_{e_{s1}..e_{sn}e_s} x_1^{e_{s1}} \ldots x_n^{e_{sn}} f(\boldsymbol{x})^{e_s}$$

The embedding is performed by introducing a *new auxiliary variable*

$$\eta = f^q \prod_{s=1}^{n} x_s^{p_s}, \qquad q \neq 0. \tag{2.18}$$

Then, instead of the non-quasi-polynomial nonlinearity f the original set of equations (2.17) can be expressed in the QP-form (2.19).

$$\dot{x}_s = \left(x_s \sum_{i_{s1},\ldots,i_{sn},j_s} \left(a_{i_{s1}\ldots i_{sn}j_s} \eta^{j_s/q} \prod_{k=1}^{n} x_k^{i_{sk}-\delta_{sk}-j_s p_k/q} \right) \right), \qquad s = 1, \ldots, n \tag{2.19}$$

where $\delta_{sk} = 1$ if $s = k$ and 0 otherwise. In addition, a new quasi-polynomial ODE appears for the new variable η:

$$\begin{aligned} \dot{\eta} \;=\; \eta \Bigg(\sum_{s=1}^{n} \Bigg(& p_s x_s^{-1} \dot{x}_s + \sum_{\substack{i_{s\alpha},j_s \\ e_{s\alpha},e_s}} a_{i_{s\alpha},j_s} b_{e_{s\alpha},e_s} q \eta^{(e_s+j_s-1)/q} \times \\ & \times \prod_{k=1}^{n} x_k^{i_{sk}+e_{sk}+(1-e_s-j_s)p_k/q} \Bigg) \Bigg), \qquad \alpha = 1, \ldots, n. \end{aligned} \tag{2.20}$$

It is important to observe that the embedding is not unique, because the parameters p_s and q in (2.18) can be chosen in many different ways: the simplest is to choose $(p_s = 0,\ s = 1, ..., n;\ q = 1)$.

If the initial values of the newly introduced variables are set according to (2.18) then the dynamics of the embedded system is equivalent to the original non-QP system described in (2.17). Since the embedded QP system includes the original differential variables x_i, $i = 1, \ldots, n$, it is clear that the stability of the embedded system (2.19)-(2.20) implies the stability of the original system (2.17).

It is important to note that QP models originate from embedding have some unusual dynamic properties because their trajectories range only a lower dimensional manifold of the QP state space. Thus they can be regarded as "hidden" differential-algebraic (DAE) system models with *rank deficient* $\boldsymbol{A}$ parameter matrices [87].

An example for embedding a smooth nonlinear dynamical system can be found in Section A.4 of the Appendix.

2.3 Applied optimization tools

In this section some of the mathematical tools applied throughout the thesis are described. The general problem statement of optimization is given in (2.21), where J denotes the cost function, or objective function to be optimized (maximized or minimized), x is the optimization variable that has to be selected such that J is optimal.

$$\min_{\boldsymbol{x}} J(\boldsymbol{x}, \theta) \tag{2.21}$$

Note, that the cost function may also depend on some parameters θ.

Problems of the form (2.21) can be solved using several different tools, depending on further assumptions on J and x. The detailed discussion of this topic is out of the scope of this thesis [45].

An extension of the optimization problem (2.21) is the so-called constrained optimization problem which can be expressed in the form (2.22) below.

$$\begin{aligned} &\min_{\boldsymbol{x}} J(\boldsymbol{x}, \theta) \\ \text{s.t.:}\quad & \begin{array}{rcl} \boldsymbol{c}(\boldsymbol{x}) & = & \boldsymbol{0} \\ \boldsymbol{d}(\boldsymbol{x}) & > & \boldsymbol{0} \end{array} \end{aligned} \tag{2.22}$$

where the problem is to be solved in the presence of constraining equations for $\boldsymbol{x}$. In the optimization problems arising in the thesis there are no equality constraints at all, while the inequality constraints are regarded to be linear or affine (i.e. $\boldsymbol{d}(\boldsymbol{x})$ is linear, or affine). The cost function J is quadratic in the simplest cases. In some other cases appearing in the thesis, the cost function cannot used in closed form, and can only be evaluated at given points $\boldsymbol{x}$ of the optimization space.

2.3.1 Model predictive control

Model predictive control (MPC) is an efficient and popular method for solving multivariate optimal control problems in energy-related control and scheduling applications ([71]). This method of management is widely recognized in both industrial and academic sectors due to its vast theoretical background and ability to simultaneously handle multivariate regulatory problems [89]. However, the model predictive approach requires a reliable dynamic model of the controlled dynamic system.

Model predictive control is a special form of control where the appropriate input is selected based on an optimization involving the model of the system and the possible future inputs [14]. It is originated from the field of process control but can be used, for example, to control speed or torque for different drives, or even in robotics. Model predictive control consists of the following main elements:

- a predictive system model,
- a cost function describing the control aim
- obtaining the control law.

Thus, in the case of model predictive control, it is important to know the system model, which defines a connection between the input and the output. Based on these, an algorithm can be used to calculate the behavior of the system and determine an input signal sequence to set the desired output. The prediction of the behavior of the system in time, the prediction of the operation is called the horizon (H). This operation is depicted in Figure 2.9.

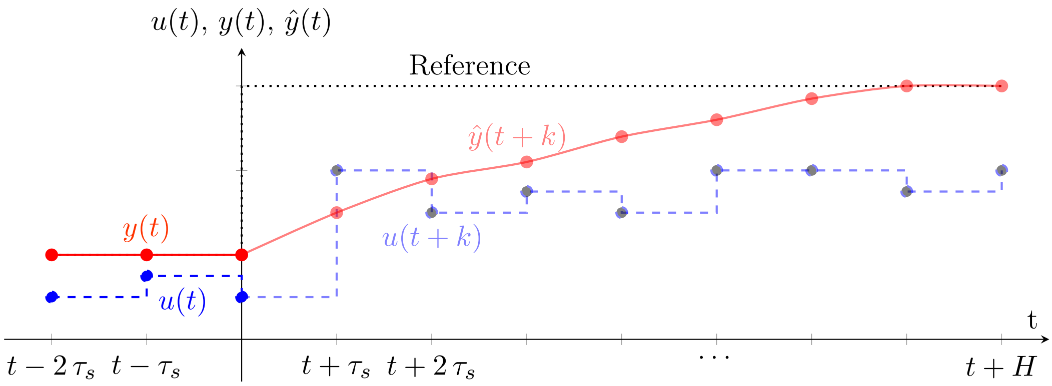

Figure 2.9: Important signals in model predictive control

Signals $u(t)$ and $y(t)$ are the inputs and the outputs applied and measured at the system in the past. Reference is the trajectory that has to be followed by the output $\hat{y}(t+k)$ in the future. This is ensured by the optimization structure of Figure 2.10 where the optimizer has to solve a constrained optimization problem between each discrete time instant in order to fint the optimal future inputs $\hat{u}(t+k)$ within a finite horizon H. At the next discrete time instant, only the first future input $\hat{u}(t+1)$ will be applied on the system and the optimization starts over.

2.3.2 Asynchronous parallel pattern search

In this section, the applied optimization structure, namely the APPS algorithm shall be discussed in detail. They commonality in this work, is that all of them are designed to search for the optimal control input for a current governing system, should it be voltage unbalance reduction with no applicable network model (due the actors unpredictability), or reaching the fastest reference value with explicit predictive control with the converter's equation's considered. The APPS can rather be described as a linear search program, distributed in a multi-dimensional plane, where there is only a black box model available [60]. These variants of pattern search can solve nonlinear unconstrained problems of the form of (2.23),

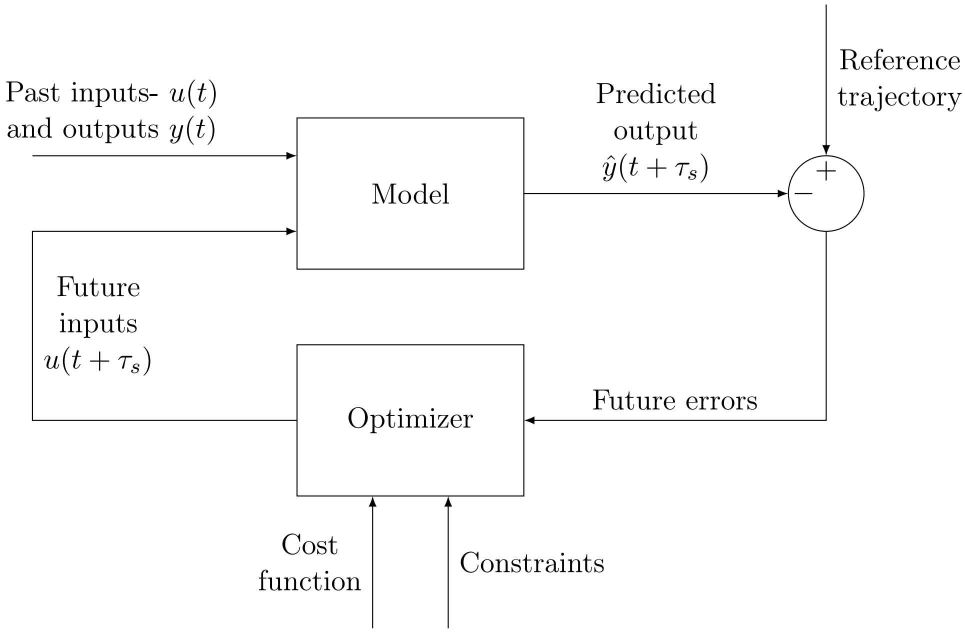

Figure 2.10: Block scheme of model predictive control

$$\min_{\boldsymbol{x}\in\mathbb{R}^n} J(\boldsymbol{x}), \tag{2.23}$$

where $J : \mathbb{R}^n \longrightarrow \mathbb{R}$. We assume that the evaluation of J is computationally expensive, hence the interest in using either distributed or parallel computing environments to solve the problem. It needs to be concentrated on the parallelization of the search strategy, rather than on the evaluation of J, though the techniques discussed here can be adapted to handle problems for which the computation of J also can be distributed. Additionally is assumed that the gradient ∇J is unavailable. For such problems, pattern search methods are one possible solution technique since they neither require nor explicitly estimate derivatives.

Note, that an extension of the APPS method [59] is also capable of solving the constrained optimization problem (2.24) which is a version of the general constrained optimization problem (2.22).

$$\begin{aligned} &\min_{\boldsymbol{x}\in\mathbb{R}^n} J(\boldsymbol{x}) \\ \text{s.t.:} \quad &\boldsymbol{x}_{LB} \;\leq\; \boldsymbol{x} \;\leq\; \boldsymbol{x}_{UB}, \end{aligned} \tag{2.24}$$

where $\boldsymbol{x}_{LB}$ and $\boldsymbol{x}_{UB}$ are the vector of lower and upper bounds on the optimization variable $\boldsymbol{x}$.

In the present thesis the optimization problems solved by APPS will be in the form (2.23), however, they can be easily be reformulated to be in the form (2.24).

Parallel pattern search Lets adopt an infinite sequence of iterations $\rho = 0, 1, 2, \dots,$ with the last iteration noted as $\rho - 1$ and initialization at 0. It is assumed that the process knows the best point so far as $\boldsymbol{x}^{\rho-1}$, where $J(\boldsymbol{x}^{\rho-1})$ is the global minima of J. Associated with $\boldsymbol{x}^{\rho-1}$ there is a step-length control parameter namely $\Delta^{\rho-1}$. Each $i \in \mathcal{P}$, where $\mathcal{P} = \{1, \dots, p\}$ process ends iteration at $\rho - 1$ by constructing it's trial point and initiating an evaluation of $J(\boldsymbol{x}_i^{\rho-1} + \Delta_i^{\rho-1}\boldsymbol{d}_i)$, where $\mathcal{D} = \{\boldsymbol{d}_1, \dots, \boldsymbol{d}_p\}$ is the finite set of directions applied by each individual process. The simultaneous start of the function evaluations at the trial points on each of the p processes signals the start of iteration ρ. When all of the participating processes are finished with their evaluation of J, they communicate these values to each other and determine the new values of $\boldsymbol{x}^\rho$, and Δ^ρ. If there exists an $i \in \mathcal{P}$, such that $J(\boldsymbol{x}_i^{\rho-1} + \Delta_i^{\rho-1}\boldsymbol{d}_i) < J(\boldsymbol{x}^{\rho-1})$, then $\rho \in \mathcal{S}$, where $\mathcal{S}$ denotes the successful iterations.

Adding asynchronicity With said above, the general strategy for asynchronous parallel pattern search, from the perspective of a single process $i \in \mathcal{P}$ is outlined in Algorithm 1

Algorithm 1 Asynchronous Parallel Pattern Search algorithm

loop
  Evaluate $J(\boldsymbol{x}_i^{best} + \Delta_i^{best}\boldsymbol{d}_i)$
  if $J(\boldsymbol{x}_i^{best} + \Delta_i^{best}\boldsymbol{d}_i) < J(\boldsymbol{x}_i^{best})$ **then**
    broadcast result to all other processes
  end if
  Update local values $\boldsymbol{x}_i^{best}$ and Δ_i^{best} based on the current local information
end loop

The price paid is that each process has its own notion of the best known point seen so far, as well as its own value for Δ^i. Any success on one process is communicated to all other processes participating in the search, but the successful process carries on from its new best point without waiting for a response from the other processes. By adding a few mild conditions, the global convergence of the search can be still ensured [60]. The indexing based on discrete time instance, where the set $\mathcal{Q} = \{1, 2, \ldots, q\}$ denote the index of steps. Thus $\boldsymbol{x}_i(q)$ s used for the best point known to process i at time step q, and similarly, $\Delta_i(q)$. So if process i starts a function evaluation at time step q, the trial point at which the function evaluation will be made at $\boldsymbol{x}_i(q)+\Delta_i(q)\,\boldsymbol{d}_i$. Further worth mention, that time steps are assumed to be of fine enough resolution so that at most one function evaluation finishes per process per time step.

Lets define two sets that satisfy $\mathcal{Q} = \mathcal{S}_i \cup \mathcal{U}_i$, , and $\mathcal{S}_i = \mathcal{I}_i \cup \mathcal{E}_i$, where $\mathcal{S}_i$ is the set of all time successful steps on process i, $\mathcal{I}_i$ is the set if internal successes, $\mathcal{E}_i$ is the set of external successes, and $\mathcal{U}_i$ consists the unsuccessful steps respectfully. An internal success, where the process finds itself the minima, the external success is where the process is updated externally by the minima. Further $\mathcal{C}_i \in \mathcal{U}_i$ is defined as the set of time steps where Δ_i^t is reduced. All the above cases $(\mathcal{U}_i \backslash \mathcal{C}_i)$ no action is performed.

The updating functions allow us to give the following general definitions for $\boldsymbol{x}_i^q$ and Δ_i^q. For every $q \in \mathcal{Q}$, $q > 0$, the best point for the i^{th} process defined to be:

$$\boldsymbol{x}_i^q = \begin{cases} \boldsymbol{x}_{\omega_i(q)}^{\tau_i(q)} + \Delta_{\omega_i(q)}^{\tau_i(q)}\boldsymbol{d}_{\omega_i(q)}, & \text{if } q \in \mathcal{S}_i \\ \boldsymbol{x}_i^{q-1}, & \text{otherwise} \end{cases} \tag{2.25}$$

with the initialisation $\boldsymbol{x}_i^0 = \boldsymbol{x}^0$, where $\omega_i(q)$ is the generating process index for the update time at step q on process i, and $\tau_i(q)$ is the time index for initialization of the function evaluation, that produced the update at time q on process i. For every q the step length control parameter Δ_i^q defined to be:

$$\Delta_i^q = \begin{cases} \lambda_{\omega_i(q)}^{\nu_i(q)} \Delta_{\omega_i(q)}^{\tau_i(q)}, & \text{if } q \in \mathcal{S}_i \\ \theta_i^q \Delta_{\omega_i(q)}^{\tau_i(q)}, & \text{if } q \in \mathcal{C}_i \\ \Delta_i^{q-1}, & \text{otherwise} \end{cases} \tag{2.26}$$

with the initialization $\Delta_i^0 = \Delta^0$, where $\nu_i(q)$ is time index for the completion of the function evaluation that produced the update at time step q on process i, and θ_i^q and λ_i^q are chosen. With the following pattern followed, the local minima of f shall eventually be reached in an undetermined number of steps.

2.3.3 Linear and bilinear matrix inequalities

In what follows, linear- and bilinear matrix inequalities are defined as special tools applied by system- and control theory [10].

Linear matrix inequality

A (non-strict) linear matrix inequality (LMI) is an inequality of the form

$$\boldsymbol{F}(\boldsymbol{x}) = \boldsymbol{F}_0 + \sum_{i=1}^{m} x_i \boldsymbol{F}_i \leq \boldsymbol{0}, \tag{2.27}$$

where $\boldsymbol{x} \in \mathbb{R}^m$ is the variable and $\boldsymbol{F}_i \in \mathbb{R}^{n\times n}$, $i = 0, \ldots, m$ are given symmetric matrices. The inequality symbol in (2.27) stands for the negative semi-definiteness of $\boldsymbol{F}(\boldsymbol{x})$. If the equality is not allowed, then the LMI is termed *strict*.

One of the most important properties of LMIs is the fact, that they form a convex constraint on the variables, i.e. the set $\mathcal{F} = \{\boldsymbol{x} \mid \boldsymbol{F}(\boldsymbol{x}) \leq \boldsymbol{0}\}$ is convex and thus many different kinds of convex constraints can be expressed in this way [10], [92]. It is important to note that a particular point from the convex solution set $\mathcal{F}$ can be selected using additional criteria (e.g. different kinds of objective functions) [10]. Standard LMI optimization problems are e.g. linear function minimization, generalized eigenvalue problem, etc.

Various problems in system- and control theory can be written up as a set of linear matrix inequalities. For example, the Lyapunov equation connected to the global stability of LTI systems. But they also appear in the context of *linear parameter-varying* (LPV) systems, or within μ-analysis there are also LMIs solved.

There are several software tools available for solving linear matrix inequalities. The most widespread ones are in the *Matlab Robust Control Toolbox* [31]. In spite of its great popularity it has problems when a non-strict LMI is to be solved. On the other hand, *Scilab* (an open source platform for numerical computation, see http://www.scilab.org) performs far much better for the non-strict case. The algorithm of [57] is also able to handle the rank deficiency of matrices $\boldsymbol{F}_i$ in (2.27). A good survey on the available solvers can be found in [107].

Bilinear matrix inequality

A bilinear matrix inequality (BMI) is a diagonal block composed of q matrix inequalities of the following form

$$\boldsymbol{G}_0^i + \sum_{k=1}^{p} x_k \boldsymbol{G}_k^i + \sum_{k=1}^{p}\sum_{j=1}^{p} x_k x_j \boldsymbol{K}_{kj}^i \leq \boldsymbol{0}, \quad i = 1, \ldots, q \tag{2.28}$$

where $\boldsymbol{x} \in \mathbb{R}^p$ is the decision variable to be determined and $\boldsymbol{G}_k^i$, $k = 0, \ldots, p$, $i = 1, \ldots, q$ and $\boldsymbol{K}_{kj}^i$, $k, j = 1, \ldots, p$, $i = 1, \ldots, q$ are symmetric, quadratic matrices.

The main properties of BMIs are that they are non-convex in $\boldsymbol{x}$ (which makes their solution numerically much more complicated than that of linear matrix inequalities), and their solution is NP-hard [107], so the size of the tractable problems is limited. However, there exist practically applicable and effective algorithms for BMI solution [57], [106], or [16]. In Matlab environment the TomLab/PENBMI solver [58] can be used effectively to solve bilinear matrix inequalities. Similarly to the LMIs, additional criteria can be used to select a preferred solution point of a feasible BMI from its solution set.

BMIs are mostly applied in the field of robust control, many problems can be formulated in the form (2.28).

Chapter 3

Modeling, identification and optimal operation of energy systems

Model based methods enable one to introduce a priori knowledge available about the system in hand. Model based control also allows the use of optimal control methods. Model based predictive control originated from the slow chemical industrial processes is nowadays very popular for energy applications because of the advent of fast and cheap computational units. Model based methods, on the other hand need a suitable model precisely tuned to render the actual system behavior. Parameter estimation methods play an important role in the use of any model based methods. Certain energy system classes operate under different temperatures which makes its even more difficult to develop simple (i.e. computationally effective) yet precise models.

The approaches of the provider's side include optimized pricing methods [51] to balance the energy grid in response to changes in supply (eg due to the changing availability of renewable energy sources) and to meet changing energy consumption. As a result of optimized pricing in the daily electricity market [99], the electricity prices may vary hour by hour [48]. The authors of the article [101] analysed the impact of microgrids and their potential contribution to the regulation of the demand and supply of electricity in the hourly electricity market by responding to price-based demand and concluded that both network efficiency and resilience improved. The work [54] proposed a new framework for decentralized energy coordination and production that can be used to schedule energy transport and flow. These tasks can be examined from both energy consumption and energy production sides, and a suitable smart solution to the defined problem can be found, and then a complex energy management can be implemented by combining the two results. The authors of [102] propose an open electric energy network that is open to the main entities with respect to the small scale transactions and they also propose an ecological model to simulate the market power of the investor owned utilities and the independent power producers based on a Lotka-Volterra competition model.

From the consumer's perspective, most people look for the cheapest solution by using their appliance (e.g. washing machine, dishwasher) at a low energy price, however, there are simple electrical appliances (e.g. refrigerators, freezers, electric water heaters) that operate all day. With such equipment, it is typically not possible to operate only with cheap electricity, as it can take up to several hours for the optimal energy price to appear.

Therefore, the cost-optimized operation of a composite system consisting of service providers, consumers, and the electrical grid offers a wide range of operating, scheduling, and regulatory options. On the consumer's side, certain electrical appliances can be operated at a reduced operating cost by switching them on and off on a scheduled basis, taking the dynamically changing electricity prices and equipment operating limitations into account. In the simplest case, this problem results in an optimal scheduling task, which can be found in several literatures. The article [95] presents an office building with an optimal daily micro-network-based scheduling method depending on weather conditions. The [79] literature is about optimal residential building consumption control method and cost estimation. Household appliances may be subject to optimal operation or scheduling, for example, [24]. The article [7] offers a possible solution to minimize the cost of energy used in olive oil production with variable energy prices. An important element of these solutions is the already mentioned day-ahead market (DAM), where electricity prices vary up to hourly as a result of optimized pricing.

Thermal modeling and the analysis of lithium-ion batteries under different temperatures has been addressed by several authors. The thermal modeling of batteries as well as the modeling without temperature dependency can be classified based on the scientific background (e.g. equivalent circuit models, electrochemical models). The review [72] gives a thorough analysis not only to the different electrochemical models but also to the parameter identification methods.

In such applications where the computational complexity (i.e. time) is crucial e.g. in a BMS, equivalent circuit models are widely used [83]. The authors of [118] address the study of open circuit voltage-state of charge (OCV-SOC) characterization under the influence of different temperatures. The results show that the OCV-SOC characteristics curve highly depends on the temperature. An online estimation method for model parameters and SOC is proposed in [27], for applications in EVs under various temperatures. Their model is based on the RC circuit equivalent of the investigated battery. In [74], a design of experiment approach is used for the development of the electro-thermal model of electric vehicle batteries. The basis of their work is also an equivalent circuit model of the battery. The authors of [15] investigated the influence of thermal effect on the performance of their dual Kalman filter based (state- and parameter estimation) method.

Another class of battery models is the electrochemical models where the chemical reactions and mechanisms taking place in the battery serves as a basis for the modeling equations. An electro-thermal model is developed and validated experimentally in the work [116], where electronic conduction, heat transfer, energy balance and electrochemical mechanisms are included in the model. A computationally more efficient electrochemical lithium-ion battery model is proposed in [4]. The Simplified Single Particle Model is compared with more complicated electrochemical models as well as experimental data. The work [46] gives a systematic approach for the development of thermal electrochemical models of large lithium-ion batteries for EV applications. The work [2] addresses the problem of non-uniformity of heat generation and electrochemical reaction increase with the discharge rate in an electroclemical-thermal coupled lithium-ion battery model.

Pure thermal models are also present in the literature, the authors of [29] developed a lumped parameter thermal model of the widely used $LiFePO_4$ lithium-ion battery. Using thermal measurements and the model they determined the heat transfer coefficient and the heat capacity of the examined battery.

Due to the above mentioned thermal effects taking place in lithium-ion batteries, the previously mentioned roles of BMSs are usually extended with thermal management. The mosty frequently used thermal management solutions of lithium-ion batteries (used either in HEVs or in EVs) are reviewed in paper [112].

Temperature dependence of the key battery parameters and variables motivated the authors of [117] to develop a two stage battery capacity estimation method. In the first stage, battery core temperature is being estimated afterwards, SOC and capacity is being estimated by a sliding mode observer.

3.1 Energy-efficient scheduling of household refrigerators

In the modern power grid the day-ahead market serves as the marketplace for trading power. The service provider gives the electricity price, i.e. the price for electrical energy, for the next 24 hours (see Section 2.1.3). In the case of this type of market, it is worth considering when some equipment will operate, as, there can be large differences (almost double) in the price of energy within a day. This is true not only for intermittently operated appliances (washing machine, electric stove, dishwasher) but also for continuously operating appliances such as electric boilers or refrigerators and freezers. With the right schedule, one can save money by continuing to operate the equipment at a cheaper energy price. This means that it produces warmer-than-usual water in the case of a water heater and cools the food better in the case of a refrigerator, so that the appliance only has to be switched on again later at a higher energy price. With such a schedule, the equipment typically consumes more energy, but from a consumer perspective, the cost is not determined by the moment of consumption and the current energy price. On the other hand, if the price of energy is mainly determined by the production and availability of renewable energy sources, then higher consumption also means greener energy consumption. The problem at hand, i.e. to minimize the operating cost suggests the use of model predictive control theory. Moreover, since the control law is the switching sequence of the freezers binary input, the problem to be solved is a constrained optimal scheduling problem [51].

3.1.1 Modeling

In the simplest case, a refrigerator can be regarded as a container that is cooled by a cooling liquid circuit driven by an electrical motor. The schematic structure of the main elements of this simple refrigerator is shown in Figure 3.1.

The containment is characterized by its air temperature T_a. It is heated by the outer environment through the door of the refrigerator, and cooled by the wall with temperature T_w . A liquid cooling system with liquid temperature T_c provides cooling when the cooling binary switch S is on ($S = 1$), while there is no cooling of the wall when it is switched off ($S = 0$). The side wall is also heated by the outer environment.

The variables and parameters[1] of the refrigerator model are collected in Table 3.1.

The engineering model The simplest possible dynamical model that describes the dynamics of the above described refrigerator can be constructed from the energy

[1] The notation for heat capacity and electrical capacitance is the same in the thesis (C), however, their use is unambiguous, heat capacity is only appearing in Section 3.1 moreover, electrical capacitance is not appearing in this section.

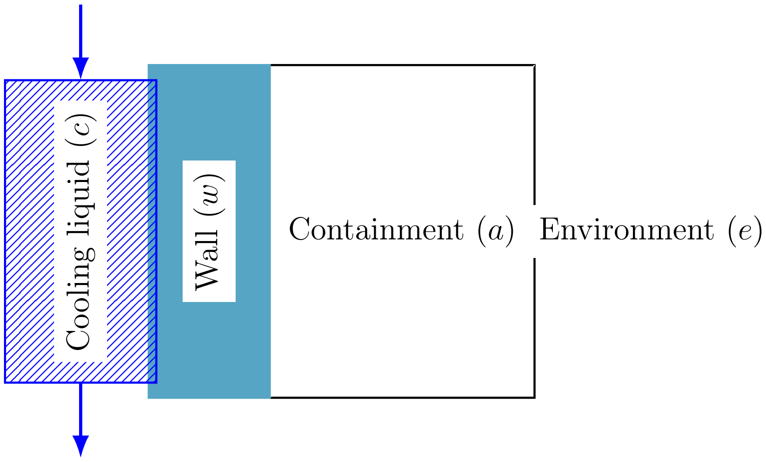

Figure 3.1: The schematic structure of the refrigerator.

Table 3.1: Model variables and parameters

meaning	symbol	classification	unit
containment air temperature	T_a	state variable	°C
wall temperature	T_w	state variable	°C
binary switch status	S	scheduling variable	–
environment temperature	T_e	parameter	°C
cooling liquid temperature	T_c	parameter	°C
minimal inner air temperature	$T_{a,min}$	parameter	°C
maximal inner air temperature	$T_{a,max}$	parameter	°C
minimal wall temperature	$T_{w,min}$	parameter	°C
maximal wall temperature	$T_{w,max}$	parameter	°C
air-wall heat transfer coeff.	K_w	parameter	$\frac{\text{kW}}{\text{°C}}$
air-env. heat transfer coeff.	K_o	parameter	$\frac{\text{kW}}{\text{°C}}$
wall-env. heat transfer coeff.	K_x	parameter	$\frac{\text{kW}}{\text{°C}}$
wall-cool. liq. heat transfer coeff.	K_c	parameter	$\frac{\text{kW}}{\text{°C}}$
heat capacity of the containment	C_a	parameter	$\frac{\text{kJ}}{\text{°C}}$
heat capacity of wall	C_w	parameter	$\frac{\text{kJ}}{\text{°C}}$

balances for the containment air and that of the wall in the following form (see [38])

$$C_a \frac{dT_a(t)}{dt} = K_w(T_w(t) - T_a(t)) + K_o(T_e - T_a(t)) \tag{3.1}$$

$$C_w \frac{dT_w(t)}{dt} = K_w(T_a(t) - T_w(t)) + K_x(T_e - T_w(t)) + S(t) \cdot K_c(T_c - T_w(t)) \tag{3.2}$$

with the variables and parameters collected in Table 3.1.

The first terms in the right-hand sides of the equations correspond to the heat transfer between the containment air and the wall, the second transfer terms correspond to the transfer between the outer environment and the containment air or the wall, respectively, and the last term in the second equation describes the effect of the cooling liquid. The parameters of the model are assumed to be constant.

Piecewise affine model Let us define two operating modes of the freezer: the cooling and the reheating modes. In both cases the state space model is in the following piecewise affine time-invariant model form [20]:

$$\dot{\boldsymbol{x}}(t) = \boldsymbol{A}_S\,\boldsymbol{x}(t) + \boldsymbol{B}_S \tag{3.3}$$

$$\boldsymbol{y}(t) = \boldsymbol{x}(t) \tag{3.4}$$

where the state variables of the dynamic model are

$$\boldsymbol{x}(t) = \begin{bmatrix} T_a(t) \\ T_w(t) \end{bmatrix} \tag{3.5}$$

where the scheduling variable $S(t)$ is the position of the switch at time t, which determines the actual operating mode of the system. The system output $\boldsymbol{y}$ is supposed to be the state vector, i.e. all states are measured. The value of the coefficient matrices $\boldsymbol{A}_S$ and $\boldsymbol{B}_S$ differ according to the to operation modes of the refrigerator, i.e. the On mode (when the cooling is taking place) and the Off mode (when the cooling is off).

On mode The first operating mode is when the switch is closed ($S = 1$), i.e. *the refrigerator is cooling.* Then the parameter matrices and vectors are

$$\boldsymbol{A_1} = \begin{bmatrix} -\frac{K_w+K_o}{C_a} & \frac{K_w}{C_a} \\ \frac{K_w}{C_w} & -(\frac{K_w}{C_w} + \frac{K_c}{C_w} + \frac{K_x}{C_w}) \end{bmatrix}, \quad \boldsymbol{B_1} = \begin{bmatrix} \frac{K_o T_e}{C_a} \\ \frac{K_x T_e + T_c\, K_c}{C_w} \end{bmatrix}. \tag{3.6}$$

Off mode The second operating mode is when the switch is open ($S = 0$), i.e. *the refrigerator is reheated to the environmental temperature.* Then the parameter matrices and vectors are as follows:

$$\boldsymbol{A_0} = \begin{bmatrix} -\frac{K_w+K_o}{C_a} & \frac{K_w}{C_a} \\ \frac{K_w}{C_w} & -(\frac{K_w}{C_w} + \frac{K_x}{C_w}) \end{bmatrix}, \quad \boldsymbol{B_0} = \begin{bmatrix} \frac{K_o T_e}{C_a} \\ \frac{K_x T_e}{C_w} \end{bmatrix} \tag{3.7}$$

The applied dynamical model (3.3) seems to omit the input signal at first sight. Note, that the binary input S appearing in the engineering model (3.1)-(3.2) plays the role of the operation mode switch in the applied model (3.3). More details on the engineering model together with a parameter set relevant to a household refrigerator can be found in [123].

3.1.2 Problem statement

Control aim

In order to be able to select the correct solution method for the problem, it is important to specify the control aims. From the consumer point of view, the most obvious aim of controlling an electrical equipment may be to minimize the already mentioned operating cost, i.e. the electricity bill. Thus, the primary goal is to minimize operating costs by scheduling the operation of the equipment, taking into account the following:

- The operating cost is the price of electricity consumed during the day.
- The price of energy varies from hour to hour, constant between two changes.
- The price of energy is known 24 hours in advance.

- The equipment must operate within the operating limits.
- The thermal impact of the equipment on the environment is negligible.
- The control input S is a binary signal, i.e. $S \in \{0; 1\}$.

Model predictive scheduling of freezers

The control aim, i.e. to minimize the operating cost suggests the use of model predictive control theory for this problem. Moreover, since the control law is the switching sequence of the refrigerators binary input, the problem to be solved is a constrained optimal scheduling problem.

In order to be able to apply the tools of model predictive control theory, one needs a suitable predictive model that describes the behavior of the controlled plant (refrigerator). The cost function usually formed as a combination of quality and/or economic expectations against the system, moreover, constraints are also introduced to the system's (state) variables which usually define some region of safety operation for the system.

Predictive system model As a first step the continuous-time model (3.6-3.7) is discretized with sampling time τ in order to get the discrete-time piecewise affine (PWA) system model used in the sequel.

$$\Sigma_S : \left\{ \begin{array}{rcl} \boldsymbol{x}[k+1] & = & \boldsymbol{\Phi}_S\, \boldsymbol{x}[k] + \boldsymbol{\Gamma}_S \\ \boldsymbol{y}[k] & = & \boldsymbol{x}[k] \end{array} \right. , \; S \in \{0; 1\} \tag{3.8}$$

where $\boldsymbol{x}[k]$ stands for the value of the vector valued signal $\boldsymbol{x}$ at the time instant $k\,\tau$, matrices $\boldsymbol{\Phi}_S = e^{\boldsymbol{A}_S\,\tau}$ and $\boldsymbol{\Gamma} = \boldsymbol{A}_S^{-1}(e^{\boldsymbol{A}_S\,\tau} - \boldsymbol{I})\boldsymbol{B}_S$ are the matrices of the state equation discretized by sampling time τ.

Cost function The operating cost to be minimized (i.e. the price of the consumed electrical energy) is the discrete sum (3.9).

$$J(p, S) = \sum_{k=1}^{N} p[k]\, S[k]\, h \quad , \tag{3.9}$$

where N is supposed to be the prediction horizon size. It is also supposed that the price schedule of the next day are known at least $H = N\,\tau$ time (prediction time) before midnight. It is important to note, that the price signal p has a sampling time of one hour between its values, but this is not equal to the sampling time τ of the dynamics (3.8), $\tau < 1\,\mathrm{h}$ in practice. In the cost function (3.9) above, $p[k]$ denotes the price signal resampled with τ.

Constraints The constraints (3.10) on the state variables describing the operating limits of the system. In the case of a refrigerator, the most important one is the limits defined for the state variable T_a as it describes the lower and upper bounds for the air temperature of the interior.

$$\boldsymbol{x}_{LB} \;\leq\; \boldsymbol{x}_k \;\leq\; \boldsymbol{x}_{UB} \;, \tag{3.10}$$

The freezer air and wall temperatures has to obey the following constraints (3.11).

$$\boldsymbol{x}_{LB} = \begin{bmatrix} T_{a,min} \\ T_{w,min} \end{bmatrix}, \quad \boldsymbol{x}_{UB} = \begin{bmatrix} T_{a,max} \\ T_{w,max}\;. \end{bmatrix} \tag{3.11}$$

Summarized, the optimal scheduling problem to be solved is to find a sequence $\{S[k]\}_{k=1}^{N}$ that minimizes the cost function (3.9) with respect to (3.8) and the constraints (3.10) defined for the states. In each iteration the optimization of the cost (3.9) is performed over the fixed size prediction horizon $H = N\,\tau$, and the first element of the optimizing input sequence is applied to the real system.

3.1.3 Heuristic optimal scheduling algorithm

The integer (binary) variables in the optimization problem to be solved during the model predictive scheduling formulated in Section 3.1.2 makes it difficult to solve the problem using off-the-shelf tools [40]. An effective heuristic scheduling algorithm is proposed in this section that can be used as the optimizer for the problem articulated in the precious section.

The proposed algorithm is a version of branch and bound type optimization [80] where the branch step introduces possible switching sequences and the bound step decreases the size of the solution space based on the following three heuristic rules [123]:

Rule 1: Any scheduling sequence that yields an $\boldsymbol{x}$ breaking the bounds (3.10) is not allowed.

Rule 2: Among any two scheduling sequences the one yields a higher $\boldsymbol{x}$ at a higher cost is not optimal.

Rule 3: Any scheduling sequence containing a cooling step that could have been performed later for a lower energy price is not optimal.

The first two rules are easy to implement. The idea to apply Rule 3 is the preliminary determination of *price-equivalent cooling time* $t^p[i]$ for all subsequent price periods of the day. For the i^{th} pricing time period (hour), it can be calculated as

$$t^p[i] = \left\lceil \frac{p[i+1]}{p[i]}\,\tau \right\rceil, \quad i = 1, \ldots, 24 \tag{3.12}$$

where $p[i]$ is the price for the i^{th} hour and $\lceil . \rceil$ represents the ceiling function.

Using the price-equivalent cooling times (3.12), it is possible to determine the reference states used in Rule 3 as follows. Off-line dynamical simulations of (3.8) are performed from the initial state $\boldsymbol{x}_{UB}$ for times $t^p[i]$, respectively. The final state of the simulations are denoted by $\boldsymbol{x}_i^r$ and can be used as the reference values of the comparison: If the actual state $\boldsymbol{x} < \boldsymbol{x}^r[i]$ during the period $t^p[i]$ then switching the cooling on yields a suboptimal sequence.

The pseudocode of the proposed optimal heuristic scheduling procedure HEURISTICSCHEDULER() is given in Algorithm 2.

It is important to note, that the calculation of $t^p[i]$ and $\boldsymbol{x}^r[i]$ can be calculated off-line, once a day, preferably when the service provider gives the prices of the next day.

Adaptive extension

An obvious step towards the improvement of the heuristic scheduler Algorithm 2 is to take into account the changes of system parameters during normal operation of the refrigerator (by putting goods in and out of the refrigerator changes the heat capacity

Algorithm 2 Heuristic scheduling algorithm

procedure HEURISTIC B&B
Input:
 $\Sigma \leftarrow \Sigma_S$
 $\boldsymbol{x}$ actual state
 $\boldsymbol{x}_{LB}, \boldsymbol{x}_{UB}$ bound
 $\boldsymbol{x}^r$ bound (Rule 3)
 p electricity prices
 $n_h \leftarrow$ horizon size $N\ \tau$
Initialization:
 J empty column vector
 $\boldsymbol{S}, \boldsymbol{X}$ empty matrices
 for $i = 0; i < n_h; i++$ **do**
branch:

$$\boldsymbol{S} = \left[\begin{array}{c|c} \boldsymbol{S} & \begin{matrix} 1 \\ \vdots \\ 1 \end{matrix} \\ \hline \boldsymbol{S} & \begin{matrix} 0 \\ \vdots \\ 0 \end{matrix} \end{array}\right], \quad \boldsymbol{X} = \left[\begin{array}{c} \boldsymbol{X} \\ \hline \boldsymbol{X} \end{array}\right], \quad J = \left[\begin{array}{c} J \\ \hline J \end{array}\right]$$

  for $k = 1 : rows(\boldsymbol{S})$ **do**
   $X_{k,i+1} = \Sigma(X_{k,i}, \boldsymbol{S}_{k,i})$
   update J_k
bound (Rule 1):
   if $X_{k,i+1} \notin [\boldsymbol{x}_{LB}, \boldsymbol{x}_{UB}]$ **then**
    delete row $\boldsymbol{X}_{k,.}$, $S_{k,.}$ and J_k
   end if
bound (Rule 3):
   if $X_{k,i+1} < \boldsymbol{x}_k^r$ and $S_{k,i+1} = 1$ **then**
    delete row $\boldsymbol{X}_{k,.}$, $\boldsymbol{S}_{k,.}$ and J_k
   end if
  end for
bound (Rule 2):
  for $k, l = 1 :$ **rows**$(\boldsymbol{S})$, $k \neq l$ **do**
   if $X_{k,i+1} > X_{l,i+1}$ **and** $J_k > J_l$ **then**
    delete row $\boldsymbol{X}_{k,.}$, $\boldsymbol{S}_{k,.}$, J_k
   else
    if $X_{l,i+1} > X_{k,i+1}$ **and** $J_l > J_k$ **then**
     delete row $\boldsymbol{X}_{l,.}$, $\boldsymbol{S}_{l,.}$, J_l
    end if
   end if
  end for
 end for
optimal solution:
 $minimal value of J = J_{k_{opt}}$
 Minimizing sequence $\boldsymbol{S}_{k_{opt},.}$
end procedure

C_a of the containment). It is easy to see based on the results of this section that having a model different from the reality would result in a suboptimal scheduling sequence.

The key parameter behind the adaptivity is the heat capacity C_a of the interior air since this compartment contains the goods. The actual heat capacity $\tilde{C}_a$ is supposed to vary between a minimal value $C_{a_{min}}$ that corresponds to the empty freezer and a maximal value ($C_{a_{max}}$). The change in the heat capacity can only be detected from the available temperature measurements (T_a) taking place in the refrigerator. The adaptivity of the model predictive scheduler is implemented as a parameter estimation step in which an estimate C_a^{est} the actual value of the refrigerator interior heat capacity is being determined based on the available temperature measurements. The sensitivity of the proposed adaptive method depends on a predefined temperature difference limit (ΔT). The heat capacity is re-estimated during an iteration when condition (3.13) is true.

$$|T_a[k] - T_a^m[k]| > \Delta T \ , \tag{3.13}$$

where $T_a[k]$ is the air temperature of the model (3.8) and $T_a^m[k]$ denotes the measured value of the air temperature at the k^{th} time instant, respectively.

The pseudocode of the proposed adaptive scheduler is given in Algorithm 3, where input parameter Σ denotes the PWA dynamics (3.8). The novel element is the online parameter estimation performed in the beginning of the control loop. The online estimation of the interior heat capacity is based on the previous temperature measurements.

Algorithm 3 Adaptive heuristic scheduling algorithm

procedure AdaptiveScheduler(Σ, $\boldsymbol{x}$, $\boldsymbol{x}_{LB}$, $\boldsymbol{x}_{UB}$, $\boldsymbol{x}^r$,$\boldsymbol{x}^m$, ΔT, $\boldsymbol{p}$, N)
    if $|X_{k,i+1} - \boldsymbol{x}^m| > \Delta T$ **then**
        $\Sigma' \leftarrow$ParameterEstimation(Σ,$\boldsymbol{x}^m$) ▷ Calculating of C_a^{est}
    end if
    $S_{k_{opt},\cdot} \leftarrow$HeuristicScheduler($\Sigma'$, $\boldsymbol{x}$, $\boldsymbol{x}_{LB}$, $\boldsymbol{x}_{UB}$, $\boldsymbol{x}^r$, $\boldsymbol{p}$, N) ▷ Algorithm 2
    return $S_{k_{opt},\cdot}$
end procedure

Figure 3.2 illustrates the difference in schedule when the internal heat capacity is twice that of an empty refrigerator. The actual heat capacity is denoted by $\tilde{C}_a$. Blue solid line denotes the case when the scheduler knows the actual heat capacity $\tilde{C}_a$, red dashed line denotes the case when the scheduler calculates with the nominal heat capacity C_a.

Figure 3.2 illustrates that in the case when the heat capacity of the system is not known by the scheduler, the algorithm will still control the refrigerator sstisfactorily. This is because the dynamics of the system will be slower as the heat capacity increases, i.e. temperatures will change more slowly. The resulting control will not be cost-optimal, but the system will not exceed the defined temperature limits. The minimal heat capacity $C_{a_{min}}$ is for an empty refrigerator, so the heuristic algorithm can be used using the empty equipment system parameters.

Online estimation of C_a The online estimation of C_a (denoted by ParameterEstimation() in Algorithm 3) is performed at the beginning of a control cycle if the difference between the model output temperature and the measured temperatures $\boldsymbol{x}^m$ is greater than the predefined ΔT value (see condition (3.13)). The estimation is basically a bisection method used for finding the root of the difference $\Delta T_a(C_a)$ (3.14)

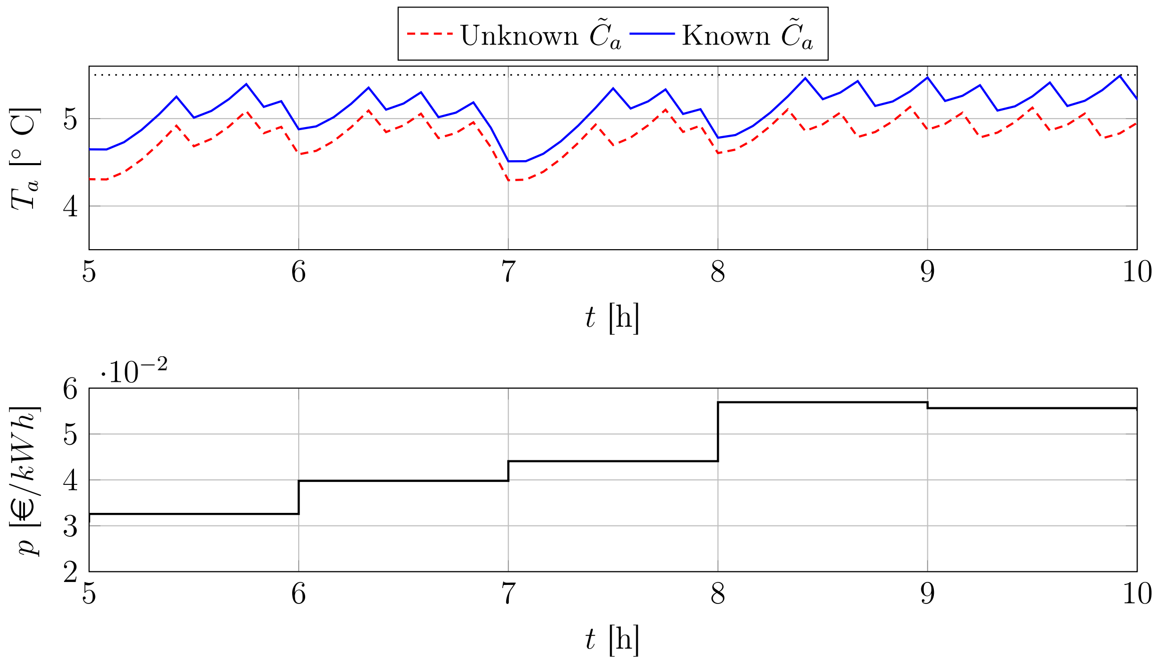

Figure 3.2: The effect of the information about actual heat capacity $\tilde{C}_a = 2\,C_a$ for the heuristic scheduling for $H = 2$ hours.

with respect to the heat capacity parameter C_a (see [121] for details).

$$\Delta T_a(C_a) = T_a^m[k] - T_a[k; C_a] \ , \tag{3.14}$$

where $T_a[k; C_a]$ is the containment air temperature computed from the discretized version of model (3.8). The root of (3.14) is denoted by $C_a^{est}[k]$.

The search interval for the value of $C_a^{est}[k]$ is an interval of length $10\,C_{a_{min}}$ with one of the end points being the previous guess for the interior heat capacity, i.e. $C_a^{est}[k-1]$. The other end point of the search interval is $C_a^{est}[n-1] \pm 10\,C_{a_{min}}$ depending on the sign of the difference $T_a[k] - T_a^m[k]$. The number of necessary iterations of the above bisection algorithm depends on the desired tolerance ε in the following form

$$N_{C_a} = \log_2\left(\frac{10\,C_{a_{min}}}{\varepsilon\,C_{a_{min}}}\right) = \log_2\left(\frac{10}{\varepsilon}\right). \tag{3.15}$$

3.1.4 Simulation case study

The proposed optimal scheduling algorithm together with its adaptive extension has been investigated using a dynamical simulation model built in Matlab Simulink environment. The details of the refrigerator, its modeling and parameter sensitivity analysis and identification is presented in Appendix A.1. The sampling time for the discrete time dynamics was $\tau = 300\,$s.

Model

The dynamical model was identified and the system matrices were determined from the measured data of the temperatures, consumption and ambient temperature of a refrigerator presented in [50]. Using these data sets, the system matrices were determined using a parameter estimation procedure based on the minimization of the prediction error (3.16). The constrained minimization of the prediction error function was performed using the Nelder-Mead simplex algorithm [62].

$$J(\theta) = \int_{t_0}^{t_f} w_a \Big(T_a(t) - \hat{T}_a(t;\theta)\Big)^2 + w_w \Big(T_w(t) - \hat{T}_w(t;\theta)\Big)^2 \, dt, \tag{3.16}$$

where w_a and w_w are weighting factors The numerical values of the discrete-time piecewise affine state space model (3.8) for the two operating modes are listed in (A.1)-(A.3) of Section A.1.

Heuristic model predictive scheduling

In the first simulation experiment, the operation of the basic version of the method was investigated. The results areS illustrated in Figure 3.3, where it is apparent, that the schedule calculated by the algorithm takes into account the operating constraints (denoted by red dotted line). Moreover, it can be seen that before a price increase the scheduler cools down the refrigerator in order to use the actual cheaper energy instead of the more expensive electricity of the next pricing interval.

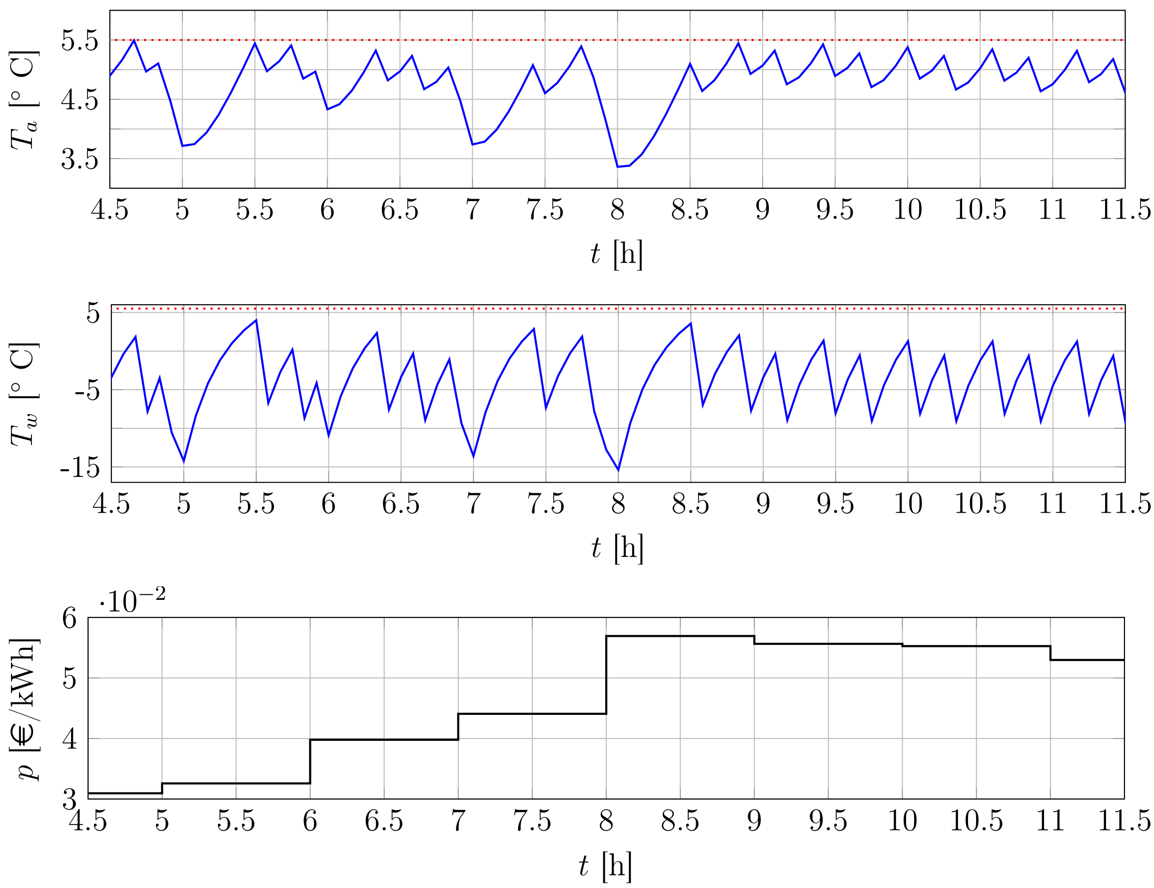

Figure 3.3: Operation of the cost optimal model predictive scheduling algorithm during the simulation experiment. The temperatures T_a and T_w and the hourly energy price can be seen (top, middle, bottom).

The aim of the second set of simulation experiments were to investigate the effect of prediction horizon size (H) on the performance of Algorithm 2. In order to make it difficult for the model predictive scheduler to find the optimal solution, Wednesday, i.e. the day with the highest price variability (see Figure 2.8) has been chosen for the experiments. The comparative simulation results are given in Figure 3.4, where the times $t_{opt}[k]$ spent with the solution of the optimization problem at the k^{th} iteration are depicted for the whole day. The results are in line with the engineering expectations i.e. a larger prediction horizon tends to be computationally more demanding. It can easily be seen in Figure 3.4 that H amount of time before the energy price is increasing the optimization problem to be solved gets computationally more demanding. Of course, the value of t_{opt} depend on the computational power of the applied computer or micro controller unit. The implementation of the algorithm on an embedded unit is out of the scope of this thesis.

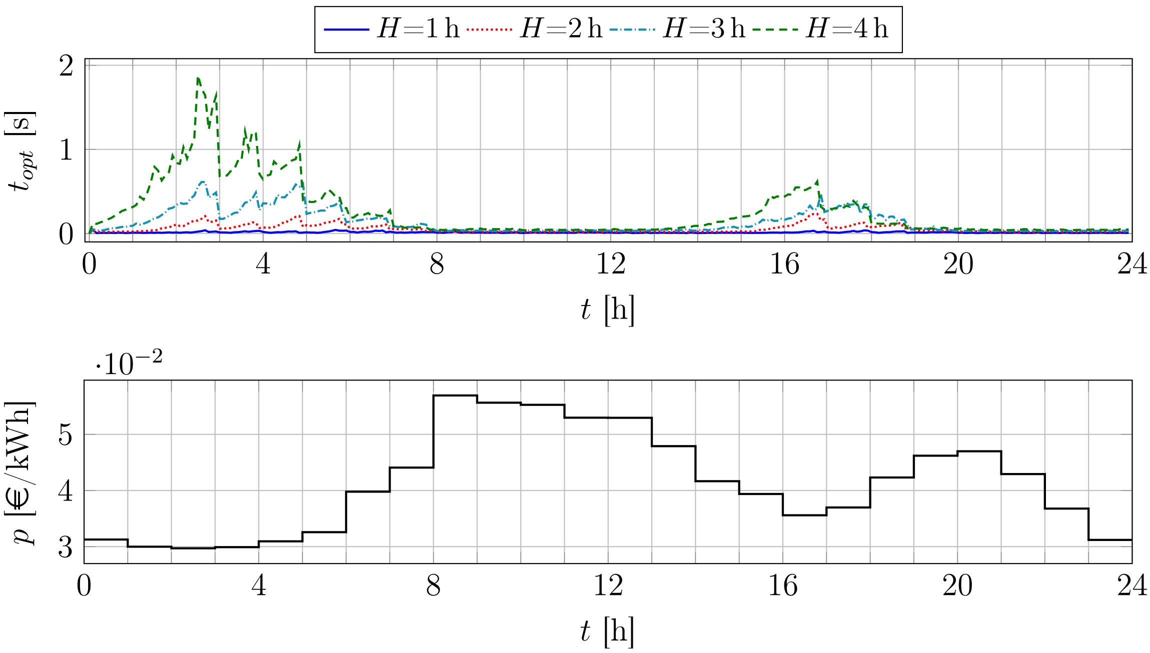

Figure 3.4: Top: The effect of prediction horizon H on the optimization time t_{opt}. Bottom: Hourly changing energy price for the examined day (Wednesday). It is apparent that H amount of time before the energy price is increasing the optimization problem to be solved gets computationally more demanding.

Table 3.2 gives a more complete picture of the computational effect of the horizon size. It is apparent that days with smaller price variance (e.g. Monday, see Figure 2.8) have a smaller total optimization time (i.e. complexity). It is important to note that from the point of view of the complexity the number of price growth steps is much more important than the degree of price growth. It can be seen that the overall optimization time (i.e. complexity) of a day is in strong correlation with the number of price growth steps.

Another aspect of horizon size has also been investigated, namely the effect of horizon size on the daily price obtained by the model predictive scheduler. Table 3.3 shows the results of the experiment. The reference values obtained from the classical hysteresis control can be seen in the last row of the table. It is easy to see, that

(i) the size of prediction horizon *does not have a serious effect* on the daily cost obtained by the algorithm,

Table 3.2: The effect of the prediction horizon size on the cumulative optimization time (given in seconds) for a whole day of the week, i.e. $\sum_k t_{opt}[k]$. The number of electricity price growth steps are shown in the last row.

H [h]	Mon.	Tu.	Wed.	Th.	Fri.	Sat.	Sun.
1	7	10	7	7	8	8	7
2	30	47	35	32	36	36	26
4	130	327	168	153	180	187	113
8	427	2675	926	731	1051	914	642
12	1023	6900	1882	1381	1881	2377	1213
24	3507	26504	4743	4843	5099	6637	2540
Number of price increases							
	9	17	11	11	14	12	9

(ii) the proposed method outperforms the classical control method on each of the examined days.

Table 3.3: The effect of the prediction horizon size on the daily operating cost [€/kWh]. As a reference, the daily values yielded by the classical hysteresis control (τ=60 s) of the refrigerator are shown in the last row.

H [h]	Mon.	Tu.	Wed.	Th.	Fri.	Sat.	Sun.
1	0.442	0.445	0.607	0.487	0.509	0.565	0.597
2	0.440	0.442	0.604	0.484	0.503	0.563	0.595
4	0.442	0.445	0.607	0.487	0.506	0.566	0.595
8	0.438	0.437	0.602	0.482	0.501	0.561	0.593
12	0.440	0.442	0.604	0.485	0.503	0.563	0.595
24	0.440	0.445	0.604	0.485	0.503	0.563	0.595
hysteresis (classical) control							
	0.464	0.464	0.638	0.510	0.531	0.594	0.627

Adaptive scheduling

Heat capacity is a crucial parameter of thermal systems since it has a serious effect on the dynamics (e.g. time constant) of the system. It is expected that the more accurate estimate C_a^{est} of the actual heat capacity $\tilde{C}_a$ enables the adaptive heuristic scheduler to approach the optimal solution. The next set of simulation experiments were aimed to highlight the differences between the non-adaptive and the adaptive model predictive schedulers, i.e. between Algorithm 2 and Algorithm 3, respectively. Figure 3.5 gives an overview on the effect of adaptivity on the results. During the experiments, the system was exposed to the price pattern of Wednesday (Figure 2.8)

The results of the adaptive heuristic model-based scheduling algorithm described above and its comparison with the simple heuristic algorithm are illustrated in Figure 3.5. The top two diagrams show the temperatures of the refrigerator and that of the model, while the last one shows the actual and estimated heat capacities. During the simulations, the unit of heat capacity can vary between the minimum, i.e. the heat capacity of an empty refrigerator ($C_{a_{min}}$) and the maximum heat capacity ($20\,C_{a_{min}}$).

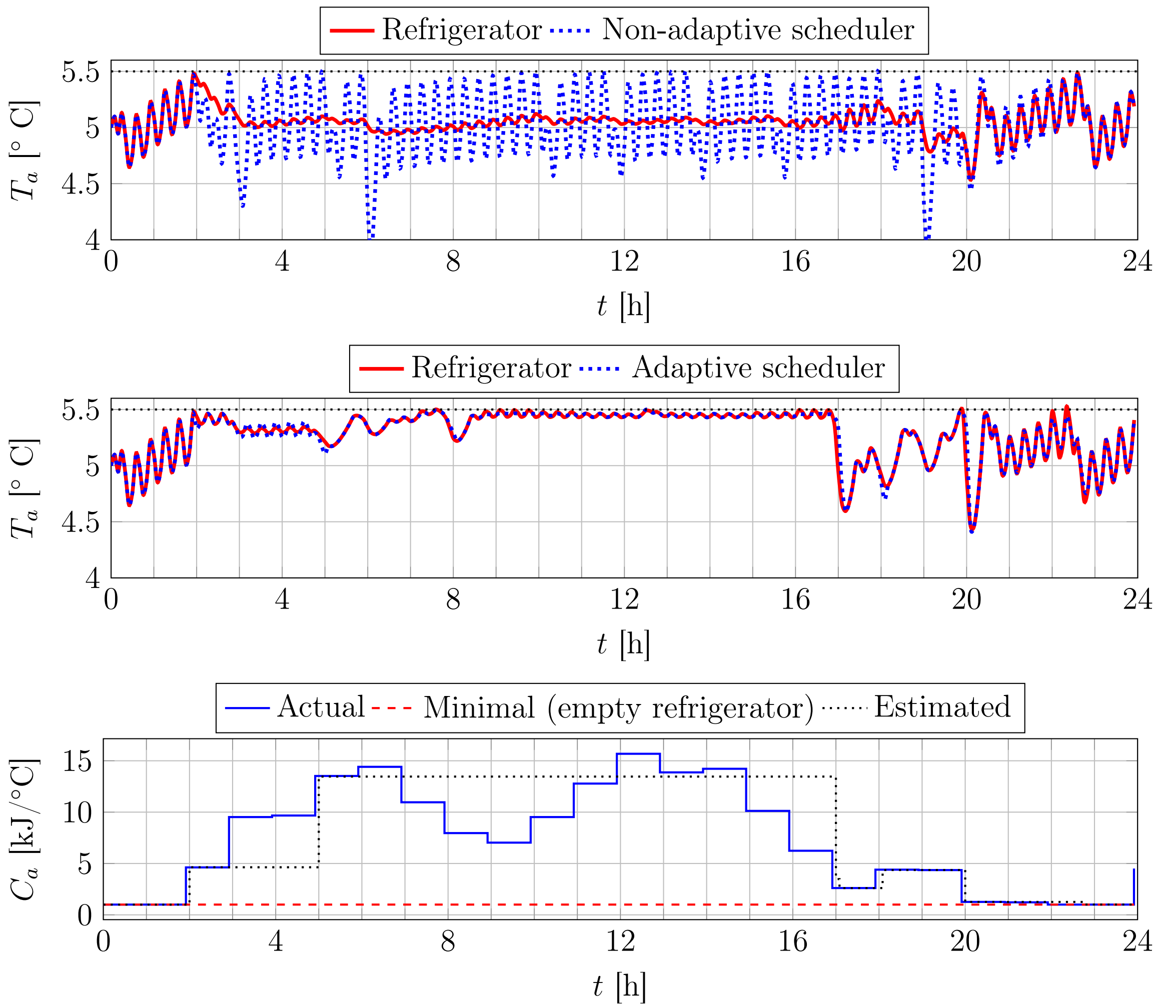

Figure 3.5: The actual and calculated temperatures T_a for different schedulet parameters. Top: non-adaptive heuristic MPC; Middle: adaptive MPC; Bottom: actual heat capacity ($\tilde{C_a}$), minimum heat capacity ($C_{a_{min}}$) and the estimated heat capacity.

The first plot illustrates the timing of non-adaptive version of the algorithm and its effect on the internal temperature of the refrigerator. In this case, the scheduler uses the minimum heat capacity $C_{a_{min}}$ in the dynamics (3.8). It can be seen that there are large changes in the calculated temperature values (dotted blue line), but the temperature does not exceed the upper temperature limit. As a result of this control, due to the varying heat capacity, the system temperature changes according to the values represented by the red solid line. It is clear that due to the increase in heat capacity, the ripple of the interior temperature decreases and its value is below the allowable upper limit. As a result, the refrigerator operates within the prescribed temperature limits, but the operating cost is higher than optimal due to the different heat capacities.

The second plot shows the operation of adaptive model predictive scheduler. A big difference from the previous one is that for a large C_a, the scheduler can keep the temperature close to the upper limit, resulting in lower operating costs. There is a minimal deviation in the schedule, but a larger deviation in the heat capacity estimate, i.e. the value of the heat capacity used in the algorithm. This is because in the case of a difference of 0.1 ° C between 3 am and 5 am, the difference in heat capacity does not cause such a difference in dynamics that it needs to be re-estimated.

3.1.5 Discussion

The results of the heuristic model-based predictive scheduling algorithm were compared with several scheduling algorithms in the article [93] where it performed well in cost optimization. Table 3.4 shows the comparative study of the operating cost savings from this article based on the results of several scheduling algorithms. The column OC (first) illustrates the performance of the proposed heuristic optimal scheduling algorithm over the other algorithms from the literature. The meanings of the abbreviations

OC Optimal Control (the method presented in this thesis)

CC-N Conventional Control

HMPC Heuristic Model Predictive Controller

HMPC-EPS HMPC with Enhanced Power Shift

HMPC-N HMPC with Narrow temperature range

HMPC-W HMPC with Wide temperature range

Table 3.4: Operating cost savings based on different control algorithms [93]

Saving [%]	OC	CC-N	HMPC	HMPC-EPS	HMPC-N	HMPC-W
Monday	9.6	6.8	9.3	7.5	8.9	8.8
Tuesday	13.7	10.4	13.7	13.7	12.7	11.8
Wednesday	8.8	7.3	8.4	7.1	8.5	7.2
Thursday	7.9	6.4	7.5	5.8	7.3	5.8
Friday	8.9	8.7	8.7	7.7	8.4	5.4
Saturday	9.0	8.9	8.6	9.0	8.7	6.7
Sunday	9.1	9.0	7.1	6.9	8.5	6.0
whole week	9.7	8.1	9.3	8.4	9.1	7.7

Specialities of the problem and their use in choosing the parameters of the algorithm There are two important special properties of the dynamic model of the refrigerator (see in (3.1)-(3.2) in the continuous time, and consequently in (3.8) in the discrete time case) that are utilized in developing the heuristic rules in the method (both in the constant and the adaptive cases)

(i) the model *input* S is *discrete valued*, $S(k) \in \{0, 1\}$,

(ii) the response of the model *output* variables T_a and T_w is *strictly monotonous* for a (step) change in input: when the switch is on, then the temperatures are decreasing, otherwise increasing.

Figure A.1 shows that it is indeed the case. Furthermore, the dominant time constant of the system can also be estimate roughly from the figure, that shows the dynamic response under normal, non-optimized operating conditions.

Besides of the use of measured data similar of Figure A.1 for parameter estimation of another freezer, the data can be used for choosing the *sampling rate and the error tolerance limits of the temperature values* in the algorithm accordingly.

The value of the prediction horizon should also be chosen considering the dynamic response of the system to a step response: it should be long enough to cover the majority of the change in this response.

Effect of energy price The simulation experiments performed in Section 3.1.4 show that both versions of the proposed model predictive schedulers are able to decrease the energy costs in a day-ahead market environment. However, they are useful only in the case of a price growth period. The proposed model predictive scheduler is sensitive to the rapid changes in the heat capacity, in such cases (primarily when C_a is falling) the air temperature may overshoot.

Generalization The specialities discussed in the previous subsection 3.1.5 can be used to find other possibilities for applying the proposed adaptive cost-optimal model predictive scheduling method. These cases include the following items.

- *Multiple independent equipments*
  When more than one freezer operate in a household, shop or plant that are independent of each other but have the same dynamically changing electricity price, then one can optimize their operation in parallel and independently of each other to get an overall optimum in cost.

- *Freezer chambers*
  Freezers in supermarkets or large industrial freezers are typically of distributed parameter nature, or consist of freezer chambers. These chambers have their individual cooling motor that cools their back wall, but they are connected to their neighboring chambers through their side walls. Therefore, these chambers are not independent of each other but can be regarded as a multiple-input multiple-output system with the cooling switches as inputs and chamber temperatures as outputs. Here the monotonicity condition (ii) should be checked that do not necessarily hold in this case. A simulation case study of an industrial freezer is presented in Appendix A.1 where the proposed model predictive scheduler is applied successfully on a different appliance.

- *Heaters*
  Simple heaters or boilers equipped with a constant power heating device controlled by a binary switch obey both conditions (i) and (ii), so the proposed heuristic method can be applied. However, the monotonicity conditions holds in another form: the response of the model *output* temperature variables is *strictly monotonous* for a (step) change in input such that *when the switch is on, then the temperatures are increasing, otherwise decreasing.*

3.2 Modeling and temperature dependent parameter estimation of batteries

The operation of real batteries depends on the temperature therefore the model has to be able to describe thermal effects too. It is also important that the obtained method should be computationally effective to simplify its implementation e.g. in a BMS.

3.2.1 Temperature dependent battery model

From the potential modeling methodologies the equivalent electrical circuit type was selected to create the basic battery model. The selected model is originally developed in [103]. The model is also presented in [141] without the thermal effect.

The following assumptions were made for the battery model of [103] with temperature dependency:

- The parameters are deduced from the discharge characteristics and assumed to be the same for charging.
- The capacity of the battery does not change with the amplitude of the current.
- The self-discharge of the battery is not represented.
- The battery has no memory effect (i.e. no aging is assumed).
- The voltage and the current can be influenced.
- The capacity depends on the ambient temperature.
- The constant potential, the polarization coefficient, the polarization resistance and the internal resistance depend on the internal (cell) temperature of the battery.

The electrical circuit equivalent to the battery can be seen in Figure 3.6, where the controlled voltage source plays the most important role since battery characteristics are implemented by it. The applied model is a simplified version of the temperature

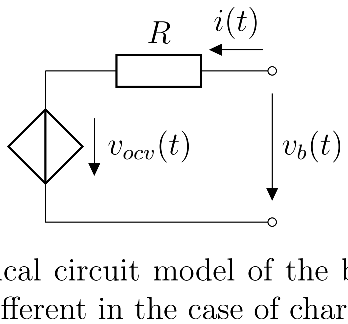

Figure 3.6: Equivalent electrical circuit model of the battery. Voltage $v_{ocv}(t)$ of the controlled voltage source is different in the case of charge and discharge.

dependent battery model presented in [104]. The input of the model is the battery current i and the output is the battery voltage v_b. The open circuit voltage v_{ocv} is represented by a controlled voltage source which operates differently during the charging and discharging operation of the battery. The model describes temperature effects as well, i.e. some of the parameters depend on the ambient or cell temperature. As a result, the temperature dependent state space model of the battery is obtained in the form of (3.17-3.19). The state equation is a simple second order linear time-invariant dynamics (3.17)-(3.18)

$$\frac{dq(t)}{dt} = \frac{1}{3600}i(t) \tag{3.17}$$

$$\frac{di_f(t)}{dt} = -\frac{1}{\tau_f}i_f(t) + \frac{1}{\tau_f}i(t) \tag{3.18}$$

$$v_b(t,T) = v_{ocv}(t,T,T_e) - R(T)i(t) \tag{3.19}$$

The state- and output variables have the following meaning:

- q is the extracted capacity of the battery, i.e. $q(t) = 0$, if the battery is fully charged and $q(t) = Q$, if the battery is fully discharged.
- i_f is a low pass filtered current value. It is used for describing the slow voltage dynamics. It is represented by a low-pass filter applied on the battery current i, where τ_f is the time constant of the filter.[103]
- the output of the model is the battery voltage v_b that is composed of the open circuit voltage (v_{ocv}) and the voltage drop across the internal resistance ($R\,i(t)$).

The open circuit voltage changes with the operation mode of the battery[2] (charge vs. discharge)

Charge mode

$$\begin{aligned} v_{ocv}(t,T,T_e) &= E_0(T) - K_1(T)\frac{Q(T_e)}{q(t)+0.1Q(T_e)}i_f(t) - \\ &\quad -K_2(T)\frac{Q(T_e)}{Q(T_e)-q(t)}q(t) + A\exp(-Bq(t)) - Cq(t) \end{aligned} \tag{3.20}$$

Discharge mode

$$\begin{aligned} v_{ocv}(t,T,T_e) &= E_0(T) - K_1(T)\frac{Q(T_e)}{Q(T_e)-q(t)}i_f(t) - \\ &\quad -K_2(T)\frac{Q(T_e)}{Q(T_e)-q(t)}q(t) + A\exp(-Bq(t)) - Cq(t) \end{aligned} \tag{3.21}$$

The state space model (3.17)-(3.19) together with the open circuit voltages for the two operation modes (3.20) and (3.21) is ambiguous. In what follows, it will always be specified which operation mode is used.

The variables as well as the parameters of the temperature dependent battery model with their meaning and nominal values can be found in Table 3.5. Our examined battery is a Samsung INR18650-20Q type battery with 2000 mAh nominal capacity and 3.6 V nominal voltage. The nominal parameters of the battery were retrieved from the battery datasheet and the Matlab Simulink model [77].

The *temperature dependency of the parameters* can be described with the following equations:

[2] The notation for battery capacity and reactive power is the same in the thesis (Q), however, their use is unambiguous, battery capacity is only appearing in Section 3.2

- The change of polarization coefficient, polarization resistance and internal resistance with the battery temperature T can be derived from the Arrhenius law:

$$K_1(T) = K_1|_{T_{ref}} \exp\left(\alpha_1\left(\frac{1}{T} - \frac{1}{T_{ref}}\right)\right) \tag{3.22}$$

$$K_2(T) = K_2|_{T_{ref}} \exp\left(\alpha_2\left(\frac{1}{T} - \frac{1}{T_{ref}}\right)\right) \tag{3.23}$$

$$R(T) = R|_{T_{ref}} \exp\left(\beta\left(\frac{1}{T} - \frac{1}{T_{ref}}\right)\right) \tag{3.24}$$

- The temperature dependency of the capacity and the constant potential can be written in the following form:

$$Q(T_e) = Q|_{T_{ref}} + \frac{\Delta Q}{\Delta T}(T_e - T_{ref}) \tag{3.25}$$

$$E_0(T) = E_0|_{T_{ref}} + \frac{\partial E}{\partial T}(T - T_{ref}) \tag{3.26}$$

Remark on the battery cell temperature
It is important to note, that the original model in [104] contains *an additional energy balance equation from which the battery cell temperature is obtained as a state variable.* In order to obtain a simple model for parameter estimation, the energy balance has been omitted and considered the battery cell temperature T as an *external variable* that does not change too much during a charge or discharge operation.

3.2.2 Parameter sensitivity analysis

As a preliminary step before parameter estimation, parameter sensitivity analysis of the dynamical model (3.17-3.19) has been performed. Note, that if the model is not, or poorly sensitive to any parameter, then estimating the corresponding parameter from input-output measurements is difficult, or even impossible. Instead of applying the classical methods of sensitivity analysis involving sensitivity equations the same empirical method described in [143] has been used i.e. perturbing the parameter values one by one with $\pm 10\%$ with respect to their nominal value and evaluated the differences of the nominal and the perturbed models outputs using the cost function

$$J(\tilde{\theta}) = \frac{1}{N}\sum_{k=1}^{N}\frac{1}{2}\left(v_b([k;\theta] - v_b[k;\tilde{\theta}]\right)^2 \tag{3.27}$$

where θ stands for the nominal parameter vector, and $\tilde{\theta}$ denotes the perturbed parameter vector.

The sensitivity analysis was repeated at 6 different temperatures: $0°C$, $10°C$, $20°C$, $30°C$, $40°C$ and $50°C$, respectively. The battery was charged/discharged between $0-100\%$ state of charge with a pseudo random binary sequence (PRBS) current input (amplitude: charge {-0.5 A, -2 A} , discharge {-5 A, -2 A}, sample time: 160 s). Both the charge and the discharge models were analysed. The nominal model was the charge/discharge model at the nominal ambient temperature $T_{ref} = 25°C$.

The dynamical models were simulated in Matlab using the model equations(3.17-3.19). At each temperatures the nominal parameters were perturbed one-by-one and

Table 3.5: Variables and parameters of the general temperature dependent battery model and the parameter values for the examined Samsung INR18650-20Q Li-ion battery.

Name	Type	Meaning	Unit	Value
i	input variable	battery current	A	-
i_f	state variable	filtered current	A	-
q	state variable	extracted capacity	Ah	-
t	independent variable	time	s	-
v_{ocv}	variable	open circuit voltage	V	-
v_b	output variable	battery voltage	V	-
T	external variable	battery cell temperature	K	-
T_e	external variable	ambient temperature	K	-
T_{ref}	parameter	nominal ambient temperature	K	298.15
τ_f	parameter	time constant of the filter	s	0.003
E_0	parameter	constant potential of the electrodes	V	-
$E_0\|_{T_{ref}}$	parameter	constant potential of the electrodes at nominal ambient temperature	V	3.9388
$\partial E/\partial T$	parameter	reversible voltage temperature coefficient	V/K	0.002
R	parameter	internal resistance	Ω	-
$R\|_{T_{ref}}$	parameter	internal resistance at nominal ambient temperature	Ω	0.005
β	parameter	Arrhenius rate constant for the internal resistance	K	3839.8
K_1	parameter	polarization constant	V/Ah	-
$K_1\|_{T_{ref}}$	parameter	polarization constant at nominal ambient temperature	V/Ah	0.0018
α_1	parameter	Arrhenius rate constant for the polarization coefficient	K	8415.3
K_2	parameter	polarisation resistance	Ω	-
$K_2\|_{T_{ref}}$	parameter	polarization resistance at nominal ambient temperature	Ω	0.0018
α_2	parameter	Arrhenius rate constant for the polarization resistance	K	8415.3
Q	parameter	battery capacity	Ah	-
$Q\|_{T_{ref}}$	parameter	battery capacity at nominal ambient temperature	Ah	2.0
$\Delta Q/\Delta T$	parameter	maximum capacity temperature coefficient	Ah/K	0.016
A	parameter	exponential voltage	V	0.1589
B	parameter	exponential capacity	$(\mathrm{Ah})^{-1}$	15.0
C	parameter	nominal discharge curve slope	V/Ah	0.2362

the value of the loss function was computed. The result of the sensitivity analysis of the charge and the discharge model can be seen in Table 3.6 and Table 3.7. The

Table 3.6: Values of the loss function in case of the parameter sensitivity analysis of the charge model.

		0°C	10°C	20°C	30°C	40°C	50°C
E_0	-10%	0.1100	0.0710	0.0728	0.0837	0.0922	0.0999
	+10%	0.1342	0.0939	0.0830	0.0721	0.0652	0.0592
K_1	-10%	0.0437	0.0047	0.0003	0.0003	0.0011	0.0020
	+10%	0.0455	0.0051	0.0004	0.0003	0.0011	0.0020
K_2	-10%	0.0365	0.0041	0.0003	0.0003	0.0011	0.0020
	+10%	0.0537	0.0059	0.0004	0.0003	0.0011	0.0020
Q	-10%	0.0376	0.0069	0.0028	0.0013	0.0005	0.0007
	+10%	0.0562	0.0054	0.0016	0.0025	0.0039	0.0055
R	-10%	0.0446	0.0049	0.0003	0.0003	0.0011	0.0020
	+10%	0.0446	0.0049	0.0004	0.0003	0.0011	0.0020

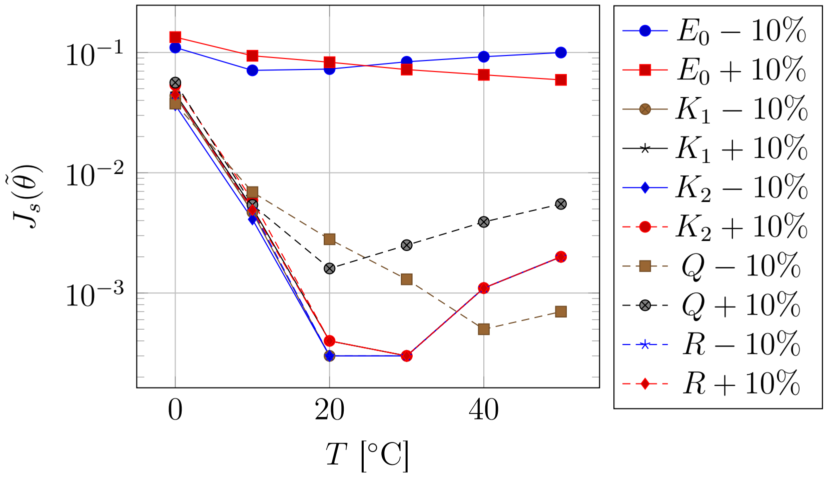

Figure 3.7: Results of the parameter sensitivity analysis of the charge model

graphical representation of the results are depicted in Figure 3.7 and Figure 3.8.

It can be seen that the discharge model is a bit more sensitive to the change of the parameters as the magnitude of the error is greater in that case. Both the charge and the discharge models have similar characteristics with respect to the parameter sensitivity:

- The models are highly sensitive to the constant potential E_0.
- The models are less sensitive to K_1, K_2 and Q.
- The rate of sensitivity is similar in case of K_1, K_2 and Q.
- The sensitivity of the models increases as the temperature decreases.
- At ambient temperatures greater than the nominal temperature, the effect of changing the parameters is really small (except for E_0), especially in case of the discharge model.

Table 3.7: Values of the loss function in case of the parameter sensitivity analysis of the discharge model.

		0°C	10°C	20°C	30°C	40°C	50°C
E_0	-10%	0.3795	0.1374	0.0912	0.0687	0.0591	0.0517
	+10%	0.1305	0.0581	0.0680	0.0886	0.1013	0.1119
K_1	-10%	0.1641	0.0184	0.0018	0.0011	0.0026	0.0042
	+10%	0.1913	0.0220	0.0022	0.0011	0.0026	0.0042
K_2	-10%	0.1578	0.0182	0.0017	0.0011	0.0026	0.0042
	+10%	0.1982	0.0223	0.0023	0.0010	0.0026	0.0042
Q	-10%	0.1362	0.0408	0.0020	0.0002	0.0023	0.0042
	+10%	0.1852	0.0346	0.0004	0.0015	0.0027	0.0042
R	-10%	0.1769	0.0200	0.0200	0.0011	0.0026	0.0042
	+10%	0.1780	0.0203	0.0020	0.0011	0.0026	0.0042

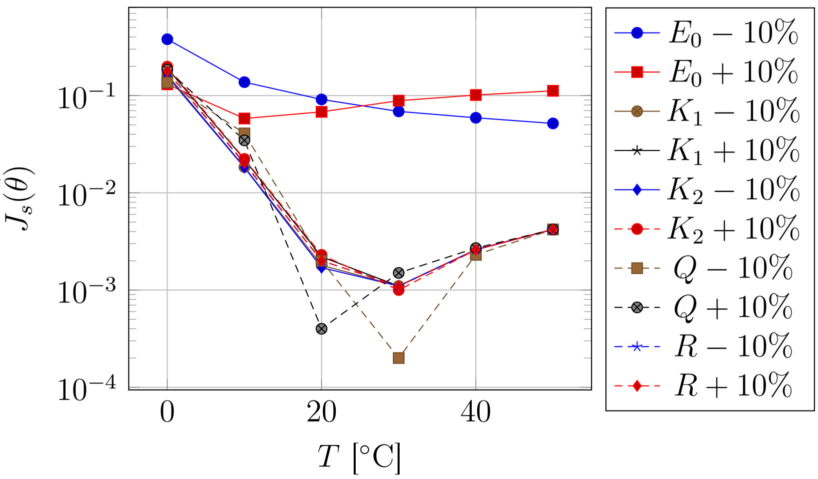

Figure 3.8: Results of the parameter sensitivity analysis of the discharge model

- The change of the internal resistance R at different temperatures has no effect on the models, as the errors related to the $\pm 10\%$ change are the same. In these cases only the temperature affects the models.

Based on these sensitivity analysis results, *the parameters E_0, K_1, K_2 and Q will be involved in parameter estimation*, while R will be fixed to its nominal value.

3.2.3 Parameter estimation

Based on the modeling and analysis results of Sections 3.2.1 and 3.2.2 the parameter estimation method will be performed using the simplified model (3.17)-(3.19) without the temperature dependence of the parameters, i.e. point estimates will be determined based on measurement data obtained at different temperatures. The obtained point estimates of the parameters at the different temperatures will then be used for determining the thermal characteristics of the parameters.

Input signal The selection of the correct input signal is crucial in any parameter estimation procedure as the sufficient excitation is the key to the successful parameter estimation. In the work [141], the optimal excitation has been presented for the estimation of battery parameters important from the aging point of view. It was shown using the Fisher information and the Cramér-Rao inequality, that pseudo-random binary sequences are optimal for the estimation of such parameters. Although the aim and the parameter set is different in this case, PRBS inputs are used. It is a widely used signal in the field of parameter estimation [67] because it is easy to generate and provides sufficient excitation. The PRBS has only two values in between the signal changes randomly. The two parameters of the PRBS are the range (the upper and lower level of the signal) and the frequency of the change that should be chosen considering the system dynamics.

An other important factor of the parameter estimation method is the ambient temperature which is chosen to be constant during an experiment.

The minimum and maximum battery temperatures of the experiments should be chosen according to the recommended operating temperatures of the examined battery. Then this range is evenly divided to get the list of ambient temperatures at which the experiments should be carried out.

Method The proposed parameter estimation method consists of two steps. At first the battery is charged or discharged at different constant ambient temperatures. At each temperatures the parameters E_0, K_1, K_2 and Q of the battery are estimated. In the second step the temperature coefficients of these parameters are estimated.

Estimation of the battery parameters The first step is the estimation of the battery parameters at different constant ambient temperatures to see how these parameters change with that temperature. The inputs of the parameter estimation are the battery current and voltage at different temperatures during a full charge or discharge process. The result of the estimation is a vector of battery parameters at different temperatures.

It can be seen from (3.17-3.19) that the battery model has a nonlinear output equation and four parameters to be estimated as the internal resistance R has bene fixed to its nominal value. Therefore a suitable nonlinear parameter estimation method should be chosen. In this work the nonlinear least-squares method is chosen. Nonlinear parameter estimation problems are usually solved as nonlinear optimization problems where a suitable prediction error functions of the model, the measurement data and the parameters are minimized in the parameter space. In the present case the prediction error function is the sum of squared deviation between the model and the measurement data at every time instance (see (3.28) below)

$$J(\theta) = \frac{1}{N} \sum_{k=1}^{N} \left(\hat{v}_b[k] - v_b[k;\theta] \right)^2 , \tag{3.28}$$

where $\hat{v}_b[k] = \hat{v}_b(k\,\tau)$ is the measured value of the battery voltage at the k^{th} sample, $v_b[k;\theta]$ is the output of the model at the same sampling instant with the parameter vector $\theta = [E_0, K_1, K_2, Q]$, and N is the total number of samples. It is important to note, that the two operation modes have to be treated as separate parameter estimations, i.e. one set of parameters are to be estimated from the charge measurements and the charge model, and another one is from the discharge data and model.

As all of the parameters to be estimated have physical meaning, the range and scale of the parameter values are usually known in advance. Therefore upper and lower bounds for the parameters can be defined that is useful to limit the searching space of the optimization. As a result, a constrained nonlinear optimization problem should be solved. From the potential algorithms the Trust Region Reflective algorithm [13] is chosen in this work.

Estimation of the temperature dependency of the parameters The second step of the parameter estimation method is the estimation of the reference values and the temperature dependency coefficients of the parameters. The inputs of this parameter estimation problem are the estimated parameters at different temperatures from the previous step. It can be seen from the temperature dependent battery model, that the battery parameters can be divided into two groups based on the type of their temperature dependency:

- Parameters with linear temperature dependency: E_0, Q.
- Parameters with nonlinear (exponential) temperature dependency: K_1, K_2.

Moreover it can be seen from (3.22-3.26) that some of the parameters (Q) depend on the ambient temperature and others (E_0, K_1, K_2) depend on the battery cell temperature. The problem is that the cell temperature is usually cannot be measured. To overcome this the *following additional assumptions are made*:

- The cell temperature does not change a lot during charge/discharge (maximum $\pm 2°C$).
- The cell temperature is substituted by the average surface temperature during charge/discharge.
- Initially the cell temperature and the ambient temperature are equal.
- The surface temperature of the battery is measured.

With the above assumptions the temperature coefficients of the parameters can be estimated. The *coefficients to be estimated* are:

- $E_0|_{T_{ref}}$ and $\partial E/\partial T$ for the temperature dependency of E_0
- $Q|_{T_{ref}}$ and $\Delta Q/\Delta T$ for the temperature dependency of Q
- $K_1|_{T_{ref}}$ and α_1 for the temperature dependency of K_1
- $K_2|_{T_{ref}}$ and α_2 for the temperature dependency of K_2

The coefficients of $E_0(T)$ and $Q(T_e)$ can be estimated with the simple linear least squares method because equations (3.26) and (3.25) are linear.

The coefficients of $K_1(T)$ and $K_2(T)$ can also be estimated by the least squares method by transforming the equations and their dependent variables.

3.2.4 Simulation study of battery parameter estimation

Simulation setup

The parameter estimation methods were implemented and tested by simulation experiments in Matlab. To simulate the thermal dynamics of the battery during charge/discharge, a more detailed was used to serve as the measurement data source for the parameter estimation. *This model contains additional energy balance equations* that describe the temperature effects of the battery [91]. Moreover, the battery cell temperature can be directly extracted from the model, which makes it suitable for parameter estimation purposes.

The simulated battery was a Samsung INR18650Q-20Q battery with 2000 mAh capacity. The nominal parameters of the battery can be seen in Table 3.5. The operating temperatures of the battery from the datasheet are $0-50°C$ for charge and $-20-75°C$ for discharge. Based on these values, the battery model was used between $0-50°C$. The charge and the discharge of the battery was simulated at 11 different ambient temperature values with PRBS input signal between 1-99% state of charge. The simulation setup in case of charge and discharge can be seen below.

Simulation setup for charge:

- PRBS input: $I_{min} = -4A$, $I_{max} = -0.5A$, $T_s = 160s$
- initial values: $q(t_0) = 0.99Q$, $i_f(t_0) = 0$, $T = T_e$
- ambient temperatures: $T_e = 0, 5, 10, 15, 20, 25, 30, 35, 40, 45, 50°C$
- stopping criterion: $q(t) = 0$;

Simulation setup for discharge:

- PRBS input: $I_{min} = 0.5A$, $I_{max} = 4A$, $T_s = 160s$
- initial values: $q(t_0) = 0.01Q$, $i_f(t_0) = 0$, $T = T_e$
- ambient temperatures: $T_e = 0, 5, 10, 15, 20, 25, 30, 35, 40, 45, 50°C$
- stopping criterion: $q(t) = 0.99Q$;

All the simulations were performed on a PC (Intel i5 CPU with 4 GB RAM).

Estimated battery parameters The battery parameters at different temperatures were estimated using the *lsqnonlin* function from Matlab Optimization Toolbox [76] that implements a Trust Region Reflective algorithm.

The function to be minimize is the cost function (i.e. prediction error) (3.28) and the parameters to be estimated are $\theta = [E_0, Q, K_1, K_2]^T$. The initial values of the parameters were set to the nominal parameter values (see in Table 3.5). The constraining inequalities (3.29) were defined for the optimization based parameter estimation.

$$\begin{array}{ccccc} 0 & \leq & E_0 & \leq & 5 \\ 0 & \leq & Q & \leq & 3 \\ 0 & \leq & K_1 & \leq & 0.1 \\ 0 & \leq & K_2 & \leq & 0.1 \end{array} \tag{3.29}$$

The results of the parameter estimation can be seen in Table 3.8. The accuracy of the parameter estimation can be characterized by the covariance matrix of the estimation. In the presented results the elements of the covariance matrices are really small (with orders between 10^{-8} and 10^{-12}) in both charge and discharge cases. This means that the parameter estimation is very accurate. Note, that the experimental data were obtained *from the simulation of the model equations of the extended model with energy balance equation* and not from real measurements, therefore no external noise or modeling errors are included.

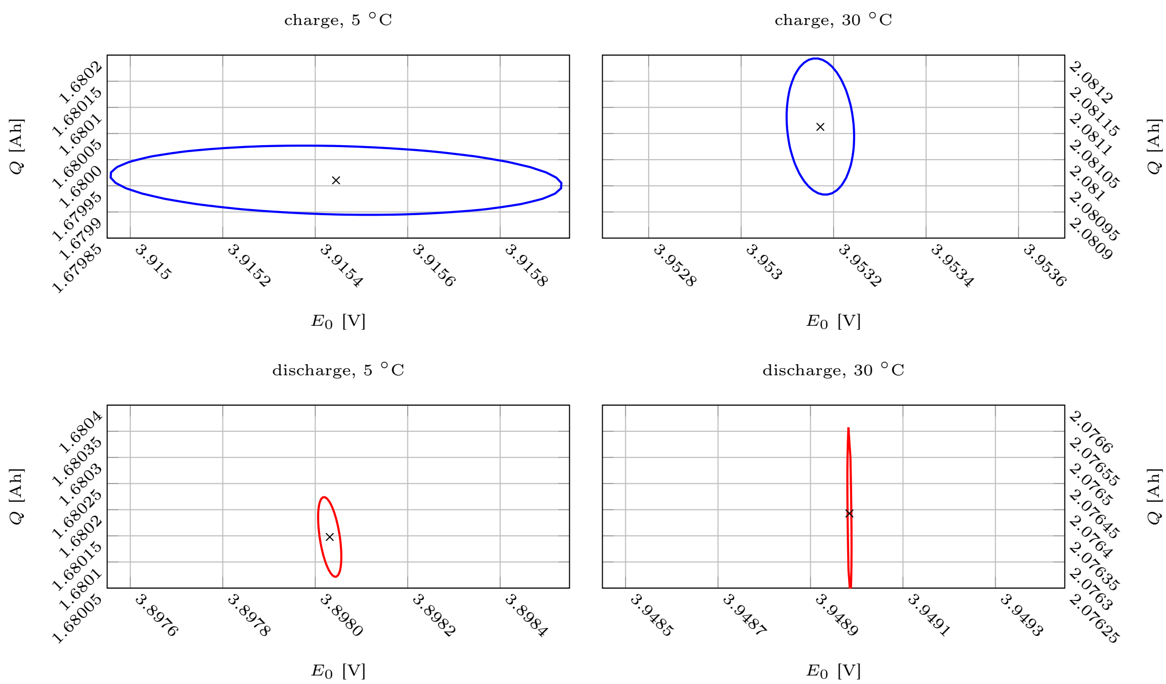

Figure 3.9: Confidence regions (solid line) of the parameter estimation for parameters E_0, Q during charge/discharge at different temperatures. The parameter estimate is represented by a $\times$. x axis range: $1 \cdot 10^{-3}$, y axis range: $3.5 \cdot 10^{-4}$.

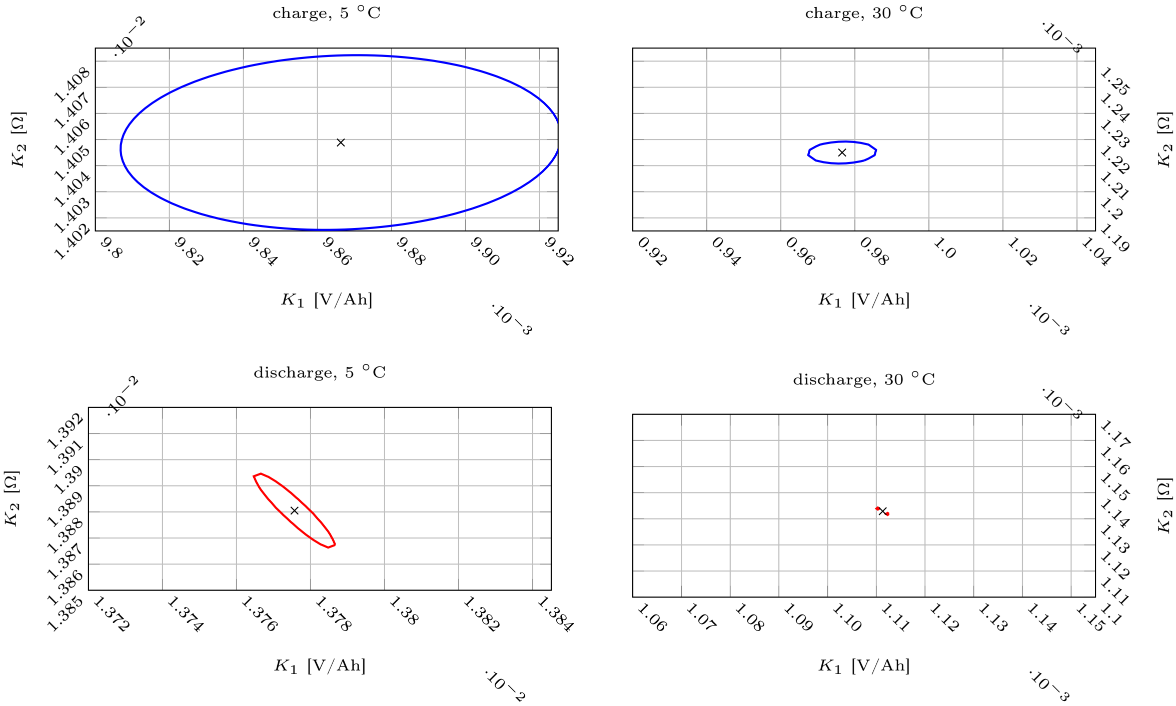

Figure 3.10: Confidence regions (solid line) of the parameter estimation for parameters K_1, K_2 during charge/discharge at different temperatures. The parameter estimate is represented by a $\times$. x axis range: $1.25 \cdot 10^{-4}$, y axis range: $7 \cdot 10^{-5}$.

Table 3.8: Estimated battery parameters at different temperatures during charge and discharge.

	charge				discharge			
T_e [°C]	E_0 [V]	Q [Ah]	$K_1 [V/Ah]$	$K_2 [\Omega]$	E_0 [V]	Q [Ah]	$K_1 [V/Ah]$	$K_2 [\Omega]$
0	3.9175	1.6001	0.0169	0.0246	3.8877	1.6010	0.0239	0.0243
5	3.9154	1.6800	0.0099	0.0140	3.8980	1.6801	0.0138	0.0139
10	3.9190	1.7599	0.0059	0.0082	3.9083	1.7599	0.0081	0.0081
15	3.9259	1.8399	0.0036	0.0049	3.9185	1.8393	0.0048	0.0048
20	3.9343	1.9201	0.0023	0.0030	3.9286	1.9188	0.0029	0.0029
25	3.9436	2.0004	0.0015	0.0019	3.9388	1.9980	0.0018	0.0018
30	3.9532	2.0811	0.0010	0.0012	3.9490	2.0764	0.0011	0.0011
35	3.9631	2.1623	0.0007	0.0008	3.9591	2.1540	0.0007	0.0007
40	3.9651	2.1576	0.0012	0.0000	3.9693	2.2300	0.0004	0.0005
45	3.9783	2.1579	0.0008	0.0000	3.9795	2.3035	0.0003	0.0003
50	3.9893	2.1582	0.0007	0.0000	3.9884	2.1583	0.0000	0.0000

The results are also depicted in Figure 3.11 with black dots. It can be noticed in the same figure that above 35 $°C$ ($T - T_{ref} = 10$) the battery reached its maximum capacity during charge.

The confidence region of the estimated parameters can be approximated by the $1.05 \cdot J(\theta_{min})$ contour line of the cost function (3.28). In order to analyse and illustrate the confidence regions, the parameters are analysed in in pairs. We fixed two parameters and computed the value of the cost function when changing the other two parameter values around their estimated value. The two parameters pairs were chosen as E_0, Q and K_1, K_2. Some examples of the confidence regions in case of charge/discharge at different temperatures are illustrated on Figure 3.9 and Figure 3.10. The order of magnitude on the x and y axes are the same in the plots of Figures 3.9 and Figures 3.10, respectively. Comparing the confidence regions at different temperatures and operating modes the following conclusions can be drawn:

- In case of both charge discharge, the confidence of Q increases while E_0 decreases as the temperature rises (see Figure 3.9).
- In case of charge, the confidence region of K_1, K_2 becomes smaller as the temperature rises (see Figure 3.10).
- A linear relationship between K_1 and K_2 can be assumed in case of discharge (see Figure 3.10).

Estimated temperature dependent parameters Having estimated the battery parameters at different ambient temperatures, the temperature dependency of the parameters was estimated with the help of the Matlab Curve Fitting Toolbox [75]. Each parameter has two coefficients that describe the temperature dependency: the parameter value at the reference temperature and the a temperature coefficient. The independent variables of the four different parameter estimation tasks are the following:

- $T - T_{ref}$, in case of $E_0(T)$;

- $T_e - T_{ref}$, in case of $Q(T_e)$;

- $\frac{1}{T} - \frac{1}{T_{ref}}$ in case of $K_1(T)$ and $K_2(T)$.

As it was mentioned in Section 3.2.3, the cell temperature T was substituted by the average surface temperature of the battery. The dependent variables are the estimated parameter values of the previous step that can be seen in Table 3.8.

The coefficients of the temperature dependency were estimated during both charge and discharge. The results of the estimation can be seen in Tables 3.9 and Table 3.10. The 95% confidence bounds shows the uncertainty of the estimated coefficients.

It can be seen that the estimated temperature dependency of E_0 and Q is close to the nominal nominal values in both charge and discharge cases. The estimation of $Q|_{T_{ref}}$ and $\Delta Q/\Delta T$ is better in case of charge because the differences between the nominal and estimated parameter are smaller. However the estimation of the other parameters is better in case of discharge.

The fitted curves of the temperature dependency can be seen in Figure 3.11 with blue solid line for the charge and red solid lines for the discharge cases, respectively. The goodness of fit was characterized by the r^2 value that is computed by:

$$r^2 = 1 - \frac{\sum_i (\hat{y}_i - y_i)^2}{\sum_i (\hat{y}_i - \bar{y})^2}$$

where $\hat{y}$ is the measured data, y is the model predicted value, and $\bar{y}$ is the mean of the measured data. The results can be seen in Table 3.11.
It can be seen that the curve fitting is a bit more accurate in case of discharge, except Q.

Table 3.9: Estimated parameters of the temperature dependency of the battery parameters during charge.

Parameter	Nominal value	Estimated value	95% confidence bounds	Unit
$E_0\|_{T_{ref}}$	3.9388	3.943	(3.94, 3.946)	V
$\partial E/\partial T$	$2.0 \cdot 10^{-3}$	$1.518 \cdot 10^{-3}$	($1.314 \cdot 10^{-3}$, $1.723 \cdot 10^{-3}$)	V/K
$Q\|_{T_{ref}}$	2.0	2.001	(2.0, 2.001)	Ah
$\Delta Q/\Delta T$	$1.6 \cdot 10^{-2}$	$1.605 \cdot 10^{-2}$	($1.601 \cdot 10^{-2}$, $1.610 \cdot 10^{-2}$)	Ah/K
$K_1\|_{T_{ref}}$	$1.8 \cdot 10^{-3}$	$2.735 \cdot 10^{-3}$	($1.866 \cdot 10^{-3}$, $3.604 \cdot 10^{-3}$)	V/Ah
α_1	8415	5989	(4684, 7294)	K
$K_2\|_{T_{ref}}$	$1.8 \cdot 10^{-3}$	$1.545 \cdot 10^{-3}$	($1.866 \cdot 10^{-3}$, $1.987 \cdot 10^{-3}$)	Ω
α_2	8415	9785	(8706, 10860)	K

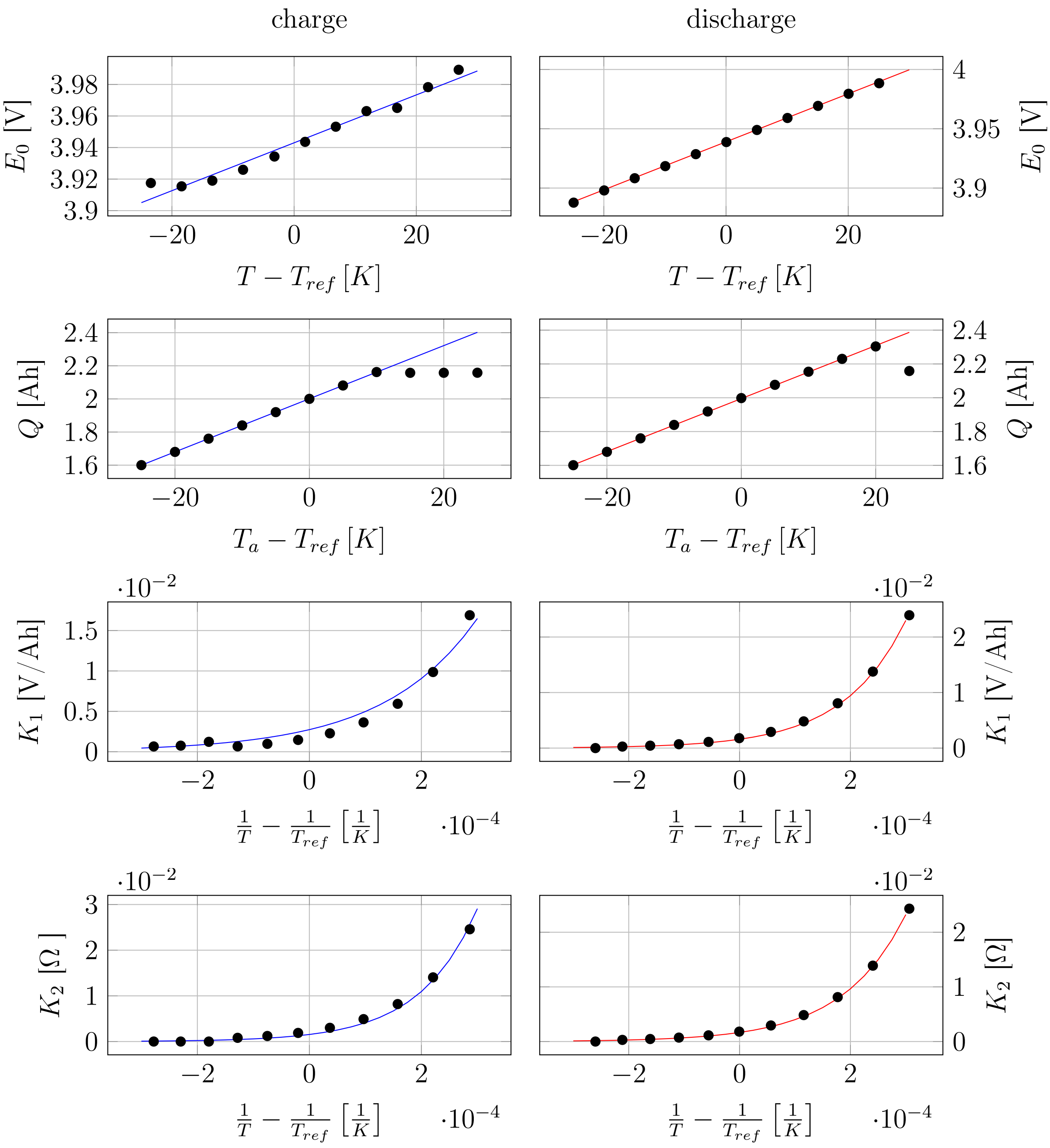

Figure 3.11: Parameter estimation and curve fitting results for all the estimated parameters. The left column corresponds to the results obtained from charge data while the right column is obtained from discharge measurements. The estimated parameter values are denoted by black dots, the fitted curves are denoted by solid lines (blue for charge and red for discharge).

Table 3.10: Estimated parameters of the temperature dependency of the battery parameters during discharge.

Parameter	Nominal value	Estimated value	95% confidence bounds	Unit
$E_0\|_{T_{ref}}$	3.9388	3.939	(3.938, 3.939)	V
$\partial E/\partial T$	$2.0 \cdot 10^{-3}$	$2.025 \cdot 10^{-3}$	($2.009{\cdot}10^{-3}$, $2.041{\cdot}10^{-3}$)	V/K
$Q\|_{T_{ref}}$	2.0	1.995	(1.993, 1.997)	Ah
$\Delta Q/\Delta T$	$1.6 \cdot 10^{-2}$	$1.568 \cdot 10^{-2}$	($1.554{\cdot}10^{-2}$, $1.581 \cdot 10^{-2}$)	Ah/K
$K_1\|_{T_{ref}}$	$1.8 \cdot 10^{-3}$	$1.588 \cdot 10^{-3}$	($1.418{\cdot}10^{-3}$, $1.757{\cdot}10^{-3}$)	V/Ah
α_1	8415	8908	(8528, 9289)	K
$K_2\|_{T_{ref}}$	$1.8 \cdot 10^{-3}$	$1.661 \cdot 10^{-3}$	($1.542{\cdot}10^{-3}$, $1.781{\cdot}10^{-3}$)	Ω
α_2	8415	8793	(8538, 9048)	K

Table 3.11: The measure of fit characterized by the r^2 value.

	E_0	Q	K_1	K_2
charge	0.9691	1	0.9656	0.9925
discharge	0.9999	0.9999	0.9995	0.9988

3.3 Summary

Model based methods have been proposed in this chapter for different electrical systems. Although the investigated system and the application area is different, the common methodological background is the same: (i) the use of a mathematical model of the system in hand (ii) and the optimization related nature of the problem.

In the first part of the chapter (Section 3.1) the cost-optimal operation of home appliances has been aimed. The proposed method is applicable for continuously operating electrical equipments with similar dynamics. Taking into account the properties of the dynamical system to be controlled (scheduled), a model predictive heuristic scheduling algorithm was formulated. The results illustrate that the developed algorithm has a reasonably fast runtime due to the proposed heuristic branch and bound type optimizer, and can achieve lower operating costs. The proposed algorithm is able to carry out cost-optimal operation schedule, even in an environment with variable energy prices.

As a next step, the proposed model predictive scheduler has been extended with an adaptivity feature that enables the re-estimation of certain parameters in the predictive model of the method. The adaptive heuristic optimal scheduler has been investigated in simulation experiments for the case of a refrigerator, where the varying heat capacity of the controlled system was successfully followed by the proposed optimization method.

Afterwards, in Section 3.2 the focus was shifted towards lithium-ion batteries and their parameter estimation in the presence of temperature change.

A parameter estimation method has been proposed that is capable of identifying the thermal behavior of lithium-ion batteries. The basis of the method is a nonlinear charge and discharge model which describes the temperature dependency as a parametric function of temperature as an external variable.

The proposed parameter estimation method contains two steps. At first the corresponding parameters are estimated from measured data of charging/discharging at different constant ambient temperatures. In the second step the temperature coefficients of these parameters are estimated.

The proposed parameter estimation method is verified by a set of simulation experiments on an electro-thermal battery model capable of describing the thermal behavior of the battery. The temperature dependent parameter characteristics obtained generated by the proposed method can be used as a computationally effective way of determining the key battery parameters at a given temperature.

Chapter 4

Model-free optimal operation of complex energy systems

Although model based methods discussed in Chapter 3 are promising tools for the optimal operation of energy systems, in some cases the properties of system to be controlled disables the development of a computationally effective and precise model. The expectation of optimal operation nonetheless exists for such systems. Electrical networks with stochastically changing loads and generators are difficult to describe with dynamical models. On the other hand, power quality problems such as total harmonic distortion due to the increasing number of nonlinear capacitive loads, or voltage unbalance problems due to the non-uniform distribution of prosumers on the phases provide several optimization problems to be solved in a model free manner.

Single phase power injections to the grid are mainly generated by domestic photovoltaic and wind power plants. Several studies address power inputs to the energy grid, see e.g., [17] for a recent survey. For off-grid, sometimes more complex solutions integrating diesel generators, photovoltaic (PV) and wind generators. Such as proposed, in [94], and [22], where presented the economical aspects of a PV system. The economic results are strongly influenced by the annual average insolation value, which encourages the areas most exposed to the sun and the southern areas. The consumption of consumers is not critically important, but the design principle used has as significant effect on the maximization of the performance of PV plants. In the paper [52] it is worth noticing, that autonomous photovoltaic systems are strongly responsible of their reactive energy requirements. To support photovoltaic systems with sufficient battery banks one should be able to establish that their reactive energy requirement share is fairly compensated by the corresponding energy yield. Additionally, in [82] the author emphasizes that PV systems are increasingly being deployed in all over the world, and this is the source of a wide range of power quality problems. With a view on consistently measuring and assessing the power quality characteristics of PV systems, they had presented an in-depth overview and discussion of this topic. The possibility of power factor correction occurring in conjunction with power injection has also been addressed [68],[32],[18], and the relationship between power injection and nonlinear distortion reduction (harmonic control) has also been explored in [64] and [65], where the authors use a DSP based current control technique to reduce distortion with active power filters (APF) and compensate for an exact nonlinear load. Sensing the nonlinear current time function and the ideal sinusoid current with a phase-locked loop technique, they inject the exact deviation current into the grid with a significant reduction in distortion.

A numerical study was done by [84] on the distribution network faults and the effects on unbalance factor and the matrix representation of network impedances with the symmetrical component and phase component method. The study concluded, that during fault voltages and currents are greatly affected by the system unbalance and the fault impedance. The increase of the system unbalance causes an increase of the during-fault voltages and currents variation. The increase of the fault impedance reduces the fault current and therefore the effect of the system unbalance on during fault voltages and current diminishes. For each system there is a characteristic value of fault impedance that is related to the load impedances. Larger fault impedances values produce fault currents similar to nominal load currents and therefore the effect of these faults in terms of during-fault voltages and currents cannot be differentiate from nominal operation conditions. Variation of power quality in non-faulty scenarios leads to thermal transients in electrical machines. This problem can be especially important in the case of low-power machines, because they have shorter time constants than high-power ones. The rate of thermal responses of a machine also significantly depends on the type of power quality disturbances. Voltage unbalance can cause machine overheating within a mere few minutes. Furthermore, fluctuating unbalance could cause an extraordinary rise in windings temperature and additional thermo-mechanical stress. Consequently, voltage unbalance is found to be more harmful to induction motors than the results from previous work [34]. Additionally beside the heat factor, voltage unbalance can cause increased reactive power [90], various copper loss [96] torque pulsation in electric motors [12]. The authors of [63] were discussing the effects of unbalanced voltage on a three-phase induction motor, one has to consider not only negative-sequence voltage but also the positive-sequence voltage. With the same voltage unbalance factor, the status of voltage unbalance could be judged by the magnitude of positive sequence voltage. Also the effect of voltage unbalance has been studied on three-phase four-wire distribution networks for different control strategies for three-phase inverter-connected distributed generation units on voltage unbalance in distribution networks [78]. Here the negative-sequence component and the zero sequence component were studied where unbalance conditions could lower stability margin and increasing the power losses. On the other hand, the adaptive coordination of distribution systems included distributed generation is also an emerging problem as it was discussed by [6]. A small voltage unbalance might lead to a significant current unbalance because of low negative sequence impedance as highlighted in [9].

Many authors present a different viewpoint of calculating unbalance on the network. [73] showed to assess the harmonic distortion and the unbalance introduced by the different loads connected to the same point of common coupling have been applied to an experimental distribution network. By [55] the focus was to bring out the ambiguity that crops up when a particular value of voltage unbalance is referred that exists in the system. By making use of the complex nature of voltage unbalance, the voltage combinations that lead to the calculation of complex voltage unbalance factor could be narrowed down to a great extent. A fast and accurate algorithm for calculating unbalance has been presented by [115]. The magnitudes of zero, positive, and negative sequences are obtained through simple algebraic equations based on the geometric figure, which is also called as 4 and 8 geometric partitions. Also a three-phase optimal power flow calculation methodology has been presented by [3], that is suitable for unbalanced power systems. The optimal algorithm uses the primal-dual interior point method as an optimization tool in association with the three-phase current injection method in rectangular coordinates.

4.1 Renewable based total harmonic distortion compensation

In case of residential prosumers the flow of electrical energy is bidirectional at the power meter. They use electricity from the grid if it is necessary, but the excess energy is fed back to the electrical network through an inverter. With the rise of electric vehicles, high capacity energy storage may also be available in the household.

The general aim is to develop and investigate optimization-based methods for complex electrical energy systems composed of renewable energy sources and batteries, with the idea that these technologies can also perform power quality improvement in the line without the need for current measurement (which is usually not available in real-world situations). In such cases the time domain approach of the active power filtering method [26], or [37] cannot be applied since the domestic power plant typically connects to the electrical network *after the power meter*, so the current waveform cannot be measured easily. The use of voltage waveform and its power quality indicators allows the compensation and reduction of the consequences of the nonlinear distortion present in the whole low-voltage transformer area, and not just the distortion present in the current sensing connection point.

4.1.1 Problem statement

Based on the above, the aim is the formulation of power injection to the grid as a direct optimization problem, where the output of the inverter is a general current waveform $i_{out}(t)$ which minimizes a measure of power quality that is calculated from the voltage measurements $v_{net}(t)$ available at the network connection point.

It is expected that the solution of the optimal power injection problem is capable of compensating the unwanted nonlinear distortion effects caused by capacitive bridge rectifiers mentioned in Section 2.1.1.

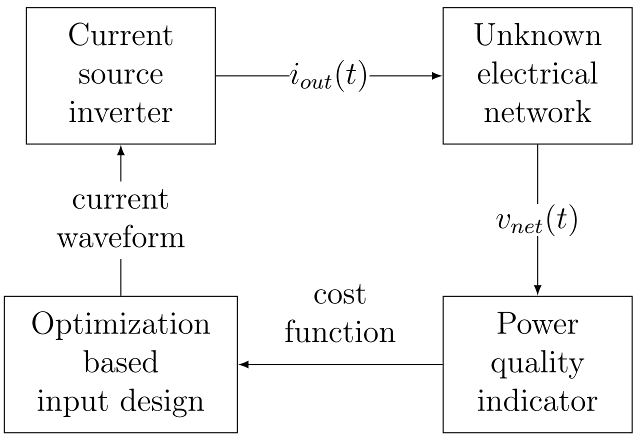

Figure 4.1: High level structure of the compensation problem.

The direct optimization based structure of Figure 4.1 proposes a possible structure for the solution of the above problem. The key elements of the structure are discussed in the sequel.

Current source inverter The current source inverter block of the figure implements the current waveform determined by the Optimization based input design block and feeds it into the grid as the current i_{out}. This module also represents the available electrical energy that can originate from different sources

- domestic solar power plant
- domestic energy storage equipment (battery bank, electric vehicle, etc.)

Electrical network The electrical grid is supposed to be one-phase, the only assumption is that the voltage $v_{net}(t)$ can be measured at the network connection point. Since the network units (generators and loads) are continuously switching on and off the network in an unobservable and uncontrollable manner, the model structure as well as the model parameters of the network cannot be determined using the tools of system identification. *An important assumption that has to be made with respect to the transient response of the network is that the effect of the input decays by the time the next input is applied to the network.* This cannot be ensured in the general case since the network is unknown.

Power quality indicator This scalar quantity serves as the cost function J_{PQ} of the optimization problem. In principle, any power quality indicator can serve as the cost function that can be calculated from v_{net} as $J_{PQ}(v_{net})$.

Optimization based input design The optimizer is the key element of the problem in hand, it solves the optimization problem (4.1) iteratively

$$\min_{i_{out}} J_{PQ}(v_{net}) \tag{4.1}$$

where J_{PQ} stands for the applied power quality norm as a cost function. A more sophisticated input design method would also take into account the constraints on the applicable current, which is naturally connected to the parameters of the inverter, the power of the solar panel, battery state of charge, etc. The use of such constraints are an interesting connection point to further research topics, but they are out of the scope of the present thesis.

4.1.2 Detailed THD compensation structure

The grid-tie inverter circuit connecting the renewable photovoltaic energy source to the main grid [68] used as the fundamental element of the method, is shown in Figure 4.2. This model contains a simple booster stage with an Isolated Gate Bipolar Transistor (IGBT) bridge connected to the grid with serial inductance. A more detailed version of this inverter can be seen in Figure A.4 of the Appendix, where the battery charger circuit is also presented.

The inverter is being driven by the switching sequence of switches $S_1 - S_4$ and $S_2 - S_3$. Another important element of Figure 4.2 is the intermediate circuit capacitor which serves as a puffer between the current sources (e.g. solar panel, battery) and the output. Although the power electrical details of the inverter model is a very interesting problem, from the point of view of the optimization based compensation problem it is regarded as the actuator implementing the current waveform.

In order to have a more detailed yet still conceptual structure for the problem defined in Section 4.1.1, some additional elements are necessary for the system. The

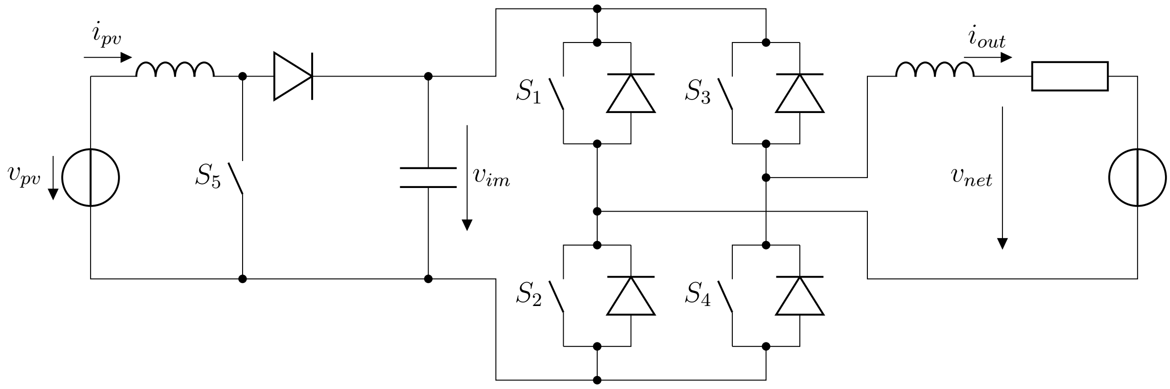

Figure 4.2: Grid-tie inverter model that connects the renewable photovoltaic energy source to the main grid

structure of the system is given in Figure 4.3, where the basic assumption of unknown electrical network is still valid, i.e. the only information available from the network is the voltage v_{net} measurable at the connection point.

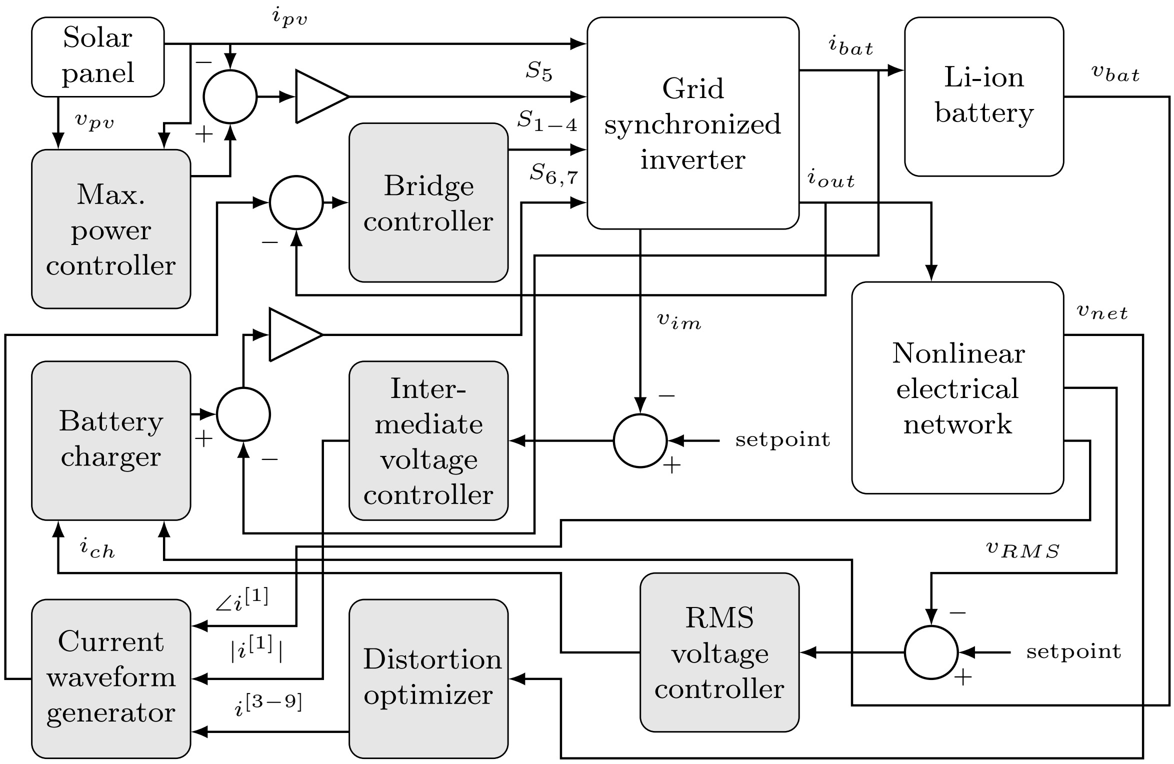

Figure 4.3: Block diagram showing the functional parts of the compensation structure supplemented with a solar panel and a battery connecting to a nonlinear electrical network.

The compensator system controlling the inverter is divided into seven main functional parts as shown by the grayed boxes in Figure 4.3. Some general components are only presented because they are needed for the normal operation of the network, the novel element is the Distortion optimizer described below.

Maximum power controller This component is a general part of the control system and is independent of the other control parts. Its only task is to operate the renewable power source (i.e., photovoltaic panel or wind generator) at the optimal working point in any wind and solar condition to obtain the maximum amount of electric power from the source. The output of the maximum power controller is determined by the input current setpoint of the inverter. It has a simple on/off switching nonlinear hysteresis controller for input current control [64].

Charger controller This part of the control system is also independent of the other control parts. It is responsible for controlling the switching element S6 in the bulk converter (Figure 4.2) in order to adjust the convenient charging current value of the battery. Like the maximum power controller, it also has a simple on/off switching nonlinear hysteresis controller [64].

Intermediate voltage controller This component measures the intermediate circuit voltage v_{im} and senses the difference between the measured value and the setpoint value. The controller changes the fundamental harmonic magnitude of the injected current using a simple proportional controller that is based on the difference between the measured and setpoint values. Higher-order components are not used by the upper harmonic controller given that they have no effect on the intermediate voltage. This controller adjusts the effective power injection to the grid in 20 ms cycles.

RMS voltage controller This component controls the effective voltage value v_{RMS} at the connection point. This controller is needed because insufficient power generation and overloads reduce voltage in the low-voltage line, while overproduction increases the voltage in this line. It is a proportional-integral controller. Its manipulated value is the charge or discharge current value of the battery.

Current waveform generator Based on the current harmonics magnitude and phase values from the Distortion optimizer this block calculates the exact waveform to be injected into the grid. This waveform is the setpoint of the bridge current controller.

Bridge controller The bridge controller calculates the difference between the measured output current and the output current setpoint and switches the IGBT bridge two half's control signal (S_1-S_4, S_2-S_3) on and off. This latter function is accomplished using a simple Schmitt trigger comparator with a simple on/off switching hysteresis controller [64].

Distortion optimizer It is the main element of the detailed structure, corresponding to the optimizer block appearing in the structure given in Figure 4.1. It calculates the frequency domain behavior of the voltage is monitored at an assigned point by measuring the the inverter's output voltage v_{net} and calculating the magnitude and phase of the 3rd, 5th, 7th and 9th harmonic components. Its outputs are the base harmonic output current and the magnitudes and phases of the 3rd, 5th, 7th and 9th high order components. These current harmonic components are the solution space of the optimization problem (4.1).

The above blocks influence each other directly in addition to some measurable voltages and currents of the inverter (see Figure 4.3).

4.1.3 Nonlinear distortion compensation as an optimization problem

The Distortion optimizer calculates the necessary optimal amplitudes and phases of the 3rd, 5th, 7th and 9th output current components. The optimization to be solved is the minimization of the cost function (4.2)

$$J_{PQ}(v_{net}) = \sum_{i=3,5,7,9} |v_{net}^{[i]}|^2 \tag{4.2}$$

where $|v_i|$ are the amplitudes of the 3rd, 5th, 7th and 9th upper harmonic output voltage components. This means, that zero values for the 3rd, 5th, 7th and 9th voltage harmonics would be optimal in order to attain the sinusoidal voltage and current shape of a linear power system.

The solution space of the optimization problem is the eight dimensional space of the magnitudes and phases of the output currents 3rd, 5th, 7th and 9th harmonic components. The output current is the waveform (4.3) below.

$$i_{out}(t) = |i^{[1]}| \sin(\omega_1 t + \angle i^{[1]}) + \sum_{k=3,5,7,9} |i^{[k]}| \sin(\omega_k t + \angle i^{[k]}) \tag{4.3}$$

where $i^{[1]}$ denotes the base harmonic current with $\omega_1 = 2\pi f$ angular speed ($f = 50\,\mathrm{Hz}$), and $i^{[k]}$ represents the k^{th} higher order harmonic component of angular speed $\omega_k = k\,\omega_1$.

It was found that changing the amplitudes and phases of any of the output current components investigated in this thesis influenced all of the components of the connection point voltage. This can be attributed to the nonlinear nature of the network.

It is important to emphasize the use of odd higher-order components (up to the 9th), despite the fact that distortion is only present in the 3rd and 5th higher-order components. This was done due to previous experience with a simpler method [127] which showed that the compensation algorithm can push distortion towards higher-order components that were originally not affected.

As the cost function (4.2) implicitly comprises the unknown electrical network, there is no hope for using optimization methods applies the derivative of the cost function (e.g. gradient method). In such cases derivative-free methods are used for optimization. Asynchronous parallel pattern search (APPS) is one such method (see Section 2.3.2). For the sake of simplicity, the unconstrained optimization problem is solved, however, in a real life application, the problem should be formulated and solved as a constrained optimization problem where the power and operation limits of the input naturally defines the constraints.

An optimization cycle consists of eight steps in which each of the above parameters is changed to conform with the direction of its parameter gradient. The parameters of the upper harmonic controller then converge to a value in the eight dimensional parameter spaces that correspond to the minimal cost function value.

Let us define the mapping (4.4) from the optimization variables (i.e. the magnitudes and phases of the 3rd, 5th, 7th and 9th higher-order current components) to the measured v_{net} voltage at the connection point. It means, that f_{net} represents the current waveform generator, the inverter, and the nonlinear network in one mapping, in order to simplify the notations of Algorithm 4.

$$v_{net} = f_{net}(i^{[k]}) \tag{4.4}$$

Of course, the actual functional form of f_{net} is unknown.

Algorithm 4 Optimization algorithm for nonlinear distortion compensation

procedure APPS-THD
  $i^{[k]}(0) = 0\angle 0,\ \Delta_k(0) = 0, d_k(0) = 1$
  while $J_{PQ}(f_{net}(i^{[k]}(q) + \Delta_k(q)d_k(q))) \neq 0$ **do**
    for k=3,5,7,9 **do**
      $d_k(q) = 0.5(\text{sign}(N(q-3) - N(q-2)) + \text{sign}(N(q-4) - N(q-3)))$
      $\Delta_k(q) = n_k N(q-1)\Delta_k(q-1) + \Delta_k(q-2) + m_k N(q-1)$
      $N(q) = J_{PQ}(f_{net}(i^{[k]}(q) + \Delta_k(q)d_k(q)))$
      if $J_{PQ}(f_{net}(i_k^{[k]}(q) + \Delta_k(q)d_k(q))) < J_{PQ}(f_{net}(i^{[k]}(q)))$ **then**
        $i^{[k]}(q+1) = i^{[k]}(q) + \Delta_k(q)d_k(q)$
      end if
    end for
    q++;
  end while
end procedure

Δ_i the process step length i.e. the value of the current vector's amplitude or angle needs to be changed for a successful step, and d_i is the corresponding step's signed direction vector, which specifies the applied changes direction. The function N represents the cost function (4.2) value as the network responses to the current injection, and n_i, and m_i are scaling gains for the corresponding process. The algorithm is initialised with $i^{[k]}(0) = 0\angle 0$, $\Delta_k(0) = 0$ for a smooth start, due to lack of prior knowledge about the network.

The parameter is $i^{[k]} \in \mathbb{C}, k = 3, 5, 7, 9$, and the initial search pattern $\mathbf{p} \in \mathcal{D} = \{d_1, ...d_n\}$ is taken from a predefined finite set, and updated every iteration. In this case, the error function values of N should be calculated for each pattern $\mathbf{p}$ in the set $\mathcal{D}$. As the competing directions are different, if there is not enough computing power available for direction vector $\mathbf{p}$, synchronization should not be maintained. This is the so-called asynchronous case. In the case of the proposed compensator, an individual $\mathbf{p}$ vector is defined for each output variable, and the optimization was performed in each direction asynchronously and shifted in time. Most likely, the cost function has a single local minimum as a symmetric amplitude and phase values. Approaching the minimal value of norm, the method uses adaptive increments that are proportional to the cost function value itself.

4.1.4 Simulation based performance and robustness analysis

In order to analyze the proposed optimization based compensator, a high fidelity simulation model has been developed that contains a dynamical model of the elements of the system presented in Figure 4.3. The network is described with a simple model with three different types of nonlinear capacitive loads representing several appliances using the capacitive input stage introduced in Section 2.1.1. The dynamical simulation network has been implemented in Matlab Simulink using the Simscape Electrical blockset. The details of the simulator go beyond the scope of the thesis, but some details are presented in Section A.2.2. The top level block diagram of the model can be seen in Figure A.5.

Performance of the method

In the first set of experiments, the overall operation and the performance of the method has been investigated. In order to do this, a nonlinear capacitive load was connected to the simulated network at $t = 0$. The value of the load parameters correspond to that of Load_1 in Table 4.1. It can be seen in Figure 4.4, where the cost function value

Table 4.1: Parameters of the capacitive loads applied during the simulation experiments.

parameters	Load_1	Load_2	Load_3
R_{load} [Ω]	25	50	35
C [mF]	10	5	7

(4.2) jumps above 60^2 as the loads are changed on the network. In a three seconds, the algorithm manages to decrease the cost function value below $10\,\text{V}^2$. In the bottom plot of the same figure the total harmonic distortion is presented which shows a similar decreasing behavior due to the distortion compensator.

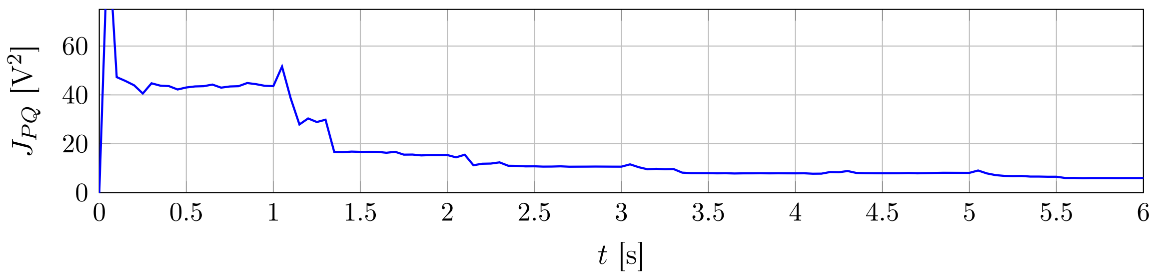

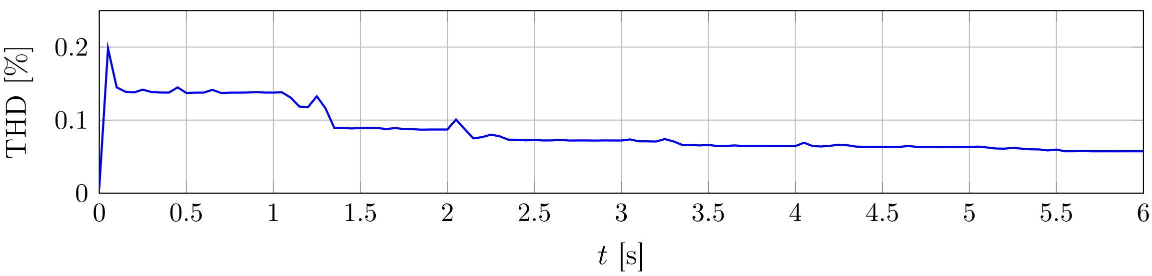

Figure 4.4: The load switching sequence during the simulation (top), the cost function during the robustness experiment (middle) and the total harmonic distortion (bottom).

A more detailed view of the operation is available in Figure 4.4 where the top and the middle plots show the output current i_{out} upper harmonic component magnitudes and phases changed according to Algorithm 4. The value of the cost function 4.2 can be seen in the bottom. It is easy to see, that the proposed direct optimization based method successfully decreases the cost function value of the network in this experiment.

It can also be seen in Figure 4.5 how the APPS algorithm steps are performed one after another shifted in time. One whole cycle takes 0.8 s, the amplitudes and the phases are optimized one after another for all injected current harmonics (four in this case).

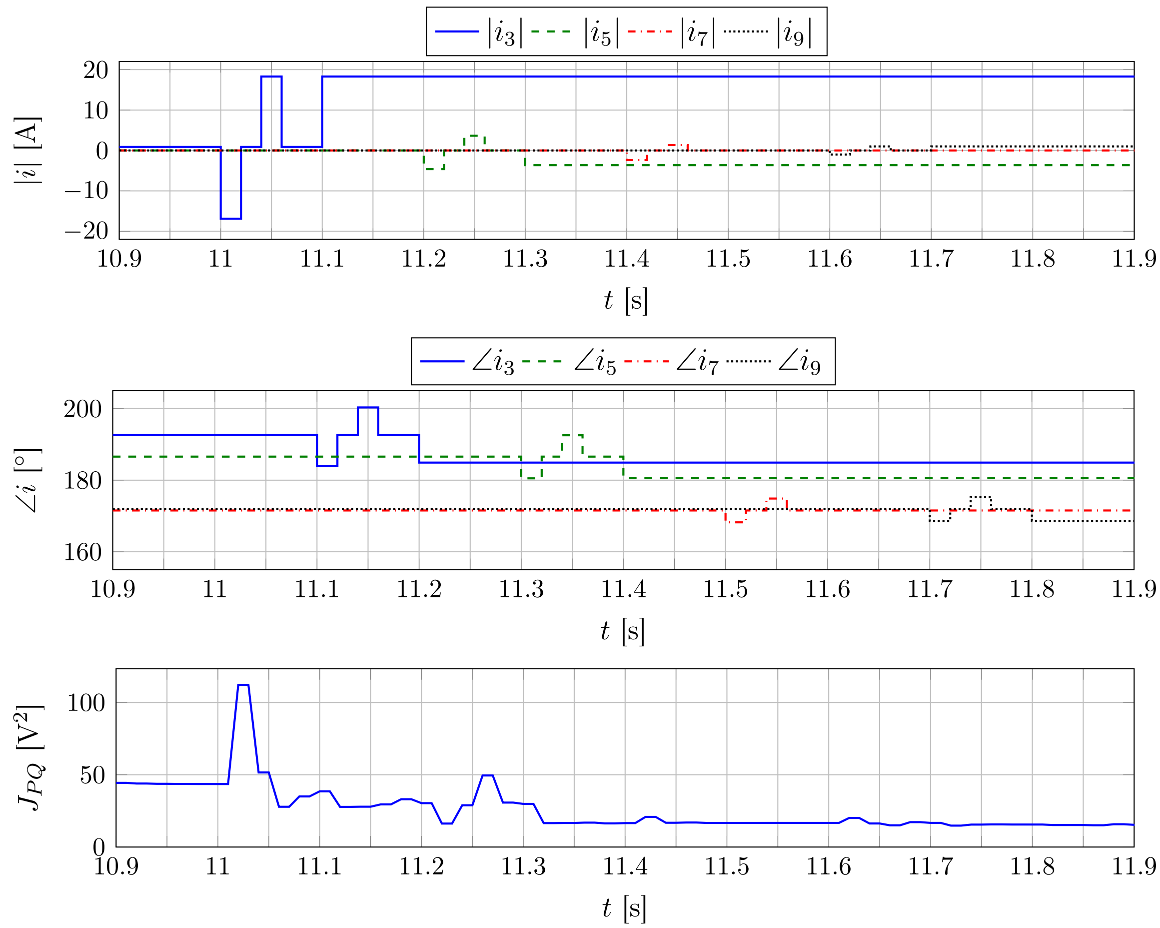

Figure 4.5: Output current parameters and error function during the operation of the optimization algorithm under robustness analysis. The current magnitudes and phases of the 3$^{\text{rd}}$, 5$^{\text{th}}$, 7$^{\text{th}}$ and 9$^{\text{th}}$ upper harmonic components can be seen in the two subplots (magnitudes in the top plot, phases in the middle plot).

Robustness against time-varying load conditions

Although the algorithm preformed well in the previous experiment, in a real life situation the loads and sources connected to the network are switching on and off according to different schedules in a stochastically changing manner.

Table 4.2: Switching sequence of the nonlinear loads during the experiment.

time interval	0-10 s	10-20 s	20-30 s	30-40 s	40-50 s	40-50 s
Load$_1$	OFF	ON	OFF	OFF	OFF	OFF
Load$_2$	OFF	OFF	OFF	ON	ON	OFF
Load$_3$	OFF	OFF	OFF	OFF	ON	OFF

The model's robustness against time-varying load conditions of the network was tested in a simulation experiment in which different capacitive loads representing several consumers are connected on and off the network according to the schedule in Table

4.2. The load parameter values are listed in Table 4.1. Figure 4.6 shows the results of the simulation. The schedule of the different loads can be seen on the top. The middle and the bottom plots show the value of the cost function (4.2) and the THD, respectively. It can be concluded, that the optimizer compensates the effect of the different nonlinear loads successfully.

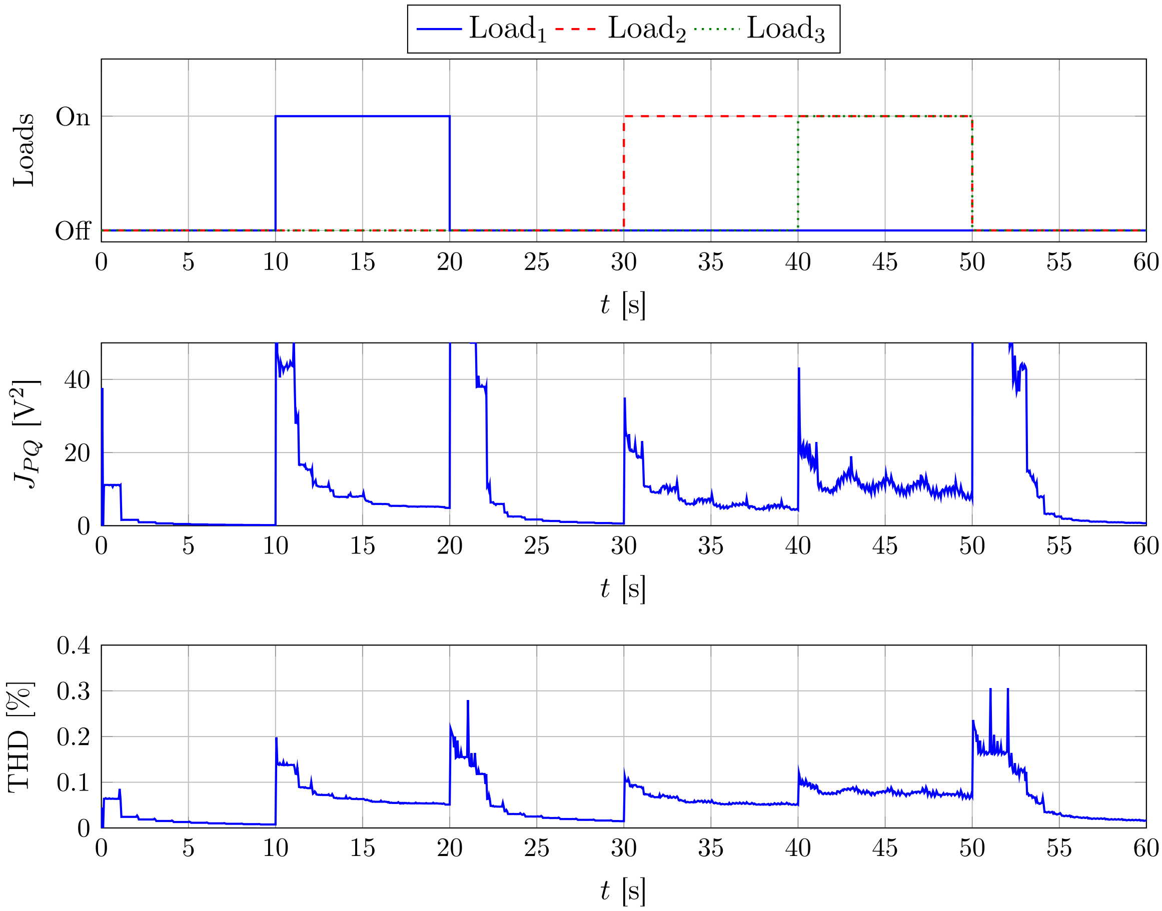

Figure 4.6: The load switching sequence during the simulation (top), the cost function during the robustness experiment (middle) and the total harmonic distortion (bottom).

Robustness against the parameters of the capacitive input stage

The robustness of the proposed compensation method is an important qualitative property with respect to the parameters of the controlled system components (i.e., the capacitive input stage and the loads). Because of the nonlinearity and hybrid nature of the controlled electrical circuit model,the robustness of the proposed upper harmonic controller had to be investigated in a series of simulation experiments.

The uncertainty related to the control problem statement can best be described by applying *parametric uncertainty bounds* to the resistance R_{load} and the capacitance C of the capacitive input stage, given that both are major sources of distortion:

$$\mathcal{D}_{R,C} = \{(R_{load}, C)|5 \leq R_{load} \leq 1000\ \Omega, 1 \leq C \leq 40\,\text{mF}\}$$

The above domain was defined by the distortion measurements obtained during the building of the proposed electrical network, and the measurement records are shown

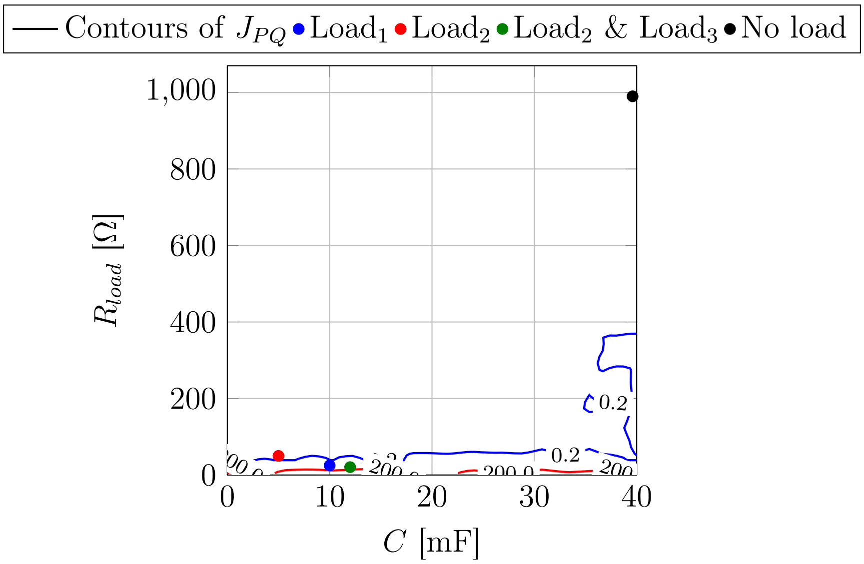

Figure 4.7: Robustness domain: the control performance as a function of the parameters R and C. The blue contour line corresponds to the cost function value $0.2\,\mathrm{V}^2$.

in Figure 4.7. The compensator's performance was evaluated based on the overall system stability and the satisfaction of several minimum performance requirements. The control performance is given in terms of the cost function (4.2) that is related to the energy of the higher-order harmonic components.

The domain of robustness is estimated by performing several dynamical simulations of the network and the compensation method where the parameters of the network load were chosen from a dense grid of the domain $\mathcal{D}_{R,C}$. The cost function values reached by the optimization based compensation method over a predefined time interval form the values of the discretized surface. The level sets of the cost function are depicted in Figure 4.7, which shows that the domain of robustness (i.e., the domain where the cost function is less than $0.2\,\mathrm{V}^2$) almost covers the entire domain.

4.2 Renewable based network asymmetry compensation

Most of a household's possible renewable sources and loads are unevenly distributed, without mindful control over single phase power converters. Some of these could represent an unevenly high power consumption, or a locally significant energy source, especially outside peak time zones of consumption. The situation is further complicated by the stochastic on/off switching of the different types of loads. This cause stochastic disturbing unbalance in the load currents which cases unbalanced load of the low voltage transformer, and amplitude- and phase unbalance in the voltage phasor trough the serial impedance of the low voltage transportation line wires and connecting devices cables.

Due to the unregulated, and uneven load, or (with the emergence of affordable PV stations) possible domestic power plant distribution, the voltage and current unbalance present in the network causes additional power loss inside the medium voltage/low voltage transformer and in the transportation line wires too. It also has undesired effects in certain three phase loads, mainly rotating machines where it causes torque reduction and pulsating torque effect. Large scale unbalance can also activate automatic protection functions of electricity dispatch system causes power outage. These negative effects lower the electric power quality and rises the cost of electrical energy and rises the carbon footprint of the everyday life, and also undesirable for the customers and adds maintenance cost to the service provider.

4.2.1 Problem statement

The main idea behind the following results is to apply a direct optimization based compensation method similar to that used in Section 4.1 to the voltage unbalance phenomena present in three-phase electrical networks. For the control aim it is a natural choice to minimize the voltage unbalance of the low voltage local transformer area measured at the connection point of the inverter.

Figure 4.8 depicts the high-level structure of the compensation method.

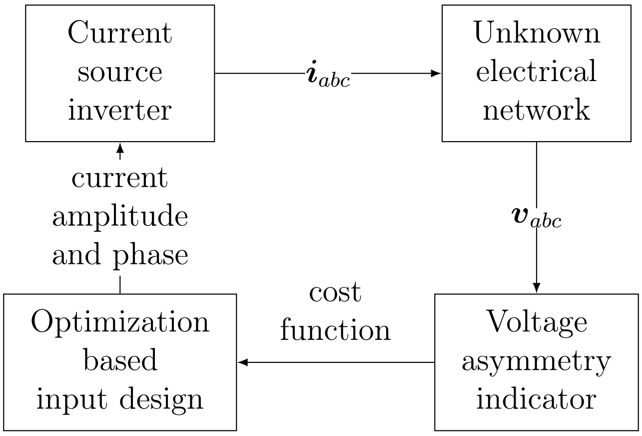

Figure 4.8: High level structure of the unbalance compensation problem

From the control-theoretic point of view, the main characteristics of the problem are as follows.

- Current input to the network (three phase current phasor): $\boldsymbol{i}_{abc} = [i_a, i_b, i_c]$. The current waveform is generated by a three-phase current source inverter, its implementation details are out of the scope of the thesis.

- Measured voltage at the connection point (three phase voltage phasor): $\boldsymbol{v}_{abc} = [v_a, v_b, v_c]$.

- Aim: minimization of the voltage unbalance during the operation of the network. This has to be measured by a suitable norm of voltage unbalance. One possible candidate is VUF (2.5) presented in Section 2.1.2.

Based on the measured quantities, the dynamic behavior of the network cannot be predicted and thus its dynamical model is supposed to be unknown. The only source of information from the network is the voltage response given by the network for the current input. Since the network actors (generators and loads) are continuously switching on and off the network in an unobservable and uncontrollable manner, the model structure as well as the model parameters of the network cannot be determined using the tools of system identification. The above facts makes it difficult to use the model based techniques of control theory.

In the following, the main functional blocks of the problem statement depicted in Figure 4.8 are detailed.

Electrical grid The electrical grid is supposed to be a three-phase grid, the only assumption is that the three-phase voltage $\boldsymbol{v}_{abc}$ can be measured at the connection point. Since the network units (generators and loads) are continuously switching on and off the network in an unobservable and uncontrollable manner, the model structure as well as the model parameters of the network cannot be determined using the tools of system identification. *An important assumption that has to be made with respect to the transient response of the network is that the effect of the input decays by the time the next input is applied to the network.* This cannot be ensured in the general case since the network is unknown.

Unbalance indicator Any suitable norm of voltage unbalance can be used as an unbalance indicator which is a mapping from the three-phase voltage phasor $\boldsymbol{v}_{abc}$ to $\mathbb{R}^+$.

Optimization based input design The optimization based input design is equivalent to the solution of an optimization problem:

$$\min_{\boldsymbol{i}_{abc}} J_U(\boldsymbol{v}_{abc}) \tag{4.5}$$

where J_U stands for the cost function of the optimization problem, i.e. the applied unbalance indicator in this case. Of course, a more sophisticated input design method would take into account the constraints on the applicable current.

Unfortunately, electrical network cannot be described by any deterministic dynamical model according to the assumptions above. Therefore, the optimization methods based on the derivative of the cost function are not applicable. In such cases, the applied optimization method has to be a derivative-free one as the network model is not assumed to be known. A variety of optimization methods are available of this class, e.g. Nelder-Mead [81], Pattern search [47], [60], Simulated annealing [56], Subgradient method [11].

Current source inverter The role of this power electric device is to produce the current waveform according to the phasor $\boldsymbol{i}_{abc}$ determined by the Optimization based input design module, i.e. to play the role of the actuator in this problem. It is important to note, that the inverter is supposed to be an asymmetric three-phase inverter which is able to feed different sinusoidal phase currents to the network. The structure and implementation may depend on the actual field of application and is not in the scope of this thesis. However, a basic model of the unit is presented in Figure A.6 of Section A.3.1.

4.2.2 A novel voltage asymmetry indicator

Section 2.1.2 discussed voltage unbalance of three-phase networks and introduced the most widely used indicator of voltage unbalance (2.5). The problem with VUF is that it does not take into account the zero sequence voltage component v_0. Other unbalance measures not discussed in the present thesis but most of them are neglecting the phase differences of voltage vectors compared to the ideal voltage phasor.

Hence it can be stated that every difference between the ideal and the measured voltage in both amplitude phase and sub-harmonics is caused by a form of voltage deviation from the ideal. The problem can also be investigated from a geometrical point of view as it is depicted in Figure 4.9.

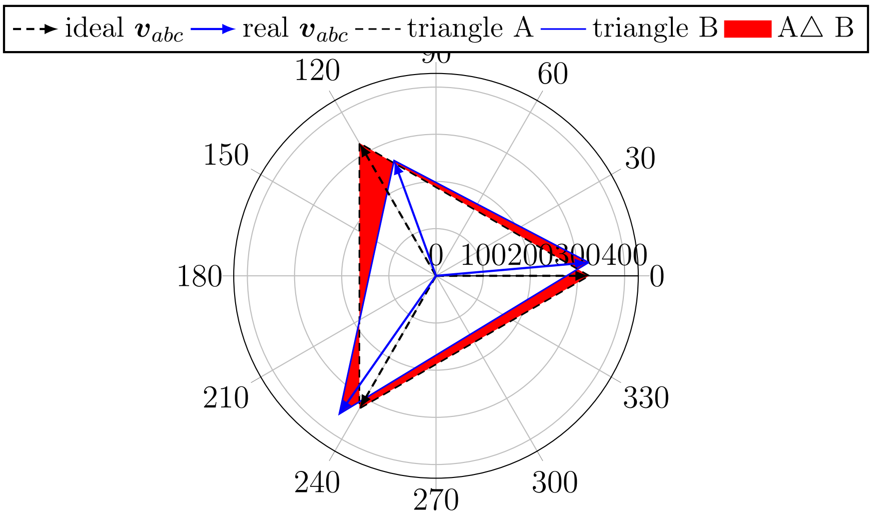

Figure 4.9: The triangles spanned by the ideal and the real peak voltage phasors. The extent of voltage deviation on the network can be measured by symmetric difference of the two triangles.

The three-phase voltage system's phasor diagram contains three phase-to-neutral voltage vectors which can be regarded as the points of a triangle (similarly, the three line-to-line vectors can play the role of the edges of the triangle). The two triangles A and B (i.e. the ideal and the actual ones) always intersect except from very extreme and physically meaningless cases. The area where triangle A and triangle B do not cover each other (i.e. the symmetrical difference of them) can be used as a norm of voltage quality. A indicates the triangle spanned by the ideal voltage vectors and B is the triangle of real voltage vectors. Difference of the ideal and the real triangle's union and intersection defines the norm ε_G. Basically, the algorithm calculates the symmetrical difference of the triangles, spanned by the three phase ideal and real voltage vectors, respectively. This approach fulfills the definition of norm, see e.g [1].

$$\begin{aligned} \varepsilon_G(\boldsymbol{v}_{abc}) &= \mathrm{area}(\mathrm{A} \triangle \mathrm{B}) \\ &= \mathrm{area}(\mathrm{A} \backslash \mathrm{B}) + \mathrm{area}(\mathrm{B} \backslash \mathrm{A}) \\ &= \mathrm{area}(\mathrm{A} \cup \mathrm{B}) - \mathrm{area}(\mathrm{A} \cap \mathrm{B}) \end{aligned} \tag{4.6}$$

In fact it is computationally more demanding compared to the previous methods, but takes every deviation into consideration. A more detailed discussion of the norm (4.6) relative to ε_u is given in [135] and [137].

4.2.3 Detailed voltage unbalance compensation structure

In order to illustrate the applicability of the direct optimization based compensator structure as well as the proposed geometric norm as the cost function a conceptual structure is proposed which is similar to the one used in Section 4.1.2. Because of the simplified nature of the problem, there are some neglected features (e.g. subharmonics, flicker) which might be interesting from the electrical engineering point of view in a real world application, but these features are omitted in this thesis.

As already mentioned the input to the network are current signals $\boldsymbol{i}_{abc}$, which is naturally constrained by the available energy of the household, stored in a battery pack or momentarily generated by the wind or solar generator unit. The response of the system could be either the current or the voltage measured at the connection point of the inverter unit, however, the general legal regulations only allow voltage measurement for consumers.

The goal is to reduce voltage unbalance on the network utilizing the limited resources of a residential solar panel. With this in mind, the device is connected to any three phase four wire 400V connection point, and based on the measured network voltage $\boldsymbol{v}_{abc}$, it generates harmonic current waveforms, that results in unbalance reduction based on the prescribed cost function (ε_u, or ε_G).

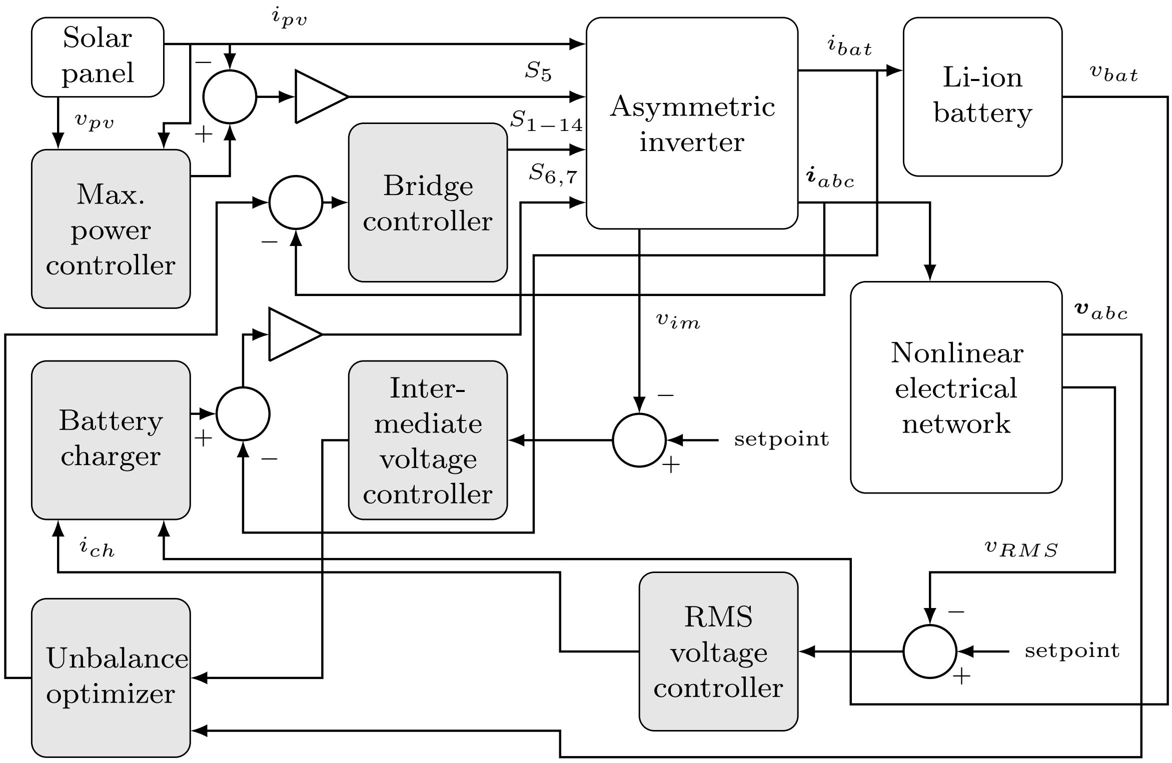

Figure 4.10: Topology of the voltage unbalance compensator. The system also contains a photovoltaic plant as a renewable energy source and a battery. The grayed units are the main functional parts of the system.

The proposed structure can be observed in Figure4.10, which has a similar structure as Figure 4.3 that was used for the distortion compensation before. Some general components are only presented because they are needed for the normal operation of the network, the novel element is the Unbalance optimizer described below.

Asymmetric inverter The current source inverter model applied here is the three-phase asymmetric extension of the inverter model used in Section 4.1.2, Figure 4.2. The power electrical details of the inverter implementation is out of the scope of this thesis. A possible implementation of the inverter in Figure A.6.

Maximum power controller It has the same role and properties as in Section 4.1.2.

Battery charger It has the same role and properties as in Section 4.1.2.

RMS voltage controller It has the same role and properties as in Section 4.1.2.

Intermediate voltage controller It has the same role and properties as in Section 4.1.2.

Bridge controller It has the same role and properties as in Section 4.1.2, however, its implementation is different because of the asymmetric three phase inverter to be controlled.

Unbalance optimizer The unbalance optimizer is the fundamental element of the proposed compensation structure , it corresponds to the Optimization based input design block of the general structure of Figure 4.8. Its input is the three-phase voltage waveform corresponding to the phasor $\boldsymbol{v}_{abc}$ measured at the network connection point. The output of the unit is a three-phase sinusoidal output current waveform that has to be implemented by the Asymmetric inverter and the Bridge controller. From the optimization point of view the optimization space is the six dimensional space of magnitude and phase values of the output current phases i_a, i_b and i_c, respectively.

Nonlinear electrical network The network, the proposed voltage unbalance compensator supposed to be connect, is a three phase four wire low voltage domestic transformer area. For the sake of modeling and simulation simplicity, the transformer's secondary circuit is assumed to be in star connection, where the neutral wire is grounded, and modeled as ideal voltage sources connected to a three phase function generator or a specific input waveform in case of measurements. It is worth mentioning, that the transformer choice could convey some issues as indicated by [110], and [98], but the transformer modeling is out of scope of this thesis.

4.2.4 Voltage unbalance compensation as an optimization problem

The Unbalance optimizer block of Figure 4.10 determines the six waveform parameters $(|i_a|, |i_b|, |i_c|, \angle i_a, \angle i_b, \angle i_c)$ of the three-phase sinusoidal current output $\boldsymbol{i}_{out}$ of the system implemented by the inverter.

$$i_k(t) = |i_k| \sin(\omega t + \angle i_k), \quad k \in \{a, b, c\} \tag{4.7}$$

The optimization problem is (4.8).

$$\min_{\boldsymbol{i}_{abc}} J_U(\boldsymbol{v}_{abc}) = \min_{\boldsymbol{i}_{abc}} \varepsilon_G(\boldsymbol{v}_{abc}) \tag{4.8}$$

Of course, any other unbalance norm (e.g. ε_u) can be selected as the cost function of the problem. Since the cost function is implicitly contains the unknown network, it is impossible to use classical optimization methods rely on the derivative of J_U. As it was mentioned in Section 4.2.1, there are several derivative-free optimization methods available in the literature for solving problems like 4.5. For such problems, pattern search methods are one possible solution technique since they neither require nor explicitly estimate derivatives. In [135], the asynchronous parallel pattern search (APPS) method is used for the solution of (4.8). The methodology and formulation of the APPS method is described in more detail in Section 2.3.2.

The basis of the applied optimizer algorithm is Algorithm 4 used in Section 4.1.3 for THD compensation. The main difference is in the dimension of the search space of the method. While in the case of Algorithm 4, refining the method to additional higher order voltage and current harmonics would increase the search space dimension by two (magnitude and phase of the additional current harmonics) in the case of the optimizer (Algorithm 5) used for the problem (4.8) works in a six dimensional search space. Basically the general strategy for the APPS method, from a single process perspective is given in Algorithm 5.

Similarly to Section 4.1.3 let us define the mapping (4.9) from the search space of the optimization problem (i.e. the three-phase current magnitudes and phases $\boldsymbol{x} = [|i_a|, |i_b|, |i_c|, \angle i_a, \angle i_b, \angle i_c]^T \in \mathbb{R}^6$) to the measured voltage $\boldsymbol{v}_{abc}$ at the network connection point. In other words, f_{net} represents the inverter with the bridge controller and also the unbalanced electrical network.

$$\boldsymbol{v}_{abc} = f_{net}(\boldsymbol{x}) \tag{4.9}$$

Of course, the actual form of the mapping (4.9) is unknown.

Algorithm 5 Optimization algorithm for voltage unbalance compensation

procedure APPS-VU
    $\boldsymbol{x}_j(0) = \mathbf{0}$, $\Delta_j(0) = 0, d_j(0) = 1$
    while $J_U(f_{net}(\boldsymbol{x}_j(q) + \Delta_j(q)d_j(q)) \neq 0$ **do**
        for j=1:6 **do**
            $d_j(q) = 0.5(\mathrm{sign}(N(q-3) - N(q-2) + \mathrm{sign}(N(q-4) - N(q-3))))$
            $\Delta_j(q) = n_j N(q-1)\Delta_j(q-1) + \Delta_j(q-2) + m_j N(q-1)$
            $N(q) = J_U(f_{net}(\boldsymbol{x}_j(q) + \Delta_j(q)d_j(q)))$
            if $J_U(f_{net}(\boldsymbol{x}_j(q) + \Delta_j(q)d_j(q))) < J_U(f_{net}(\boldsymbol{x}_j(q)))$ **then**
                $\boldsymbol{x}_j(q+1) = \boldsymbol{x}_j(q) + \Delta_j(q)d_j(q)$
            end if
        end for
        q++;
    end while
end procedure

Δ_i the process step length i.e. the value of the current vector's amplitude or angle needs to be changed for a successful step, and d_i is the corresponding step's signed direction vector, which specifies the applied changes direction. Furthermore N represents the chosen norm's value as the network's response to the current injection, and n_i, and m_i are scaler gains for the corresponding process. The initial values of $\boldsymbol{x}_i(0) = 0$, $\Delta_i(0) = 0$, due to lack of prior network knowledge and to avoid large initial transients.

In the case of the proposed algorithm, an individual pattern vector (see Section 2.3.2) is defined for each output variable, and the optimization was performed in each direction asynchronously and shifted in time. Approaching the minimal value of norm, the controller uses adaptive increments that are proportional to the norm itself. Because of the complex interactions between the components of the controller, only one parameter is changed at a time, even if the values of the amplitude and phase components in specific time slot changes. The algorithm moves along the six axes of six separate time slots close to the local minimum of the error function, however the first step of the six is trivial, since it can be locked to the first phase .

The advantage of this compensator structure that is not necessary to know the controlled systems' behavior, as the number and type of the other loads on the network is unknown [135]. There are however three disadvantages. First is the low speed of control, due to the several necessary iterations (depending on the circumstances) to find the optimal directions in the parameter space, and the serial nature of interventions and norm calculations. The second comes from the method itself since the optimizer may stuck in local minima, and the third is that the sequential current injections may increase THD of the network.

4.2.5 Simulation based analysis

Unfortunately, the method cannot be examined on a real network connected to the grid, that is why a high fidelity simulation model had been developed for the experimental study. In order to be able to investigate the proposed optimization based unbalance reduction with the three phase inverter on a low voltage local grid, all the elements of this complex electrical system (including the photovoltaic source, battery, and other power electronic components) has been modeled in Matlab/Simulink environment according to [135]. The top level structure of the Simulink model can be seen in Figure A.7 in Section A.3. The domains of the signals expected are as follows:

- Controller output (three phase current phasor): $\boldsymbol{i}_{abc} = [i_a, i_b, i_c]$, the domain for each phase is [0, 20] A amplitude and $\pm 60°$ phase.

- Measured signal (three phase voltage phasor): $\boldsymbol{v}_{abc} = [v_a, v_b, v_c]$, the domain for each phase is [0, 326] V (peak) amplitude and $\pm 60°$ phase.

It is important to note, that the following case study serves as a proof of concept and a simulation based benchmark problem in order to be able to compare different unbalance indicators as well as different optimization problems.

In order to investigate the operation of the proposed method as well as the symmetric difference based unbalance norm ε_G, several different simulation experiments have been performed using the dynamical simulation model. The results of the first experiment is presented in Figure 4.11, where the operation of the APPS-based optimizer can be seen. Note, that the fundamental concept behind Algorithm 5 and Algorithm 4 is the same, as it can be seen in Figures 4.11 and Figure 4.5.

The aim of performance analysis is twofold. First of all, the proposed voltage unbalance indicator has to be investigated in the control structure as the cost function of the optimization based controller, and on the other hand, the control structure itself has to be exposed against engineering expectations on a proof of concept level.

The results of the second set of experiments can be seen in the top of Figure 4.12 where ε_G has been used as the voltage unbalance indicator and the cost function for the optimizer on an experimental network with fixed unbalanced load. The dashed line represents the examined low voltage local network's voltage unbalance norm (G) without the proposed controller implemented in the inverter unit of the domestic powerplant while the solid line represents the compensated network's value. Note, that the geometrical norm is a unit-less value, since it represents the ideal and the real voltage phasor's symmetric difference.

Measurements from a real unbalanced network

In order to expose the method to more realistic circumstances, the simulation model was set up in such a way, that measurement data from a real network with voltage unbalance The measurements took place at the campus building's power electronics

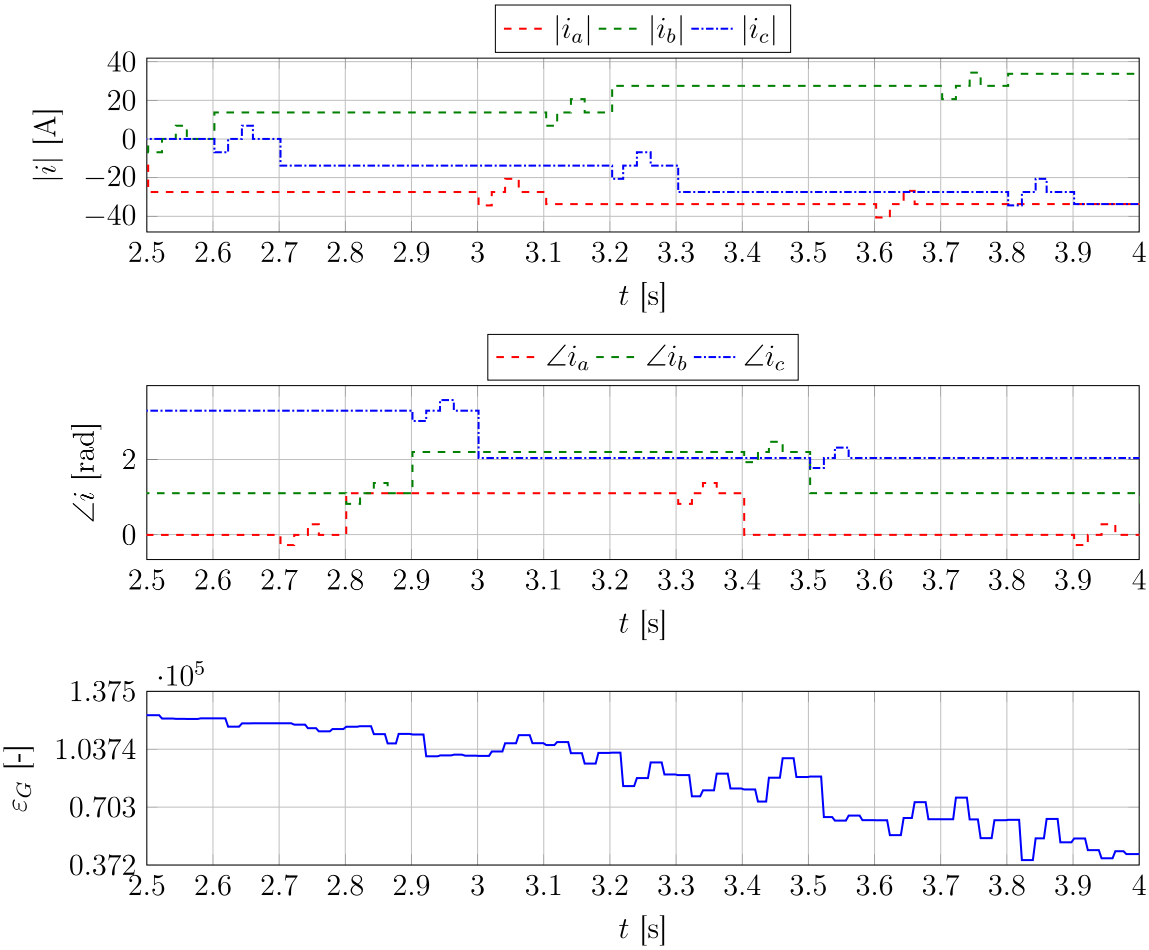

Figure 4.11: Operation of the optimal unbalance compensation. It can be observed that each optimization sequence has it's delayed time window in strict order of 0.1 second. In each step an upper and a lower directional test step is made with the with of 0.02 second from which the algorithm can decide the size and direction of the next step, based on Algorithm 5. As such 0.6 second is required for performing one optimization cycle.

laboratory, where a common 400 V connection point was investigated as the behaviour of the network.

Afterwards, the measurement data has been used as the input of a micro-grid segment of the Matlab/Simulink model in order to test the controller and inverters structure's performance in quasi-realistic circumstances. Figure 4.12 shows the simulation results with respect to ε_G and ε_u. It can be seen, that the optimal compensation that uses ε_G as cost function decreases VUF as well. The compensators performance on the simulated microgrid's network loss reduction can be observed by means of active and reactive power loss in the bottom two plots of Figure 4.12. It can be concluded that the reactive power loss cannot be decreased with the proposed structure and method.

The measurement output is connected to a modeled three phase load and network system, consisting of symmetrical loads and network segments between them. Further artificial load unbalance is not necessary since the network's unbalance is already present. This structure enables to show that any point the inverter is connected,

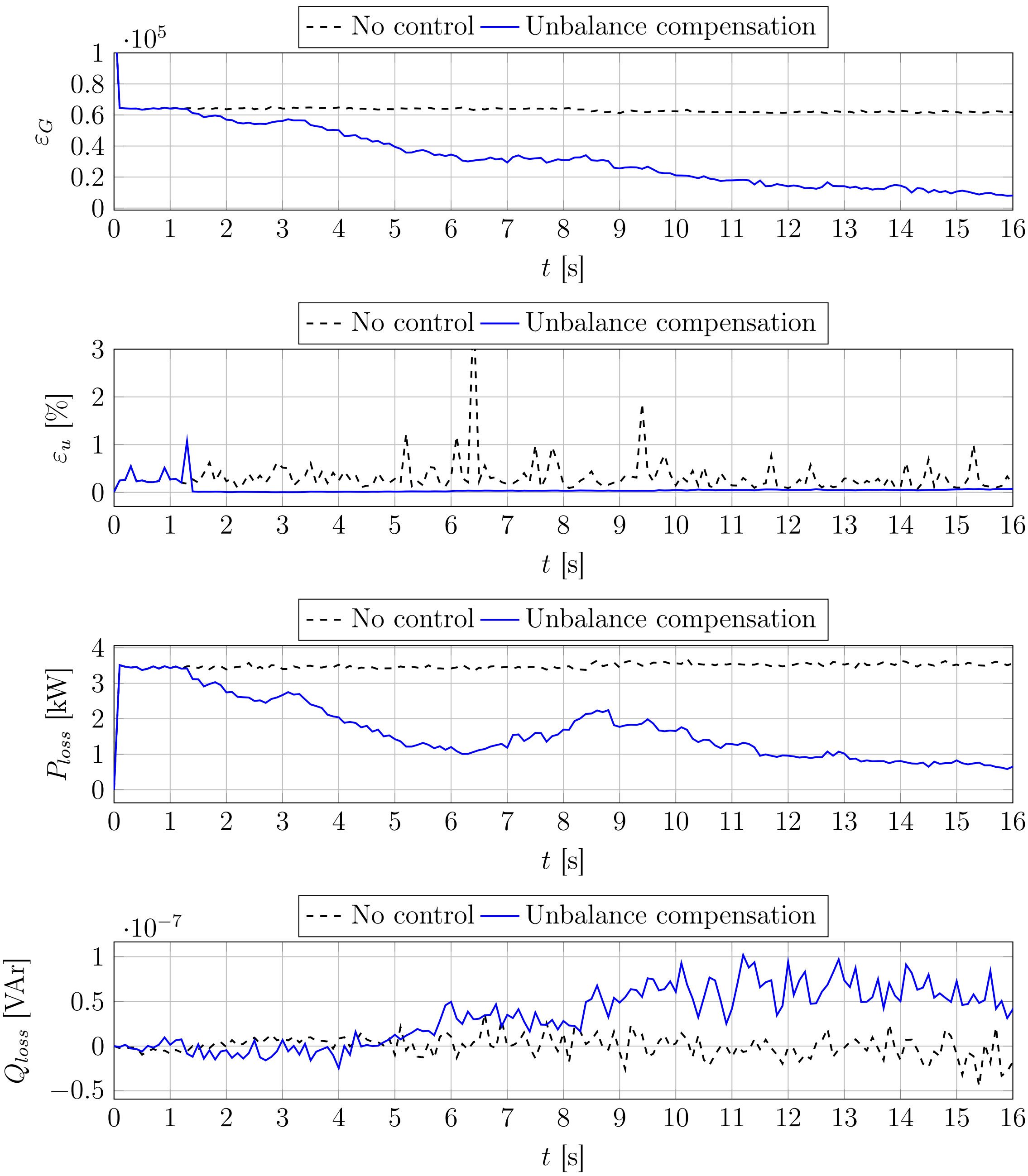

Figure 4.12: Unbalance compensation system performance with a half charged battery and photovoltaic power source available on a measurement driven network. The optimization based compensation starts at $t = 1s$. Top: The underlying unbalance norm is the geometrical one (ε_G). Second: ε_u is also smoothed due to the compensation. Third: The active power loss (P_{loss}) is actively decreasing due to the result of unbalance compensation, Bottom: The reactive power loss (Q_{loss}) cannot be decreased by the unbalance compensation.

could restore power quality with a certain degree such unbalance compensation at this case. The future plan is to set up multiple devices on different connection points.

Performance comparison of different unbalance indicators

In this section the chosen unbalance indicators, ε_u, and ε_G will be compared in performance solving the same optimization problem. The only difference between the three compared simulations are the Algorithm 5's cost function candidate (ε_u, or ε_G), as they are compared to the uncompensated reference simulation experiment. The environment consist of a notable voltage unbalance and an emphasized undervoltage, so the difference of the two approaches would be observable.

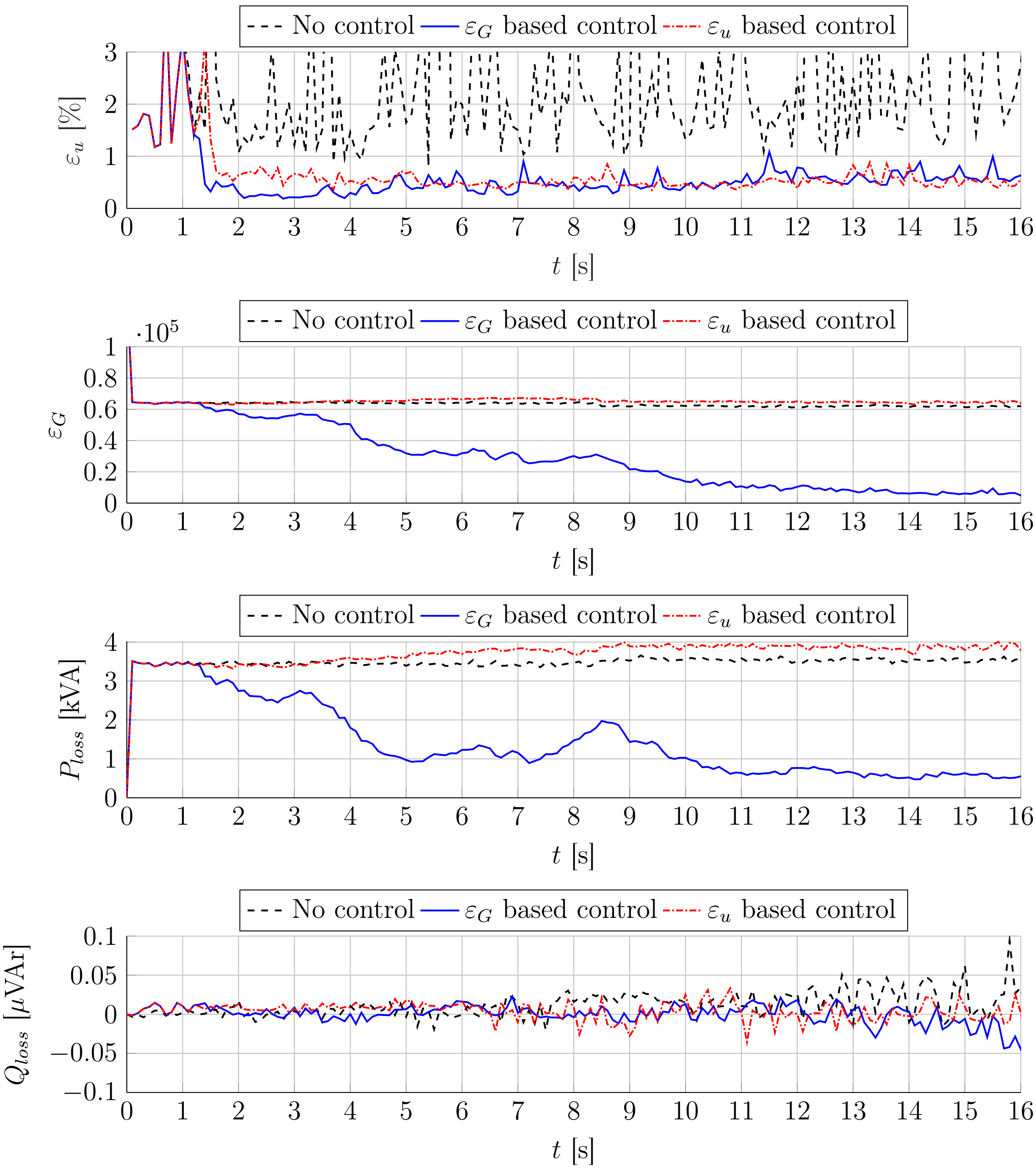

Figure 4.13: Voltage unbalance compensation when employing VUF or the geometric norm as cost function. Together with the network's active (P_{loss}) and reactive losses Q_{loss} in case of ε_u or ε_G as cost function. The controller starts at $t = 1s$.

It can be observed, that in Figure 4.13 the value of ε_u does not deviate much in case of different cost function options. However, observing the trend of ε_G with the same circumstances, the values are showing a different trend with in case of the ε_u based approach, the unbalance is slightly above the uncontrolled threshold, and with ε_G a clear reduction is shown. This is due to the case of the initial large undervoltage, which gets compensated, but with ε_u it is not recognised.

In terms of network power losses with the previous example observable in Figure 4.13. In case of the active power losses the simulation with ε_G as cost candidate produces clear reduction, but with the ε_u a slight increase. However with all approaches the reactive power slowly diverges form zero over time, which is a clear improvement point for the future.

4.3 Summary

Two different power quality problems has been formulated as model-free optimization problems. In both cases, a conceptual problem statement was given for the solution without any deep power electronics details as the main focus of the present thesis is the formulation of different energy related problems as optimization problems.

A compensator structure has been proposed in Section 4.1 enabling the integration of small domestic powerplants that use renewable sources of energy supply to the low voltage power grid with significant improvement of power quality by means of the total harmonic distortion. The key element of the structure is an optimizer that minimizes a cost function related to the total harmonic distortion in the higher order current harmonics magnitude and phase solution space.

A direct optimization based compensation structure applicable for three-phase network is proposed in Section 4.2 of the chapter. Due to the basic assumptions regarding the network, the optimal input current phasor can be found by any derivative-free optimization method. The cost function for the proposed voltage unbalance optimizer can be any scalar valued VU norm, however, the geometrical unbalance norm is applied as a cost function in the asymmetry reducing optimization based control utilizing an asynchronous parallel pattern search (APPS) algorithm. Simulations, performed in Matlab/Simulink environment show that the geometrical based indicator can serve as a basis of further research. The optimization-based control algorithm injects the available energy (as current waveform) in such a way, that the voltage unbalance decreases.

Chapter 5

Optimization based analysis and control of smooth nonlinear systems using quasi-polynomial and Lotka-Volterra representation

Global asymptotic stability is a very strong property of all system classes. Although global asymptotic stability is an easy to check property of linear time-invariant systems the global stability analysis of general nonlinear systems is far from being trivial, and results can be obtained only for special system classes.

On the other hand, electrical energy related dynamical systems are frequently nonlinear in nature which makes it important to use general nonlinear descriptive models such as the quasi-polynomial system class.

The fundamental works on LV systems was proposed by Lotka [69] and Volterra [109] which put the LV form into a population biology framework.

From the $90's$ there are several works about the representation of general nonlinear systems having smooth nonlinearities by QP and LV models, e.g. [42], [43] [44]. [43] established the algebraic structure of the class of QP systems. They split into equivalence classes and each class of equivalence is represented by a Lotka-Volterra system.

The other branch of papers are engaged in the stability properties of Lotka-Volterra and quasi-polynomial systems. Local stability analysis of them can be found in [23], where the locally linearized system matrices can be determined directly from the QP or LV system's parameter matrices. Several works investigate the global stability of Lotka-Volterra predator-prey models, especially with periodic solutions [100], [70]. However, there are also works on the global stability of quasi-polynomial systems [41], [28]. The main weakness of them is that only small (3-4) dimensional LV systems can be handled with these methods. An interesting numerical method for their stability analysis is given in [33].

On the other hand, the utilization of Lotka-Volterra models for feedback control appears only in few papers [35], or [36], where the positive stabilizing control is proposed only for a subset of LV systems.

Based on the fundamental concepts of QP and LV systems presented in Section 2.2, this chapter draws up own results that connects the global stability analysis of quasi-polynomial systems with a class of optimization problems. Section 5.1.1 presents a method for global stability analysis.

Embedding the energy system into QP form (see Section 2.2.3), and applying state feedback that preserves the QP-form of the closed loop system, its global stability can be conveniently investigated by using linear matrix inequalities if the feedback parameters are known and fixed. If the feedback parameters are not fixed, then an optimization based feedback design problem is defined that globally stabilizes the closed loop system, that is the subject of Section 5.2.1.

5.1 Optimization based global stability analysis of smooth nonlinear systems

The dissipativity condition of a class of Lyapunov functions for Lotka-Volterra systems can be reformulated so that Laypunov function based stability analysis methods can be performed using widespread numerical solvers.

5.1.1 Global stability analysis as a linear matrix inequality

In what follows, $\boldsymbol{x}^*$ will denote an element-wise positive equilibrium state of the quasi-polynomial dynamics (2.11), i.e. $\boldsymbol{x}^* \in \mathrm{int}(\mathbb{R}^n_+)$ Similarly $\boldsymbol{z}^* \in \mathrm{int}(\mathbb{R}^m_+)$ is a positive equilibrium point in the Lotka-Volterra system (2.12). What makes the Lotka-Volterra system class for a good candidate for stability analysis [41] is the fact that there exists a well known entropy-like Lyapunov function family for them ,[28], which is in the form (5.1)

$$V(\boldsymbol{z}) = \sum_{i=1}^{m} c_i \left(z_i - z_i^* - z_i^* \ln \frac{z_i}{z_i^*} \right), \qquad (5.1)$$
$$c_i > 0, \quad i = 1 \ldots m,$$

where $\boldsymbol{z}^* = (z_1^*, \ldots, z_m^*)^T$ is the equilibrium point of the Lotka Volterra model (2.12).

It is examined and proved in [28] and [41] that the global stability of (2.12) with Lyapunov function (5.1) implies the boundedness of solutions and global stability of the original QP system (2.11). That is, the Lotka-Volterra model is dynamically equivalent to the QP models for which the product $\boldsymbol{M} = \boldsymbol{B}\,\boldsymbol{A}$ is invariant. Practically, the Lotka-Volterra variables are the quasi-monomials (2.13) of such QP systems, so the Lyapunov function (5.1) can also be used in the quasi-polynomial coordinates.

The time derivative of the of the Lyapunov function (5.1) is:

$$\dot{V}(\boldsymbol{z}) = \frac{1}{2}(\boldsymbol{z} - \boldsymbol{z}^*)(\boldsymbol{C}\,\boldsymbol{M} + \boldsymbol{M}^T\boldsymbol{C})(\boldsymbol{z} - \boldsymbol{z}^*) \qquad (5.2)$$

where $\boldsymbol{C} = \mathrm{diag}(c_1, \ldots, c_m)$ is a diagonal matrix of the Lyapunov function parameters and $\boldsymbol{M}$ is the invariant matrix characterizing the LV form (2.12). The non-increasing nature of the Lyapunov function (5.1) is equivalent to a feasibility problem over the following set of *linear matrix inequality* (LMI) constraints:

$$\begin{array}{rcl} \boldsymbol{C}\,\boldsymbol{M} + \boldsymbol{M}^T\boldsymbol{C} & \leq & \boldsymbol{0} \\ \boldsymbol{C} & > & \boldsymbol{0} \end{array} \qquad (5.3)$$

where the unknown matrix is $\boldsymbol{C}$, which is diagonal and contains the coefficients of (5.1). (See Appendix 2.3.3 for the properties and solution methods of LMIs.)

The similarity of the stability conditions is apparent with that of continuous time linear time-invariant systems. If a linear time-invariant system with state matrix $\boldsymbol{A}$

is asymptotically stable, there must be positive definite matrices $\boldsymbol{P}$ and $\boldsymbol{Q}$ such that $\boldsymbol{A}^T\boldsymbol{P}+\boldsymbol{P}\,\boldsymbol{A}=-\boldsymbol{Q}$ (the *Lyapunov-equation*). The linear system and $\boldsymbol{A}$ is diagonnally stable if $\boldsymbol{P}$ is a diagonal matrix [53].

It is important to mention that the strict positivity constraint on c_i can be somewhat relaxed in the following way [28]: if the equations of the model (2.11) are ordered in such a way that the first n rows of $\boldsymbol{B}$ are linearly independent, then $c_i > 0$ for $i = 1, \ldots, n$ and $c_j = 0$ for $j = n+1, \ldots, m$ still guarantee global stability.

It is stressed that *global stability is restricted to the positive orthant int*($\mathbb{R}^n_+$) *only for QP and LV models*, because it is their original domain (see the definition in (2.11)).

It is also important that the global stability of the equilibrium points of (2.11) with Lyapunov function (5.1) does not depend on the value of the vector $\boldsymbol{L}$ as long as the equilibrium points are in the positive orthant [28]. This fact will allow us to place the equilibrium point of the closed loop system during the stabilizing controller design (see Section 5.2).

The possibilities to find a Lyapunov function that proves the global asymptotic stability of a QP system can be increased by using time-reparametrization [144].

The computationally effective method of global stability analysis for Lotka-Volterra and QP systems can be used for the global stability analysis of general smooth nonlinear systems because of the descriptive nature of the QP model class. According to Section 2.2.3, general nonlinear dynamical systems with smooth nonlinearities can be embed into the ODE form (2.11). Of course the fact that the embedding introduced hidden algebraic equations (see Section A.4 for an illustrative example) to the model has to be taken into consideration.

5.2 Globally stabilizing feedback design

As a next step, the promising properties of the QP and LV system classes can be used for stabilizing controller synthesis for general smooth nonlinear systems. In order to control a QP (and consequently a LV) model a non autonomous version of the ODEs (2.11) and (2.12) is needed. The input-affine extension (2.14)-(2.15) of the models are used here and the fact is used that the class of quasi-polynomial systems is closed under quasi-polynomial state feedback laws.

5.2.1 The controller design problem

The globally stabilizing QP state feedback design problem for QP systems can be formulated as follows [132]. Consider arbitrary quasi-polynomial inputs in the form:

$$u_l = \sum_{i=1}^{r} k_{il}\,\hat{q}_i(\boldsymbol{x}), \quad l = 1\ldots, p \tag{5.4}$$

where $\hat{q}_i(\boldsymbol{x}) = \hat{q}_i(x_1, \ldots, x_n),\ i = 1, ..., r$ are arbitrary quasi-monomial functions of the state variables of (2.14) and k_{il} is the constant gain of the quasi-monomial function $\hat{q}_i$ in the l-th input u_l. The closed loop (autonomous) system will also be a QP system with matrices

$$\hat{\boldsymbol{A}} = \boldsymbol{A}_0 + \sum_{l=1}^{p}\sum_{i=1}^{r} k_{il}\boldsymbol{A}_{il}, \quad \hat{\boldsymbol{B}}, \tag{5.5}$$

$$\hat{\boldsymbol{\lambda}} = \boldsymbol{\lambda}_0 + \sum_{l=1}^{p}\sum_{i=1}^{r} k_{il}\boldsymbol{\lambda}_{il}. \tag{5.6}$$

Note that the number of quasi-monomials in the closed-loop system (i.e. the dimension of the matrices) together with the matrix $\hat{\boldsymbol{B}}$ may significantly change depending on the choice of the feedback structure, i.e. on the quasi-monomial functions $\hat{q}_i(\boldsymbol{x})$.

Furthermore, the closed loop Lotka-Volterra coefficient matrix $\hat{\boldsymbol{M}}$ can also be expressed in the form:

$$\hat{\boldsymbol{M}} = \hat{\boldsymbol{B}}\,\hat{\boldsymbol{A}} = \boldsymbol{M}_0 + \sum_{l=1}^{p}\sum_{i=1}^{r} k_{il}\boldsymbol{M}_{il}.$$

Then the global stability analysis LMI (5.3) of the closed loop system with unknown feedback gains k_{il} leads to the following bilinear matrix inequality (5.7) (see Section 2.3.3 for the general form (2.28) and solution methods for bilinear matrix inequalities).

$$\hat{\boldsymbol{M}}^T\boldsymbol{C} + \boldsymbol{C}\,\hat{\boldsymbol{M}} = \boldsymbol{M}_0^T\boldsymbol{C} + \boldsymbol{C}\,\boldsymbol{M}_0 + \sum_{l=1}^{p}\sum_{i=1}^{r} k_{il}\left(\boldsymbol{M}_{il}^T\boldsymbol{C} + \boldsymbol{C}\,\boldsymbol{M}_{il}\right) \leq \boldsymbol{0}. \tag{5.7}$$

The variables of the BMI are the $p \times r$ k_{il} feedback gain parameters and the $c_j,\ j = 1,..,m$ parameters of the Lyapunov function (5.1). If the bilinear matrix inequality (5.7) is feasible then there exists a globally stabilizing feedback with the selected structure.

It is important to note, that the fact that a QP system is obtained by embedding a general nonlinear system into QP form usually makes the solution of (5.7) more difficult as the rank of matrix $\boldsymbol{M}$ is not full in such cases.

5.2.2 Numerical solution of the controller design problem

This section deals with the numerical aspects of the globally stabilizing controller design problem.[133]

5.2.3 Numerical solution based on bilinear matrix inequalities

There are just few software tools available for solving general bilinear matrix inequalities that is a computationally hard problem. In some rare fortunate cases with a suitable change of variables quadratic matrix inequalities can be rewritten as linear matrix inequalities (see e.g. [10]). Unfortunately, the structure of the matrix variable of (5.7) does not fall into this fortunate problem class, so the previously mentioned idea cannot be used.

Rewriting the above matrix inequality (5.7) in the form (2.28) one gets the following expression which can be directly solved by [58] as a BMI feasibility problem:

$$\begin{aligned} \sum_{j=1}^{m} c_j\bar{M}_{0j} + \sum_{j=1}^{m}\sum_{l=1}^{p}\sum_{i=1}^{r} c_j k_{il}\bar{M}_{(il)j} &\leq 0 \\ -c_1 &< 0 \\ &\vdots \\ -c_m &< 0. \end{aligned} \tag{5.8}$$

The two disjoint sets of BMI variables are the c_j parameters of the Lyapunov function (5.1) and the k_{il} feedback parameters. The parameters of the problem $\bar{M}_{0j}$ ($\bar{M}_{(il)j}$, respectively) are the symmetric matrices obtained from $\boldsymbol{M}_0$ ($\boldsymbol{M}_{il}$, respectively) by adding the $m \times m$ matrix that contains only the j-th column of $\boldsymbol{M}_0$ ($\boldsymbol{M}_{il}$, respectively) to its transpose:

$$\boldsymbol{M} = \begin{bmatrix} m_{11} & \cdots & m_{1j} & \cdots & m_{1m} \\ \vdots & \ddots & \vdots & \ddots & \vdots \\ m_{m1} & \cdots & m_{mj} & \cdots & m_{mm} \end{bmatrix}$$

$$\downarrow$$

$$\bar{\boldsymbol{M}}_j = \begin{bmatrix} 0 & \cdots & m_{1j} & \cdots & 0 \\ \vdots & & \vdots & & \vdots \\ m_{1j} & \cdots & 2m_{jj} & \cdots & m_{mj} \\ \vdots & & \vdots & & \vdots \\ 0 & \cdots & m_{mj} & \cdots & 0 \end{bmatrix}.$$

Note that for low dimensions (i.e. for $m < 3$) there are practically feasible methods for circumventing the BMI feasibility problem [53] but these cannot be extended to the practically important higher dimensional case.

An iterative LMI approach to controller design problem Because of the NP-hard nature of the general BMI solution problem, it is worthwhile to search for an approximate but numerically efficient alternative way of solution. As shown below, the special structure of the QP stabilizing feedback design BMI feasibility problem allows the application of a computationally feasible method for its solution that solves an LMI in each of its iterative approximation step. The already existing iterative LMI (ILMI) algorithm of [16] used for static output feedback stabilization (see e.g. in [39]) will be used for this purpose.

In order to be able to use the ILMI algorithm, it is necessary to write up the QP stabilizing feedback design problem as a static output feedback stabilization problem for LTI systems. In what follows the globally stabilizing feedback design BMI (5.7) is used in the form

$$(\boldsymbol{M}_0 + \boldsymbol{\Theta}\, \boldsymbol{K})^T \boldsymbol{C} + \boldsymbol{C}(\boldsymbol{M}_0 + \boldsymbol{\Theta}\, \boldsymbol{K}) < \boldsymbol{0}. \tag{5.9}$$

where $\boldsymbol{\Theta}$ and $\boldsymbol{K}$ are the matrices defined in (5.10) and (5.11), respectively.

$$\boldsymbol{\Theta} = \left[\overbrace{\boldsymbol{M}_1, \ldots, \boldsymbol{M}_p}^{1^{\text{st}}}, \ldots, \overbrace{\boldsymbol{M}_1, \ldots, \boldsymbol{M}_p}^{r^{\text{th}}} \right], \tag{5.10}$$

$$\boldsymbol{K} = \begin{bmatrix} k_{11}\, \boldsymbol{I}_{m\times m} \\ \vdots \\ k_{1p}\, \boldsymbol{I}_{m\times m} \\ \vdots \\ k_{r1}\, \boldsymbol{I}_{m\times m} \\ \vdots \\ k_{rp}\, \boldsymbol{I}_{m\times m} \end{bmatrix} \tag{5.11}$$

The above problem is equivalent to a LTI output feedback stabilization problem (5.12) below.

$$(\boldsymbol{A} + \boldsymbol{B}\, \boldsymbol{F}\, \boldsymbol{C})^T \boldsymbol{P} + \boldsymbol{P}(\boldsymbol{A} + \boldsymbol{B}\, \boldsymbol{F}\, \boldsymbol{C}) < \boldsymbol{0} \tag{5.12}$$

Matrix $\boldsymbol{M}_0$ corresponding to the state matrix $\boldsymbol{A}$, $\boldsymbol{\Theta}$ playing the role of the input matrix $\boldsymbol{B}$, and $\boldsymbol{K}$ serving as $\boldsymbol{F}\,\boldsymbol{C}$ and $\boldsymbol{P}$ is the unknown matrix variable of the problem.

It is apparent that the matrix parameters and variables have a special structure for quasi-polynomial systems.

The ILMI algorithm does not aim at finding the complete feasible set of the BMI (5.9) but computes an optimal solution point with minimal trace of $\boldsymbol{C}$ if the BMI is feasible. The ILMI algorithm solves a linear objective function minimizing LMI and a generalized eigenvalue problem in each step. The scheme of the algorithm adapted for QP stabilizing state feedback design is given in Algorithm 6.

Algorithm 6 Iterative LMI algorithm for stabilizing state feedback designĹą

Require: $\boldsymbol{Q} > \boldsymbol{0}$

Solve $\boldsymbol{M}_0^T\boldsymbol{C} + \boldsymbol{C}\boldsymbol{M}_0 - \boldsymbol{C}\Theta\Theta^T\boldsymbol{C} + \boldsymbol{Q} = \boldsymbol{0}$ for $\boldsymbol{C}$
$i \leftarrow 1$
$\boldsymbol{X}_1 \leftarrow \boldsymbol{C}$
loop
    Minimize α_i subject to the LMI constraints

$$\begin{bmatrix} M_0^T C_i + C_i M_0 - X_i\Theta\Theta^T C_i - C_i\Theta\Theta^T X_i + X_i\Theta\Theta^T X_i - \alpha_i C_i & (\Theta^T C_i + K)^T \\ \Theta^T C_i + K & -I \end{bmatrix} < 0,$$

$$\boldsymbol{C}_i = \mathrm{diag}(c_{i1}, \ldots, c_{im}) > 0$$

    if $\alpha_i^* \leq 0$ **then**
        return $\boldsymbol{K}$ ▷ $\boldsymbol{K}$ is a stabilizing gain
    end if
    $\alpha_i \leftarrow \alpha_i^*$
    Minimize trace($\boldsymbol{C}_i$) subject to the LMI constraints

$$\begin{bmatrix} M_0^T C_i + C_i M_0 - X_i\Theta\Theta^T C_i - C_i\Theta\Theta^T X_i + X_i\Theta\Theta^T X_i - \alpha_i C_i & (\Theta^T C_i + K)^T \\ \Theta^T C_i + K & -I \end{bmatrix} < 0,$$

$$\boldsymbol{C}_i = \mathrm{diag}(c_{i1}, \ldots, c_{im}) > 0$$

    if $\|\boldsymbol{X}_i - \boldsymbol{C}_i^*\| < \delta$ **then**
        return false ▷ The system cannot be stabilized
    else
        $i \leftarrow i + 1$
        $\boldsymbol{X}_i \leftarrow \boldsymbol{C}_i^*$
    end if
end loop

It is important to note that for QP systems with rank deficient $\boldsymbol{M}_0 = \boldsymbol{B}\,\boldsymbol{A}$ some additional techniques are needed because the algorithm fails for singular $\boldsymbol{M}_0$ matrices. One possible way is using singular perturbation on $\boldsymbol{M}_0$:

$$\tilde{\boldsymbol{M}}_0 = \boldsymbol{M}_0 - \gamma\,\boldsymbol{I}_{m\times m}, \qquad \gamma > 0.$$

If this way $(\tilde{\boldsymbol{M}}_0, \boldsymbol{\Theta})$ become stabilizable then Algorithm 6 can be applied.

According to [16] the algorithm is convergent although sometimes it may not achieve a solution because α not always converges to its minimum. The proper selection of initial Q affects the convergence of the algorithm, a suitable selection of Q that guarantees the immediate convergence can be found in [16]. Based on the above, the algorithm is used as an off-the-shelf tool, that's why no numerical analysis is presented here.

It is important to emphasize here, that the computationally feasible ILMI algorithm can be used to test the feasibility of the associated BMI, and then the final design can be performed by a constrained optimization method using a suitable controller performance criterion in the feasible case.

5.2.4 Equilibrium points

After solving the globally stabilizing feedback design BMI the resulting Lotka-Volterra system has a globally asymptotically stable equilibrium point in the positive orthant. This steady-state equilibrium point $\boldsymbol{x}^*$ can be determined from the steady-state version of the closed loop quasi-polynomial system (2.11)

$$0 = x_i \left(\hat{\lambda}_i + \sum_{j=1}^{m} \hat{A}_{ij} \prod_{k=1}^{n} x_k^{\hat{B}_{jk}} \right), \quad i = 1, \ldots, n. \tag{5.13}$$

By excluding the non strictly positive equilibrium states one only has to deal with the equation:

$$0 = \hat{\lambda}_i + \sum_{j=1}^{m} \hat{A}_{ij} \prod_{k=1}^{n} x_k^{\hat{B}_{jk}}, \quad i = 1, \ldots, n \tag{5.14}$$

where the parameters $\hat{\lambda}_i$ and $\hat{A}_{ij}$ depend linearly on the feedback parameters according to the equations (5.5) and (5.6).

However, with the BMI (5.7) it is not possible to prescribe the equilibria of the closed loop system but only to globally stabilize it. So it is necessary to introduce extra parameters to the feedback in order to be able to place the positive steady state point anywhere in the positive orthant as needed. The feedback structure has to be constructed in a way that the parameters that are used in the *steady state point placing problem* appear in the vector $\hat{\boldsymbol{\lambda}}$ of the closed loop quasi-polynomial system. This way the parameters of the equilibrium placing are separated from the stabilizing feedback design BMI's parameters. The feedback has the form

$$\boldsymbol{u} = \boldsymbol{K}(k, \boldsymbol{x}) + \boldsymbol{D}(\boldsymbol{\delta}, \boldsymbol{x}) \tag{5.15}$$

where $\boldsymbol{K}(k, \boldsymbol{x})$ is the feedback structure with the parameters for the BMI, and $\boldsymbol{D}(\boldsymbol{\delta}, \boldsymbol{x})$ has the form so that the components of the parameter vector $\boldsymbol{\delta}$ appear in the vector $\boldsymbol{\lambda}$ of the closed loop QP system. It is important to note that the QP input (5.4) is linear in both of the parameters k and $\boldsymbol{\delta}$.

One can further simplify the QP input structure (5.4) by using a linear term $D_i(\delta_i, x_i) = \delta_i x_i$ in the feedback (5.15) to take care of the placing of the steady-state point, and the other term for stabilizing the closed loop system.

Fully actuated case In this case the QP system has at least one designated input for each of the n state equations. The steady state point of these systems can be put anywhere in the positive orthant.

$$0 = \lambda_i(\boldsymbol{\delta}) + \sum_{j=1}^{m} A_{ij} \prod_{k=1}^{n} x_k^{*B_{jk}}, \quad i = 1, \ldots, n \tag{5.16}$$

where $\lambda_i(\boldsymbol{\delta})$ is a linear function of the δ parameters of the problem and $\boldsymbol{x}^* = (x_1^*, \ldots, x_n^*)^T$ is the desired equilibrium. That is, $\boldsymbol{\delta}$ can be determined from a linear system of equations.

Partially actuated case If the system has $k < n$ different inputs, then there are no general results for QP models. However, in the Lotka-Volterra case there is some possibility of shifting some components of the equilibrium point. If the LV coefficient matrix $\boldsymbol{M}$ can be transformed into an upper block triangular matrix by row and column changes then it means that the first k coordinates of the equilibrium point can be prescribed at will independently of the remaining $n-k$.

Note that if the system does not belong to the above two classes then it is not possible to redesign its equilibrium point with the above technique.

Rank deficient (embedded) systems In case of systems that are not originally in quasi-polynomial form (see Section 2.2.3 for embedding into QP-form) all the above hold with some specialities. It is known that for such QP systems that their trajectories range only a lower dimensional manifold of the QP state space and their parameter matrix A is rank deficient. With this understanding one has to design the equilibrium point of the system (if it is possible to design at all, see Section 5.2.4) into this lower dimensional manifold.

Feedback design for a simple fermentation process This example presents a fermentation process similar to the one presented in Section A.4 of the Appendix, just the reaction kinetics (i.e. function $\mu(x_2)$) is different. This one is a monotonous function of the substrate concentration x_2, that results in a simpler nonlinearity. The system is described by the non-QP input-affine state-space model

$$\begin{aligned} \dot{x}_1 &= \mu(x_2)x_1 + \tfrac{(X_F - x_1)F}{V} \\ \dot{x}_2 &= -\tfrac{\mu(x_2)x_1}{Y} + \tfrac{(S_F - x_2)F}{V} \\ \mu(x_2) &= \mu_{max}\tfrac{x_2}{K_S + x_2}, \end{aligned} \tag{5.17}$$

where the inlet substrate and biomass concentrations denoted by S_F and X_F, are the manipulated inputs. The variables and parameters of the model together with their units and parameter values are given in Table A.4. The parameter values are taken from [61].

The system has a unique locally stable equilibrium point in the positive orthant:

$$\begin{bmatrix} \bar{x}_1 \\ \bar{x}_2 \end{bmatrix} = \begin{bmatrix} 0.6500 \\ 0.4950 \end{bmatrix} \tag{5.18}$$

with steady-state inputs

$$\begin{bmatrix} \bar{X}_F \\ \bar{S}_F \end{bmatrix} = \begin{bmatrix} 0.6141 \\ 4.3543 \end{bmatrix}.$$

By introducing a new differential variable $\eta = \frac{1}{K_S + x_2}$ one arrives at a third differential equation

$$\begin{aligned} \dot{\eta} &= -\tfrac{1}{(K_S+x_2)^2}\cdot\tfrac{dx_2}{dt} = -\eta^2\cdot\left(-\tfrac{\mu_{max}}{Y}x_1x_2\eta + \tfrac{(S_F-x_2)F}{V}\right) = \\ &= \eta\left(\tfrac{\mu_{max}}{Y}x_1x_2\eta^2 + \tfrac{F}{V}x_2\eta - S_F\tfrac{F}{V}\eta\right) \end{aligned} \tag{5.19}$$

that completes the ones for x_1 and x_2. Thus the original system (5.17) can be represented by the following three quasi-polynomial differential equations:

$$\begin{aligned} \dot{x}_1 &= x_1\cdot\left(-\tfrac{F}{V} + \mu_{max}x_2\eta + \tfrac{F}{V}x_1^{-1}X_F\right) \\ \dot{x}_2 &= x_2\cdot\left(-\tfrac{F}{V} - \tfrac{\mu_{max}}{Y}x_1\eta + \tfrac{F}{V}x_2^{-1}S_F\right) \\ \dot{\eta} &= \eta\cdot\left(\tfrac{F}{V}x_2\eta + \tfrac{\mu_{max}}{Y}x_1x_2\eta^2 - \tfrac{F}{V}\eta S_F\right). \end{aligned}$$

Using a wise choice of the feedback structure, the quasi-monomials of the closed loop system may decrease. In our case the feedback structure is chosen to be

$$\begin{aligned} X_F &= k_1 x_1 x_2 \eta + \delta_1 x_1 \\ S_F &= k_2 x_1 x_2 \eta + \delta_2 x_2. \end{aligned}$$

The closed loop QP system is then

$$\begin{aligned} \dot{x}_1 &= x_1 \cdot \left(-\tfrac{F}{V} + \left(\mu_{max} + k_1 \tfrac{F}{V}\right) x_2 \eta\right) \\ \dot{x}_2 &= x_2 \cdot \left(-\tfrac{F}{V} + \left(-\tfrac{\mu_{max}}{Y} + k_2 \tfrac{F}{V}\right) x_1 \eta\right) \\ \dot{\eta} &= \eta \cdot \left(\tfrac{F}{V} x_2 \eta + \left(\tfrac{\mu_{max}}{Y} - k_2 \tfrac{F}{V}\right) x_1 x_2 \eta^2\right). \end{aligned}$$

Note, that for the globally stabilizing feedback design phase parameters δ_1, and δ_2 are set to zero, since they will be used for shifting the equilibrium of the closed loop system to the original fermenter's one. It is apparent that the closed loop system has only 3 quasi-monomials: $x_2\eta, x_1\eta, x_1 x_2 \eta^2$.
The solution of the BMI problem gives the feedback gain parameters

$$\begin{aligned} k_1 &= -1.5355 \\ k_2 &= 43.6516, \end{aligned}$$

which makes the system globally asymptotically stable (in the positive orthant) with the Lyapunov function (5.1) having parameters:

$$c_1 = 0.0010, \quad c_2 = 0.0761, \quad c_3 = 0.0760.$$

The equilibrium (5.18) of the open loop fermenter can be reset by expressing δ_1, and δ_2 from the steady-state equations. This gives $\delta_1 = 1.7152$, $\delta_2 = -20.9293$, so the equilibrium point (5.18) of the fermentation process (5.17) is globally stabilized.

Partially actuated example in QP-form The system of this example is a simpler variant of the fermentation process of Section A.4 with S_F being the manipulable input:

$$\begin{aligned} \dot{x}_1 &= \mu_{max} x_1 x_2 - \tfrac{F}{V} x_1 \\ \dot{x}_2 &= -\tfrac{\mu_{max}}{Y} x_1 x_2 + \tfrac{F}{V}(S_F - x_2). \end{aligned} \tag{5.20}$$

The parameter values can be seen in Table 5.1. The quasi-polynomial form of the

Table 5.1: Variables and parameters of the fermenter model (5.20)

X	biomass concentration		$[\frac{g}{l}]$
S	substrate concentration		$[\frac{g}{l}]$
F	inlet feed flow rate	2	$[\frac{l}{h}]$
V	volume	1	$[l]$
S_F	substrate feed concentration		$[\frac{g}{l}]$
Y	yield coefficient	1	-
μ_{max},	kinetic parameter	1	$[\frac{1}{h}]$

model is:

$$\begin{array}{rcl} \dot{x}_1 & = & x_1 \left(S - 2\right) \\ \dot{x}_2 & = & x_2 \left(-x_1 + 2x_2^{-1} S_F - 2\right). \end{array} \tag{5.21}$$

For a fixed value of the substrate concentration $S_F^* = 1$, the system has an asymptotically stable wash-out type equilibrium point

$$\begin{bmatrix} x_1^* \\ x_2^* \\ S_F^* \end{bmatrix} = \begin{bmatrix} 0 \\ 1 \\ 1 \end{bmatrix}.$$

The feedback structure was chosen to be

$$S_F = k_1 x_2^2 + \delta_1 x_2.$$

The closed loop system with the above structure is

$$\begin{array}{rcl} \dot{x}_1 & = & x_1 \left(x_2 - 2\right) \\ \dot{x}_2 & = & x_2 \left(-x_1 + 2k_2 x_2 + 2(\delta_1 - 1)\right). \end{array} \tag{5.22}$$

It is apparent, that the above QP model (5.22) is also the Lotka-Volterra model of the system. The LV matrices of the system are the following ones:

$$M = \begin{bmatrix} 0 & 1 \\ -1 & 2k_1 \end{bmatrix}, \quad N = \begin{bmatrix} -2 \\ 2(\delta_1 - 1) \end{bmatrix}.$$

It is noticeable that matrix M is not upper triangular, i.e. the equilibrium cannot be manipulated partially based on the results of section 5.2.4. However, with a fortunate choice of δ_1 (e.g. $\delta_1 = 2.5$) one can modify the value of the (non wash-out type) equilibrium of system (5.22). It is important to note, that in this case the equilibrium will be positive, but one cannot decide its value. The other free parameter (k_1) can be used for stabilizing this equilibria. So k_1 and the two parameters of the Lyapunov function are given to the ILMI algorithm. It gives the following results:

$$k_1 = -0.0013, \quad C = \begin{bmatrix} 1.2822 & 0 \\ 0 & 1.2822 \end{bmatrix}.$$

Figure 5.1. shows the feasibility region of the globally stabilizing BMI problem and the solution given by the ILMI algorithm of section 5.2.3. The obtained feedback with parameters k_1 and δ_1 globally stabilizes the system in the positive orthant. Indeed, the closed loop system has a unique equilibrium state

$$\begin{bmatrix} \bar{x}_1 \\ \bar{x}_2 \end{bmatrix} = \begin{bmatrix} 2.9948 \\ 2.0000 \end{bmatrix}$$

in the positive orthant $\mathrm{int}(\mathbb{R}_+^2)$, for which the locally linearized system matrix has eigenvalues with strictly negative real part, this way at least local stability can be proved for the equilibrium.

Some further examples of quasi-polynomial state feedback design method are presented in Section A.5.

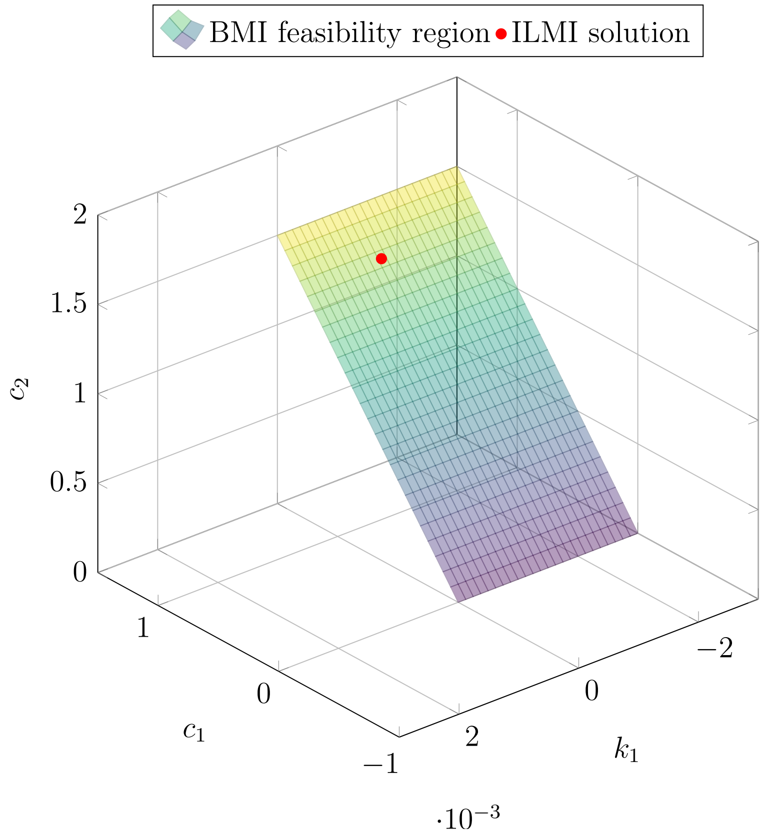

Figure 5.1: BMI feasibility region for Example 5.2.4

5.3 Summary

A general optimization based framework has been proposed in this chapter that uses the convenient properties of quasi-polynomial and Lotka-Volterra system classes.

It was shown in Section 5.1, that the negative definiteness condition of the Lyapunov function of QP and LV systems is equivalent to a linear matrix inequality, thus the stability analysis of QP systems (and general nonlinear process systems embedded into QP form) is equivalent to the feasibility of a constrained optimization problem. The linear matrix inequality is non-strict if the model has been obtained by embedding.

The global stability analysis has been extended to a wider class of QP systems by embedding the parameters of the time-reparametrization transformation into the global stability analysis, when one has to solve a bilinear matrix inequality feasibility problem.

A globally stabilizing state feedback design problem was formulated in Section 5.2 using the global stability analysis results of Section 5.1.1. The problem has been solved as a bilinear matrix inequality feasibility problem, having two groups of variables, one for the parameters of the Lyapunov function and another for the feedback gains. The proposed method does not utilize the objective function of the BMI optimization problem (2.28), thus it is a possible point to introduce some performance or robustness specifications.
If one is to solve just the BMI feasibility without additional criteria, the problem has been reformulated so that an existent iterative LMI algorithm is suitable for its' solution.

The stabilizing state feedback may shift the closed loop system's equilibrium points into unwanted values that's why the possibilities of designing an additional feedback that (partially) sets back the original steady state were proposed. It was shown that under certain conditions on the closed loop system's Lotka-Volterra coefficient matrix it is possible to design such a controller. It's parameters were determined from a linear set of equations. In most cases, however, it is only possible to redesign the steady state for only a few number of state coordinates.

Chapter 6

Conclusions

6.1 New scientific results

The new scientific contributions of the thesis are summarized in the following thesis points. Thesis points 1, 2 and 3 are related to Chapters 3, 4 and 5 of the dissertation, respectively. The corresponding publications are listed at the end of each thesis point.

1. **Model-based methods for energy systems**
   I have developed model-based methods for the optimal operation and the parameter estimation of home appliances and batteries.

   (a) I have formulated the cost optimal scheduling of a class of energy related electrical home appliances as a model predictive optimal scheduling problem where the scheduling variable determines the binary operation mode of the system, the cost function is the operation cost of the appliance in the presence of hourly changing electricity price. I have presented a branch-and-bound heuristic optimization algorithm to solve the above problem. Afterwards, I have extended the heuristic model predictive scheduling algorithm so that it is capable of adaptive operation, following the change in the key parameter(s) of the underlying dynamics.

   (b) I have proposed a prediction error minimization based parameter estimation method that is capable of identifying the thermal behavior of lithium-ion batteries. The basis of the method is a nonlinear charge and discharge model which describes the temperature dependency as a parametric function of temperature as an independent variable. The proposed parameter estimation method determines point estimates of the key battery parameters at different temperatures, afterwards, by interpolating the parameter values between the point estimates a thermal characteristics of the battery parameters is obtained.

   Related publications: [120], [142], [121], [123], [122], [141], [143].

2. **Optimization based input design for the power grid**
   I have developed model-free direct optimization-based compensation methods for electrical networks.

   (a) I have proposed a direct optimization based compensator structure capable of decreasing the total harmonic distortion of one phase low voltage electrical networks with unknown network model or topology. The cost function of the optimization problem is constructed from the higher order harmonics of the voltage measured at the connection point. The suggested compensator structure reduces the harmonic distortion by a non-sinusoidal current input to the grid where the injected current harmonics magnitudes and phases serve as the optimization variable for the applied derivative-free optimization method.

(b) I have shown that the symmetric difference between the ideal three-phase voltage phasor and that of the three-phase voltage measured at the connection point can serve as the cost function of a direct optimization-based voltage unbalance compensation structure. Moreover, I have formulated the problem of voltage unbalance compensation in the case of unknown network model as an optimization problem. I have analyzed the performance of the method by dynamical simulation based experiments using a conceptual network and inverter model and concluded that the proposed unbalance optimizer together with the proposed norm successfully decrease voltage unbalance and perform better then the widely used voltage unbalance factor.

Related publications: [125], [129], [124] [138], [126], [127] [140], [136], [135], [137].

3. **Control of smooth nonlinear systems in quasi-polynomial and Lotka-Volterra form**
I have developed new optimization based computational methodfor the stabilizing feedback control of smooth nonlinear systems being in Lotka-Volterra representation.

(a) I have formulated the global stability analysis of smooth nonlinear dynamical systems being in quasi-polynomial representation as the feasibility problem of a linear matrix inequality.

(b) I have formulated the globally stabilizing controller design problem for smooth nonlinear systems being in quasi-polynomial form. The control law is a nonlinear state feedback such that the closed loop system is a quasi-polynomial one. I have reformulated the problem as the feasibility of a set of bilinear matrix inequalities. I have proposed an iterative LMI-based solution method to solve globally stabilizing feedback design problem.

Related publications: [133], [144], [131], [132], [139].

6.2 Utilization of the results and future work

6.2.1 Model-based methods for energy systems

The proposed optimal heuristic model predictive scheduling method can be applied to different household equipment with similar dynamics (water heater, air conditioner, etc.). Multiple household equipments could be operated in parallel by an improved version of the algorithm in order to avoid short consumption peaks when operating such devices at the same time. The method can serve as a key component in the flexibility-related operation of residential prosumers [119]. In such approaches, the prosumers can give an estimated amount with they can increase or decrease their actual power consumption (or generation). This information can be used by the system operator for scheduling purposes.

The proposed temperature dependent parameter estimation method together with the thermo-electric battery model can serve as a basis for model-based optimal charge control methods for lithium-ion batteries [130]. On the other hand determining the state of health of the battery, and to estimate the temperature dependent state of charge during its life cycle is of key importance in electric vehicle applications. This is possible through a suitable experiment and estimation policy that gives estimates the battery parameters based on high quality (in the system identification sense) measurements.

6.2.2 Model-free optimal compensation of power grid

Both model-free optimization directions proposed in the thesis has a wide range of potential improvements and further research directions. As the virtual powerplants are getting more and more widespread, several residential prosumers having the potential to improve power quality could work together, under the control of the system operator. The parallel operation of several devices within the same local transformer area is also an interesting question that will be investigated in the future.

The inclusion of constraints to the optimization problem is an obvious step of future research which may also result in different, computationally more effective algorithms.

The symmetrical difference based unbalance measure will be further investigated to find a computationally effective way of calculating it e.g. on the computational complexity of an embedded system to reach the processing time constants of power electronic devices.

6.2.3 Quasi-polynomial and Lotka-Volterra models

By formulating robustness and/or performance specifications as an objective function it will be possible to prescribe the quality of the controller to be designed. The selection of the feedback controller structure is also an important question since a wise choice can decrease the size of the BMI to be solved. That's why controller structure selection based on graph theoretic methods is another direction of a possible future work. Note, that there is a wide range of structural results for the class chemical reaction networks which have a close connection to quasi-polynomial systems [145].

The controller design BMI with the built-in robustness specifications and the controller structure design together would extend the controller design problem to a complete methodology for the stabilizing control of smooth nonlinear systems given in QP representation.

Passivity based control has been developed in [134] where the entropy-like Lyapunov function of the Lotka-Volterra model serves as the storage function. Mixed mechanical-thermodynamical systems (e.g. gas turbines) can also be embedded into QP representation, and with a Lyapunov function (5.2) their global stability can be investigated. Note, that using a *quadratic Lyapunov function*, the region of their (local) stability can be conveniently determined by solving LMIs.

Appendix A

Appendix

A.1 Model based heuristic scheduling

A.1.1 Optimal scheduling

The numerical values of the discrete-time piecewise affine state space model (3.8) for the two operating modes are listed in (A.1)-(A.3).

$$\mathbf{\Phi}_1 = \begin{bmatrix} 0.9998 & 0.0001 \\ 0.0004 & 0.9977 \end{bmatrix}, \qquad \mathbf{\Phi}_0 = \begin{bmatrix} 0.9998 & 0.0001 \\ 0.0010 & 0.9988 \end{bmatrix} \tag{A.1}$$

$$\mathbf{\Gamma} = \begin{bmatrix} -0.0024 \\ -0.045 \end{bmatrix}, \qquad \boldsymbol{f} = \begin{bmatrix} 0.0022 \\ 0.0028 \end{bmatrix} \tag{A.2}$$

$$\boldsymbol{x} = \begin{bmatrix} T_a \\ T_w \end{bmatrix}, \qquad \boldsymbol{u} = \begin{bmatrix} S \end{bmatrix} \tag{A.3}$$

A.1.2 Case Study of a freezer

A simple case study is used to illustrate the use and the properties of the the proposed cost-optimal scheduling method. A simple freezer (RIO S-68) for storing ice-cream in a shop was used, the parameters of which were estimated using measured data. This model was used to illustrate the operation and properties of the scheduling algorithms.

Freezer modeling and identification

The first step of the model predictive scheduling is to develop a reliable model of the system, in our case a freezer, to be scheduled.

A relatively small freezer operating in a grocery shop is chosen for the case study, that is used for storing ice cream. The containment volume of the freezer is approximately $0.3\,\mathrm{m}^3$ with 9.5 kg ice cream stored in it during the experiments.

The temperature of the containment T_a and that of the wall T_w was measured by Pt100 temperature sensors using 1 s sampling time. The freezer was operating in an automatic temperature regulating mode keeping the -27 ^{o}C setpoint using a conventional hysteresis type on/off controller. The actual status (on/off) of the switch S was also recorded. The electric power of the cooling motor was 240 W.

The measured data were collected for 48 hours using a personal computer.

The piecewise affine model described in subsection 3.1.1 was used for the parameter estimation.

Estimation method A quadratic loss function characterizing the measure of fit was used in the following form:

$$V(\theta) = \int_{t_0}^{t_f} w_a(T_a - \hat{T}_a)^2 + w_w(T_w - \hat{T}_w)^2 \tag{A.4}$$

where $\hat{T}_a$ and $\hat{T}_w$ are the model-predicted values of the containment and the wall temperatures, respectively, θ is the vector of model parameters, and $w_a = 3$, $w_w = 1$ are weighting factors.

The Matlab function `fminsearch` was used for minimizing the above loss function with respect to the parameter values. A plausibility region was given to each parameter based on physical insight that was taken into account during the optimization.

Estimation results Together with the estimated value of the parameters, the value of the loss function (A.4) was also computed as a function of the possible parameter values. The level set curves of the loss function were also investigated and evaluated in order to gain information about the correlation of the estimated parameter values and about sensitivities with respect to parameter variations.

The results indicated that the estimates of some parameter pairs, for example of (T_c, K_c) are highly correlated, in this case physical insight was used to choose the actual value of one of them. Using this regularization, the estimated values shown in Table A.1 were obtained.

Table A.1: Estimated freezer parameter set

meaning	symbol	estimated value	unit
cooling liquid temperature	T_c	-43.6	°C
air-wall heat transfer coeff.	K_w	0.0241	$\frac{\mathrm{kW}}{°\mathrm{C}}$
air-env. heat transfer coeff.	K_o	0.0021	$\frac{\mathrm{kW}}{°\mathrm{C}}$
wall-env. heat transfer coeff.	K_x	0.0186	$\frac{\mathrm{kW}}{°\mathrm{C}}$
wall-cool. liq. heat transfer coeff.	K_c	0.173	$\frac{\mathrm{kW}}{°\mathrm{C}}$
heat capacity of the containment	C_a	40.1	$\frac{\mathrm{kJ}}{°\mathrm{C}}$
heat capacity of wall	C_w	71.4	$\frac{\mathrm{kJ}}{°\mathrm{C}}$

The quality of the estimation is characterized by plotting the measured containment and wall temperatures against their model predicted values using the estimated parameter values in the model. In Figure A.1 a good agreement of the measured and model predicted temperatures are shown that indicates the good quality of the model for model predictive scheduling purposes.

Sensitivity investigations

We investigated the sensitivity of the model predicted temperatures with respect to the critical model parameter, the heat capacity of the containment C_a. This parameter depends on the mass and specific heat of the containment content, that is the goods stored in the freezer (in our case the ice cream). This parameter may change in time depending on the load and consumption of the stored freezer content.

The sensitivity analysis shows that the estimated value of C_a is independent of the other parameters (no high correlation is observed), and it influences critically the

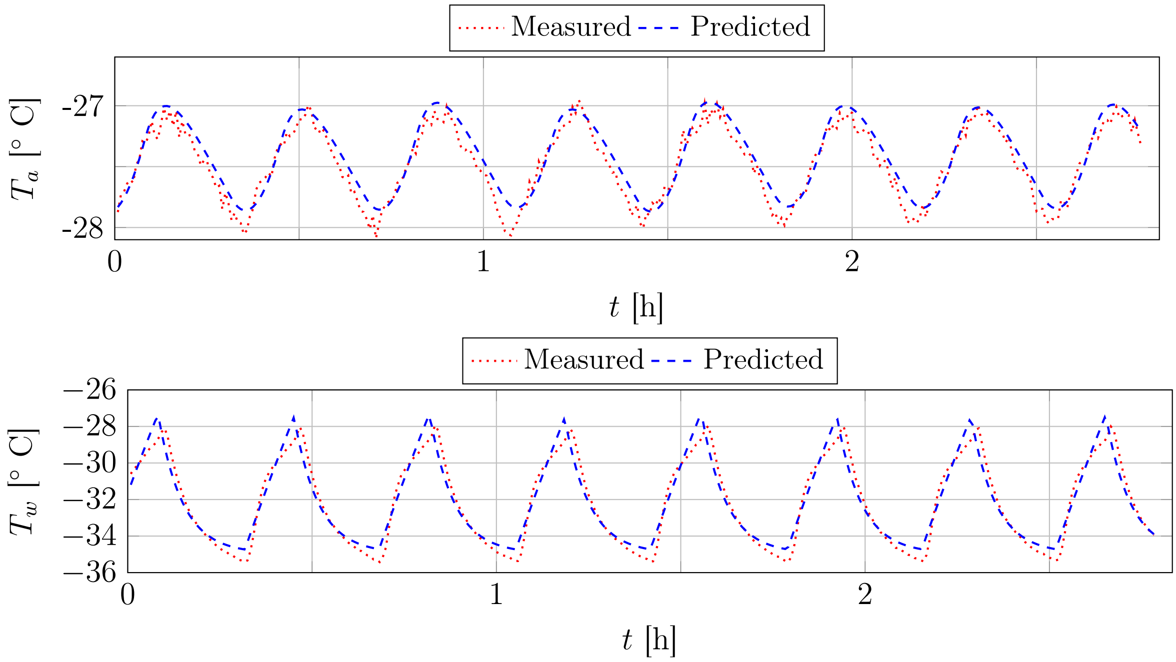

Figure A.1: The measured and model predicted temperatures

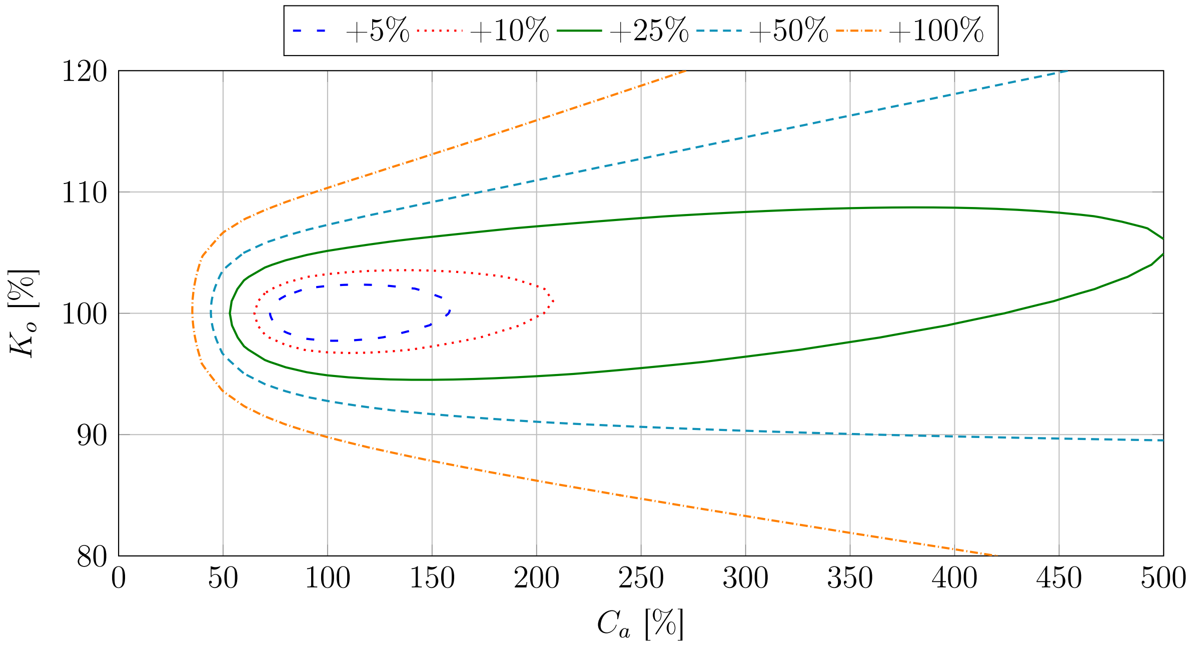

Figure A.2: The level set curves of the loss function with K_o and C_a parameters

model response. Figure A.2 shows the level set curves of the loss function in the parameter sub-space for the parameters K_o and C_a. A definite sharp minimum is observed, that shows the strong influence of C_a on the loss.

The upper plot shows the interior air temperature (T_a) of the system controlled by the non-adaptive MPC for Wednesday. The dashed line denotes the temperature calculated by the MPC algorithm, the solid line corresponds to the actual interior air temperature of the simulated freezer. The second plot is similar, but the dashed line denotes the inner air temperature calculated by the adaptive MPC algorithm (that iteratively re-estimates the heat capacity C_a). On the first two plots dotted line

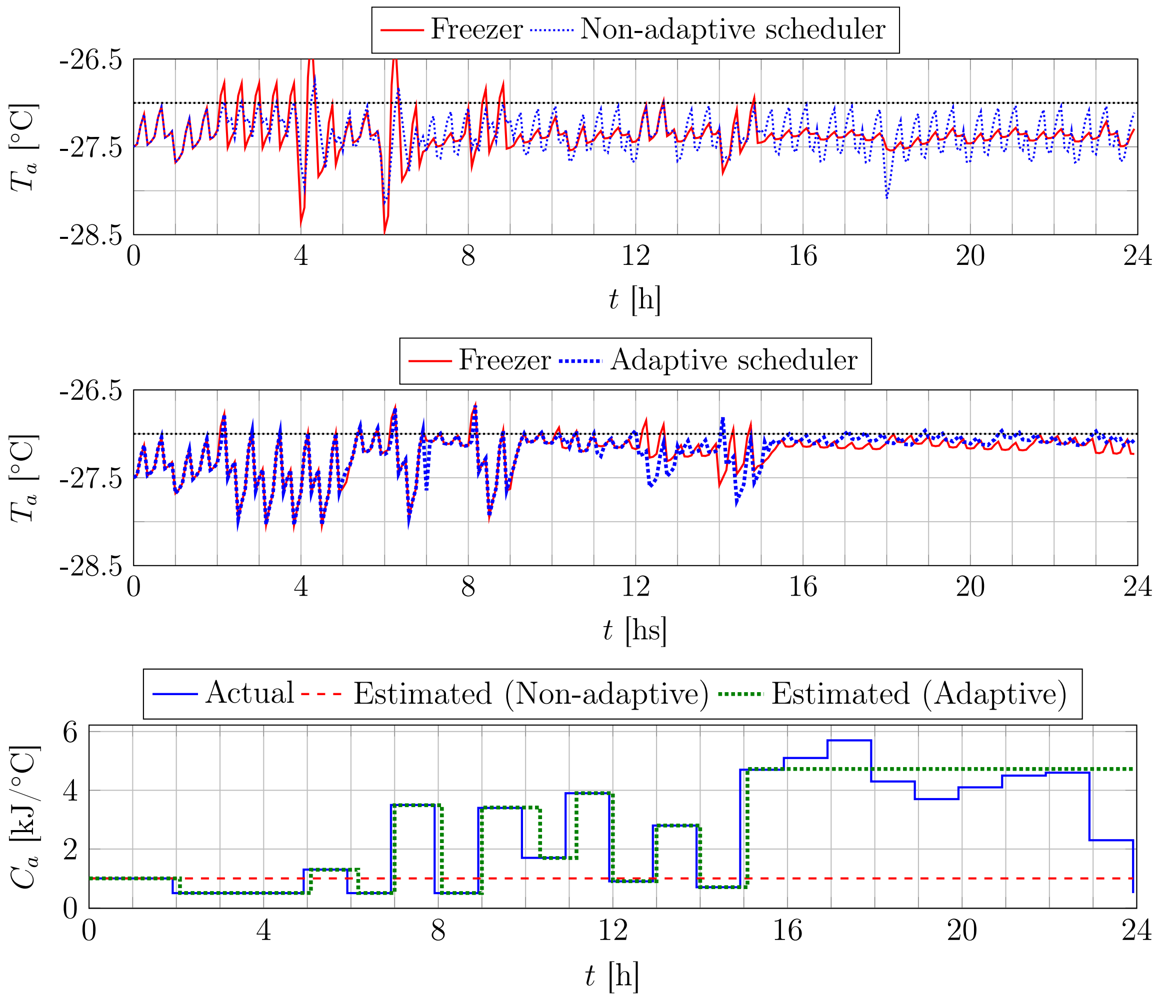

Figure A.3: Top: Operation of the non-adaptive MPC algorithm. Black dashed line denotes the upper temperature limit; Middle: Operation of the adaptive MPC algorithm; Bottom: Actual heat capacity of the system (solid), heat capacity at the beginning of the simulation and being used by the non-adaptive algorithm (dashed) and the estimated heat capacity used by the adaptive algorithm (dotted).

denotes the upper limit of the air temperature, $T_{a,max}$. The plot at the bottom shows the actual value of the heat capacity C_a that changes due to the changing goods in the freezer, the non-adaptive MPC is supposed to know the heat capacity at the initial time (dashed) while the adaptive algorithm follows the actual value be re-estimating the parameter C_a if the condition (3.13) is true.

It is easy to see, that due to the lack of correct information about the heat capacity, the non-adaptive scheduler operates in a conservative way and (e.g. after 15:00) keeps the temperature at a level lower than it is necessary. Moreover, when the non-adaptive scheduler overestimates the heat capacity of the system and the price level increases at the next hour (e.g. at 4:00 and 6:00), the system tends to overshoot, as it can be seen on the upper plot. The middle plot shows the case of adaptive scheduling: due to the estimated actual heat capacity C_a^{est}, the scheduler uses a more precise model of the freezer and able to set a temperature nearer to the upper limit that yields a lower cost of the operation (see Table A.2).

The bottom plot shows a few situations when the adaptive MPC uses a higher C_a^{est} value than the actual C_a^{act} of the freezer, e.g. at 7:00 am. In such cases the air temperature violates the upper temperature limit for a short period, due to the fact, that the scheduler overestimates the heat capacity (and thus the time constant) of the system.

Table A.2: The daily operating costs [€/kWh] for $H = 2$ hours in the case of the nonadaptive and the adaptive algorithms.

Algorithm	Mon.	Tu.	Wed.	Th.	Fri.	Sat.	Sun.
Nonadaptive	0.440	0.442	0.604	0.484	0.503	0.563	0.595
Adaptive	0.430	0.430	0.589	0.474	0.491	0.550	0.580

A.2 Nonlinear distortion compensation

A.2.1 Inverter model

An extended version of the current source inverter model applied in Section 4.1.2 is presented in Figure A.4, where the battery charge/discharge operation os controlled by switches S_6 and S_7.

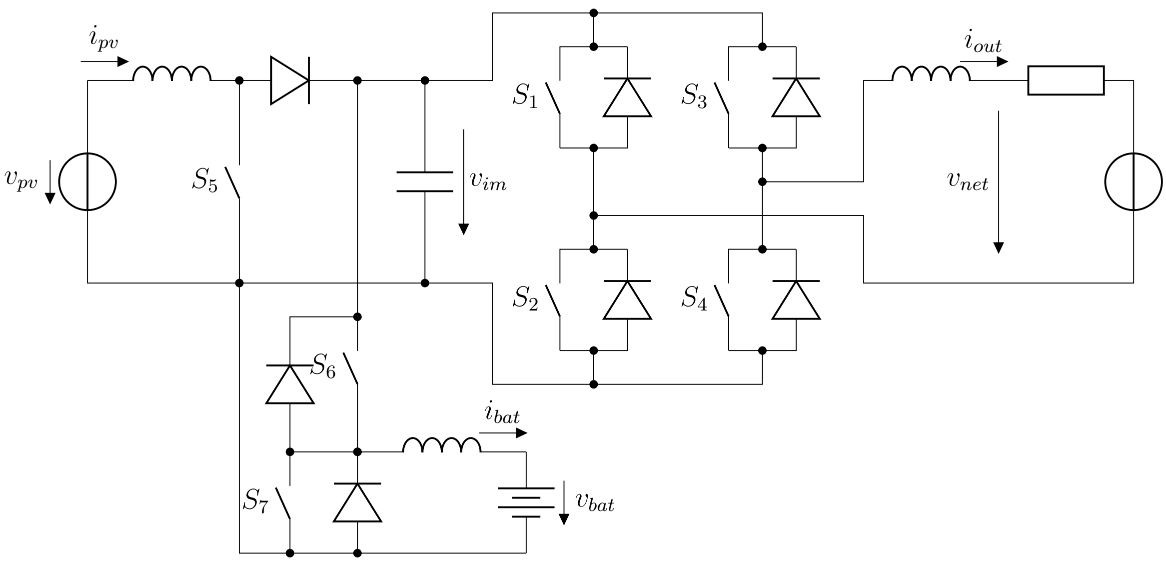

Figure A.4: Grid-tie inverter model that connects the renewable photovoltaic energy source to the main grid. The circuit also contains the battery charger and the lithium-ion battery

A.2.2 Matlab based simulation model

The nonlinear distorted network model was developed in Matlab Simulink environment. The model contains the proposed compensator and controller elements, renewable soure and the typical elements of the nonlinear network presented in Section 4.1.2.

- mid-voltage transformer - voltage generator with serial inductance

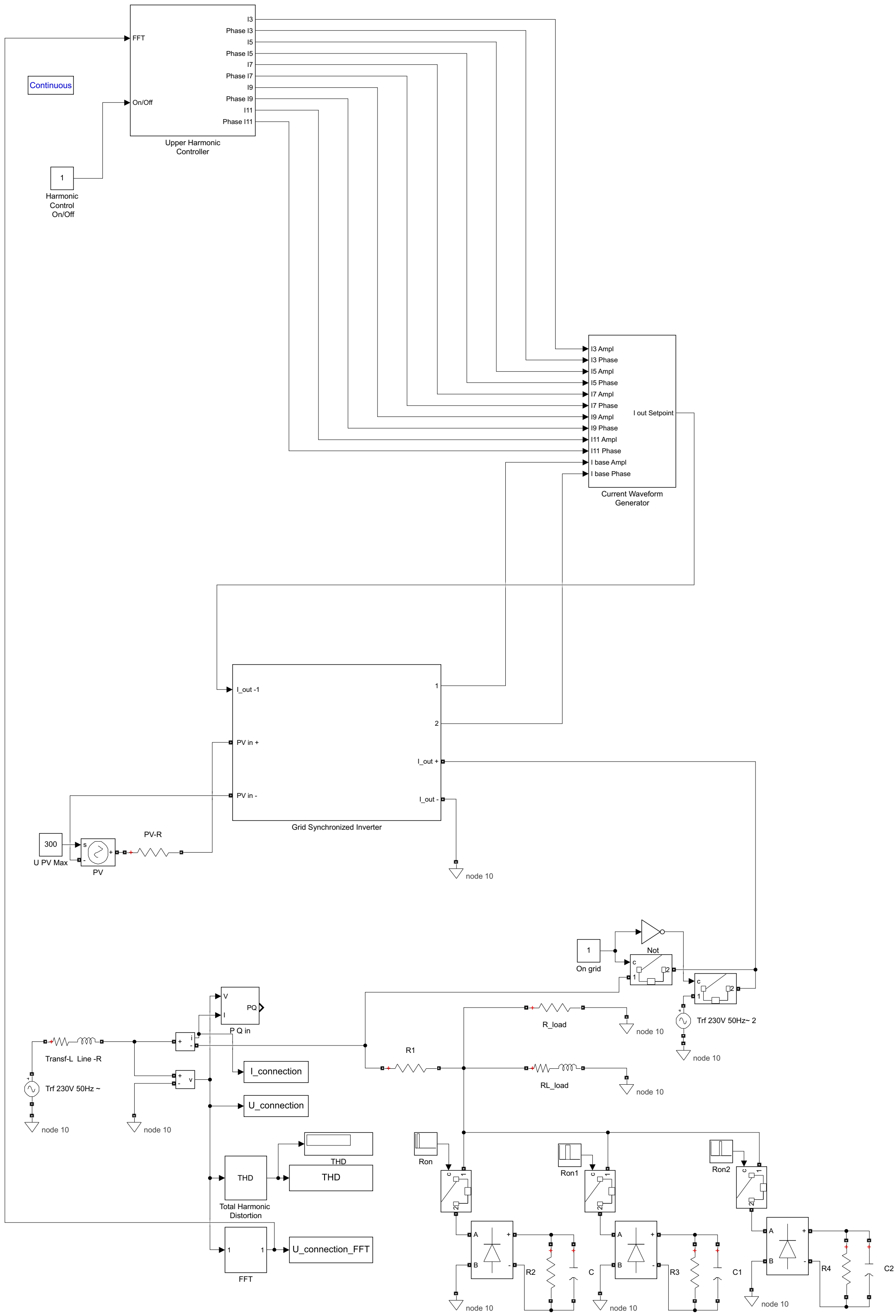

Figure A.5: Top level Matlab Simulink model of the system consisting of the power source, nonlinear network with typical elements (loads), battery and the THD compensator

- wires - modeled with ohmic loss resistance

- linear ohmic loads - modeled with ohmic resistance

- linear inductive loads - modeled with serial resistance and inductance

- nonlinear loads - built from with capacitance and diodes with highly nonlinear characteristics

- battery model

- grid synchronous inverter model

The top level Matlab Simulink model of the high fidelity simulation modelcan be seen in Figure A.5.

A.3 Voltage unbalance compensation

A.3.1 Asymmetric inverter model

A simple asymmetric inverter circuit can be seen in Figure A.6. The basis of the inverter is the single phase inverter (Figure 4.2) used in Section 4.1.2. In principle, three such inverters are connected to the three phases and are connected to a common ground.

A.3.2 Matlab based simulation model

The top level structure of the Matlab Simulink model of the three-phase network with loads, rooftop solar panel, battery and the unbalanced network can be seen in Figure A.7.

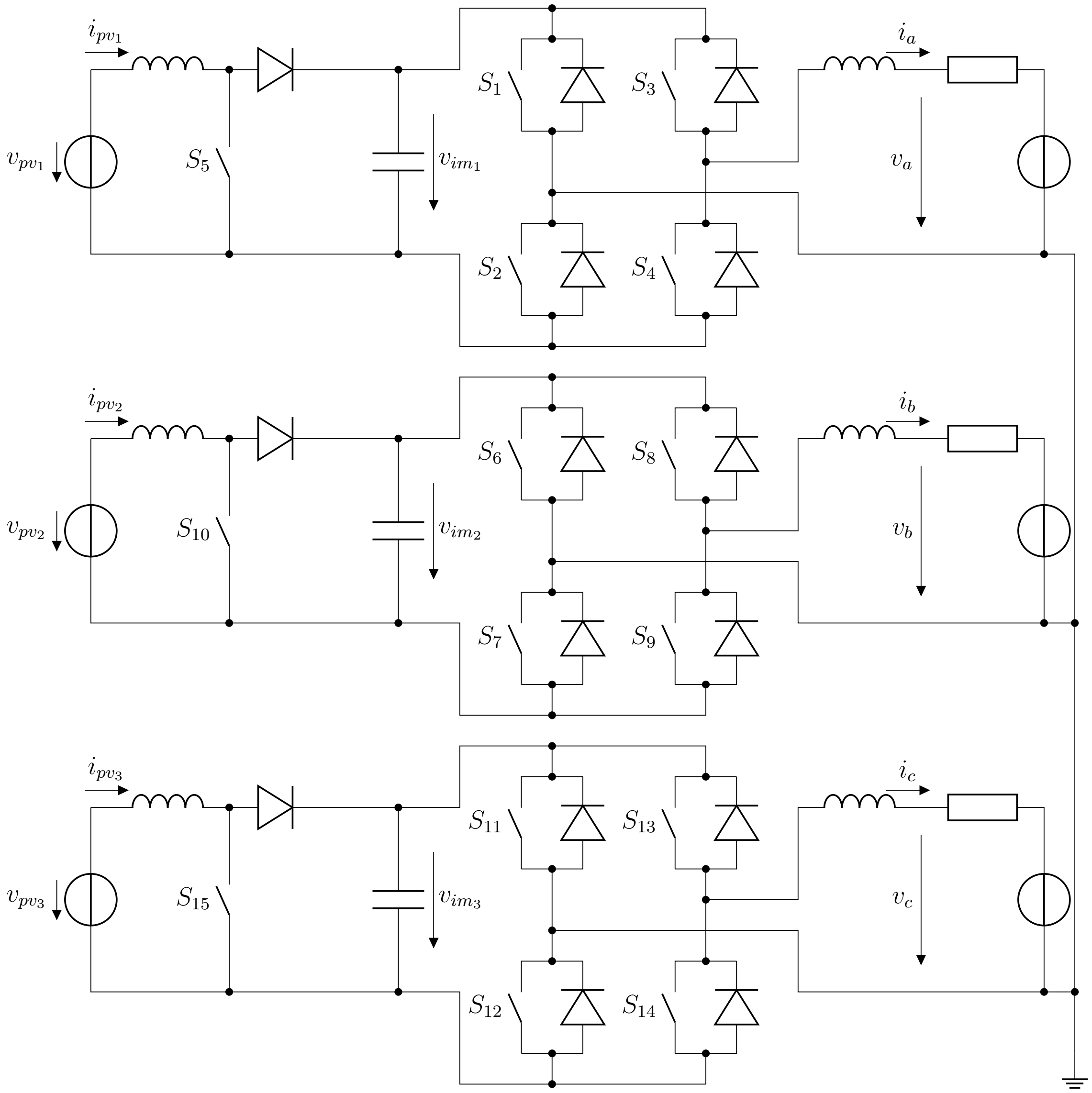

Figure A.6: Grid-tie inverter model that connects the renewable photovoltaic energy source to the main grid

A.4 Embedding general nonlinear systems into quasi-polynomial form

A simple fermentation example illustrates the way of embedding non-QP system models into QP-form and the special properties of process system models in QP-form. Consider a simple fermentation process with non-monotonous reaction kinetics that is described by the non-QP input-affine state-space model

$$\begin{aligned}
\dot{x}_1 &= \mu(x_2)x_1 + \frac{(X_F - x_1)F}{V} \\
\dot{x}_2 &= -\frac{\mu(x_2)x_1}{Y} + \frac{(S_F - x_2)F}{V} \\
\mu(x_2) &= \mu_{max}\frac{x_2}{K_2x_2^2 + x_2 + K_1}
\end{aligned} \tag{A.5}$$

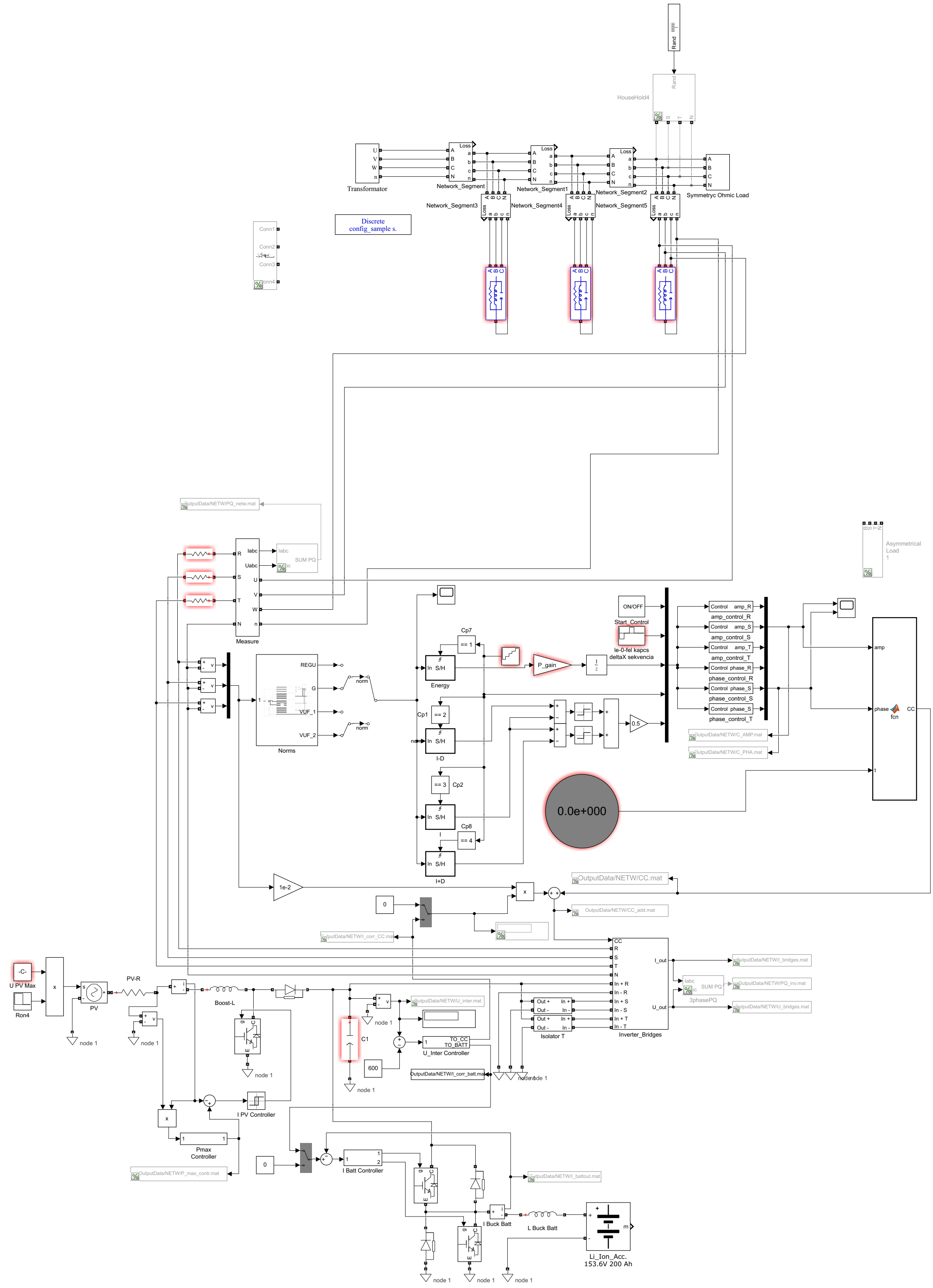

Figure A.7: Top-level structure of the simulation model used for unbalance compensation.

where the state variables x_1 and x_2 are the biomass- and the substrate concentrations respectively. The inlet substrate and biomass concentrations denoted by S_F and X_F, are the manipulated inputs. The variables and parameters of the model together with their units and parameter values are given in Table A.3. The parameter values are taken from [61].

x_1	biomass concentration		$[\frac{g}{l}]$
x_2	substrate concentration		$[\frac{g}{l}]$
S_F	substrate feed concentration		$[\frac{g}{l}]$
X_F	biomass feed concentration		$[\frac{g}{l}]$
F	inlet feed flow-rate	3.2089	$[\frac{l}{h}]$
V	volume	4.0000	$[l]$
Y	yield coefficient	0.5000	-
μ_{max},	kinetic parameter	1.0000	$[\frac{1}{h}]$
K_1	kinetic parameter	0.0300	$[\frac{g}{l}]$
K_2	kinetic parameter	0.5000	$[\frac{l}{g}]$

Table A.3: Variables and parameters of the fermenter model with non-monotonous kinetics (A.5)

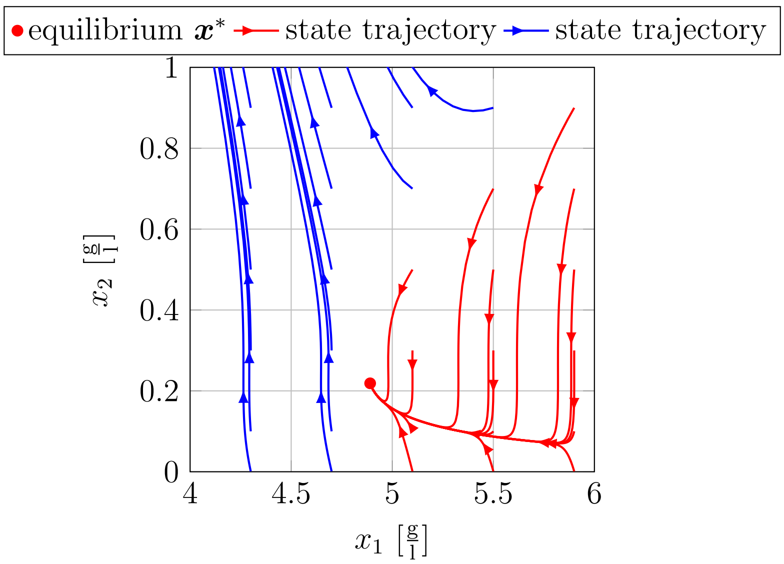

Figure A.8: Some trajectories of the system (A.5). The different trajectories with different colors denote the trajectories converging to different equilibrium states of the system. (The blue trajectories converge to the wash-out equilibrium at $(0, 10)$.)

By introducing a new differential variable $\eta = \frac{1}{K_2 x_2^2 + x_2 + K_1}$ one arrives at a third differential equation

$$\dot{\eta} = -\frac{2K_2 x_2 + 1}{(K_2 x_2^2 + x_2 + K_1)^2} \cdot \dot{x}_2 \tag{A.6}$$

that completes the ones for x_1 and x_2. Thus the original system (A.5) can be represented by three differential equations in input-affine QP-form (2.14):

$$\begin{aligned}
\dot{x}_1 &= x_1\left(\mu_{max}x_2\eta - \frac{F}{V}\right) + x_1\left(x_1^{-1}\frac{F}{V}\right)X_F \\
\dot{x}_2 &= x_2\left(-\frac{\mu_{max}}{Y}x_1\eta - \frac{F}{V}\right) + x_2\left(x_2^{-1}\frac{F}{V}\right)S_F \\
\dot{\eta} &= \eta\left(\frac{2\mu_{max}K_2}{Y}x_1x_2^2\eta^2 + \frac{2K_2F}{V}x_2^2\eta + \frac{\mu_{max}}{Y}x_1x_2\eta^2 + \frac{F}{V}x_2\eta\right) + \\
&\quad +\eta\left(-\frac{2K_2F}{V}x_2\eta - \frac{F}{V}\eta\right)S_F
\end{aligned} \tag{A.7}$$

The system has a locally stable equilibrium point in the positive orthant:

$$\boldsymbol{x}^* = \begin{bmatrix} x_1^* \\ x_2^* \end{bmatrix} = \begin{bmatrix} 4.8906 \\ 0.2187 \end{bmatrix} \tag{A.8}$$

with steady-state inputs

$$\begin{bmatrix} X_F^* \\ S_F^* \end{bmatrix} = \begin{bmatrix} 0 \\ 10 \end{bmatrix}. \tag{A.9}$$

Note, that there is also a so-called wash-out equilibrium where biomass concentration x_1 is zero.

The system can be characterized by the following matrices of the input-affine QP model (2.14):

$$\boldsymbol{A}_0 = \begin{bmatrix} \mu_{max} & 0 & 0 & 0 & 0 & 0 & 0 & 0 \\ 0 & 0 & -\frac{\mu_{max}}{Y} & 0 & 0 & 0 & 0 & 0 \\ \frac{F}{V} & 0 & 0 & 0 & \frac{2\mu_{max}K_2}{Y} & \frac{2K_2F}{V} & \frac{\mu_{max}}{Y} & 0 \end{bmatrix}$$

$$\boldsymbol{A}_1 = \begin{bmatrix} 0 & \frac{F}{V} & 0 & 0 & 0 & 0 & 0 & 0 \\ 0 & 0 & 0 & 0 & 0 & 0 & 0 & 0 \\ 0 & 0 & 0 & 0 & 0 & 0 & 0 & 0 \end{bmatrix} \quad \boldsymbol{A}_2 = \begin{bmatrix} 0 & 0 & 0 & 0 & 0 & 0 & 0 & 0 \\ 0 & 0 & 0 & \frac{F}{V} & 0 & 0 & 0 & 0 \\ -\frac{2K_2F}{V} & 0 & 0 & 0 & 0 & 0 & 0 & -\frac{F}{V} \end{bmatrix}$$

$$\boldsymbol{B} = \begin{bmatrix} 0 & 1 & 1 \\ -1 & 0 & 0 \\ 1 & 0 & 1 \\ 0 & -1 & 0 \\ 1 & 2 & 2 \\ 0 & 2 & 1 \\ 1 & 1 & 2 \\ 0 & 0 & 1 \end{bmatrix} \quad \boldsymbol{\lambda}_0 = \begin{bmatrix} -\frac{F}{V} \\ -\frac{F}{V} \\ 0 \end{bmatrix} \quad \boldsymbol{\lambda}_1 = \boldsymbol{\lambda}_2 = \begin{bmatrix} 0 \\ 0 \\ 0 \end{bmatrix}. \tag{A.10}$$

The eight quasi-monomials of the QP system model given by the matrices (A.10) are

$$x_2\eta,\ x_1^{-1},\ x_1\eta,\ x_2^{-1},\ x_1x_2^2\eta^2,\ x_2^2\eta,\ x_1x_2\eta^2,\ \eta.$$

The lower dimensional manifold and some trajectories of the system can be seen on Figure A.9. (The inputs X_F and S_F are held constant.)

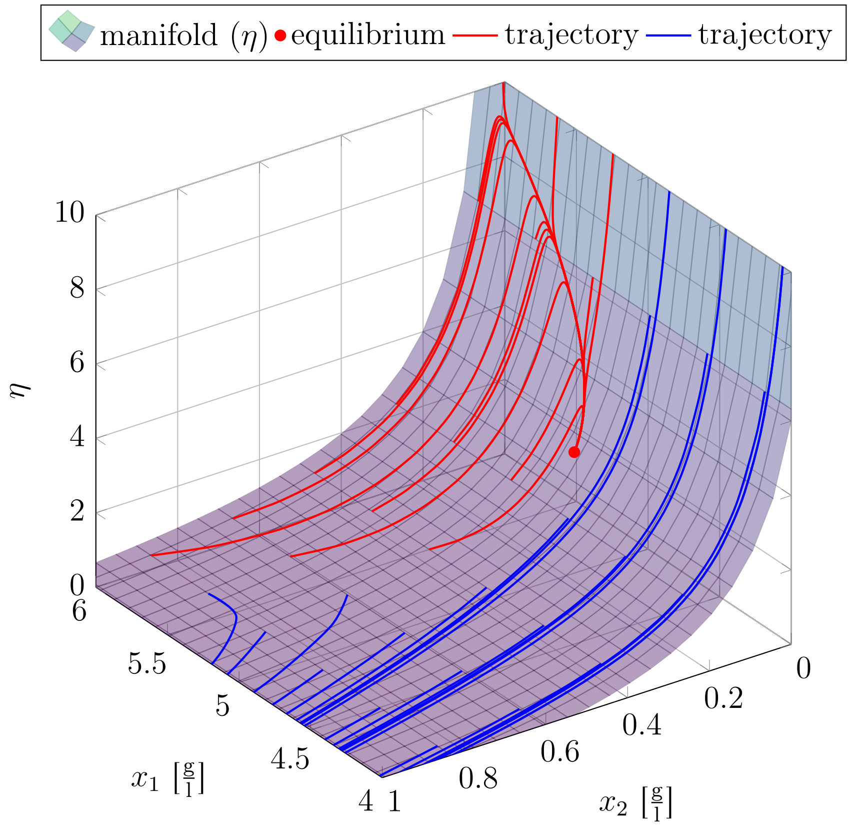

Figure A.9: Some trajectories of the system (A.5) embedded into the QP model (A.7). The different trajectories with different colors denote the trajectories converging to different equilibrium states of the system. The surface corresponds to the lower dimensional manifold defined by the hidden algebraic variable η.

x_1	biomass concentration		$[\frac{g}{l}]$
x_2	substrate concentration		$[\frac{g}{l}]$
S_F	substrate feed concentration		$[\frac{g}{l}]$
X_F	biomass feed concentration		$[\frac{g}{l}]$
F	inlet feed flow-rate	1.0000	$[\frac{l}{h}]$
V	volume	97.8037	$[l]$
Y	yield coefficient	0.0097	-
$\mu_{max},$	kinetic parameter	0.0010	$[\frac{1}{h}]$
K_s	kinetic parameter	0.5	$[\frac{l}{g}]$

Table A.4: Variables and parameters of the fermenter model (5.17)

A.5 Examples for stabilizing QP feedback design

In the following, some simple process system examples are proposed for the BMI based stabilizing controller design problem discussed so far. The first two are simple continuously stirred tank reactor (CSTR) examples with second order chemical reactions where the system model is naturally in a QP-form.

A.5.1 Fully actuated process system example in QP-form

The second process system example is the same fermentation process examined in section 5.2.4 but this time biomass is also fed to the reactor with manipulable inlet concentration X_F. The parameters of the system are the same as in the previous case.

$$\begin{aligned} \dot{x}_1 &= \mu_{max} x_1 x_2 + \tfrac{F}{V}(X_F - x_1) \\ \dot{x}_2 &= -\tfrac{\mu_{max}}{Y} x_1 x_2 + \tfrac{F}{V}(S_F - x_2) \end{aligned} \tag{A.11}$$

The quasi-polynomial form of the model is:

$$\begin{aligned} \dot{x}_1 &= x_1 \left(x_2 + 2x_1^{-1} X_F - 2 \right) \\ \dot{x}_2 &= x_2 \left(-x_1 + 2x_2^{-1} S_F - 2 \right). \end{aligned} \tag{A.12}$$

Note that (A.12) is also the Lotka-Volterra model of the system. The manipulable inputs are X_F and S_F. For fixed values of the input concentrations $X_F^* = 0$ and $S_F^* = 1$, the system has no equilibrium in the strictly positive orthant but has one asymptotically stable wash-out equilibrium on the boundary

$$\begin{bmatrix} x_1^* \\ x_2^* \\ X_F^* \\ S_F^* \end{bmatrix} = \begin{bmatrix} 0 \\ 1 \\ 0 \\ 1 \end{bmatrix}.$$

The feedback structure is chosen to be

$$\begin{aligned} X_F &= k_1 x_1^2 + \delta_1 x_1 \\ S_F &= k_2 x_2^2 + \delta_2 x_2. \end{aligned}$$

Parameters k_1 and k_2 are to stabilize the system, δ_1 and δ_2 will be used to shift the equilibrium. The closed loop system is

$$\begin{aligned} \dot{x}_1 &= x_1 \left(2(\delta_1 - 1) + x_2 + 2k_1 x_1 \right) \\ \dot{x}_2 &= x_2 \left(2(\delta_2 - 1) - x_1 + 2k_2 x_2 \right). \end{aligned}$$

The iterative BMI algorithm yielded the following parameters for the feedback and the Lyapunov function:

$$k_1 = -1.0004, \quad k_2 = -1.0004, \quad C = \begin{bmatrix} 1.0004 & 0 \\ 0 & 1.0004 \end{bmatrix}.$$

We would like to prescribe a strictly positive equilibrium instead of the original one. Suppose that the desired equilibrium is at

$$\begin{bmatrix} \tilde{x}_1 \\ \tilde{x}_2 \end{bmatrix} = \begin{bmatrix} 0.5 \\ 0.5 \end{bmatrix}.$$

Expressing the values of δ_1 and δ_2 from the state equations in which the desired equilibrium point is substituted in yields

$$\delta_1 = 1.2502, \quad \delta_2 = 1.7502.$$

Indeed, the closed loop system with the determined parameters $k_1, k_2, \delta_1, \delta_2$ has an asymptotically stable equilibria in $[\tilde{x}_1, \tilde{x}_2]^T$.

It is apparent that in this example with a higher degree of freedom it was possible to shift the steady state point of the system.

Bibliography

[1] H. Alt, U. Fuchs, G. Rote, and G. Weber. Matching convex shapes with respect to the symmetric difference. *Algorithmica*, 21(1):89–103, 1998.

[2] Z. An, L. Jia, . Wei, C. Dang, and Q. Peng. Investigation on lithium-ion battery electrochemical and thermal characteristic based on electrochemical-thermal coupled model. *Applied Thermal Engineering*, 137:792–807, 2018.

[3] L. R. Araujo, D. R. R. Penido, S. Carneiro, and J. L. R. Pereira. A three-phase optimal power-flow algorithm to mitigate voltage unbalance. *IEEE Transactions on Power Delivery*, 28(4):2394–2402, 2013.

[4] M. Astaneh, R. Dufo-Lopez, R. Roshandel, F. Golzar, and J. L. Bernal-Agustín. A computationally efficient Li-ion electrochemical battery model for long-term analysis of stand-alone renewable energy systems. *Journal of Energy Storage*, 17:93–101, 2018.

[5] K. J. Aström and B. Wittenmark. *Computer-controlled systems.* Prentice Hall, 1997.

[6] Y. Ates, M. Uzunoglu, A. Karakas, A. R. Boynuegri, A. Nadar, and B. Dag. Implementation of adaptive relay coordination in distribution systems including distributed generation. *Journal of cleaner production*, 112:2697–2705, 2016.

[7] P. Báez-González, J. Alejandro, M. A. R. Carlini, and C. Bordons. Day-ahead economic optimization of energy use in an olive mill. *Control Engineering Practice*, 54:91–103, 2016.

[8] A. Battaglini, J. Lilliestam, A. Haas, and A. Patt. Development of supersmart grids for a more efficient utilisation of electricity from renewable sources. *Journal of Cleaner Production*, 17:911–918, 2009.

[9] M. T. Bina and A. Kashefi. Three-phase unbalance of distribution systems: Complementary analysis and experimental case study. *International Journal of Electrical Power & Energy Systems*, 33(4):817–826, 2011.

[10] S. Boyd, L. El Ghaoui, E. Feron, and V. Balakrishnan. *Linear Matrix Inequalities in System and Control Theory.* SIAM, Philadelphia, 1994.

[11] S. Boyd, L. Xiao, and A. Mutapcic. Subgradient methods. *Lecture notes of EE392o, Stanford University, Autumn Quarter*, 2004:2004–2005, 2003.

[12] T. Brekken, N. Mohan, and T. Undeland. Control of a doubly-fed induction wind generator under unbalanced grid voltage conditions. In *2005 European Conference on Power Electronics and Applications*, pages 10–pp. IEEE, 2005.

[13] R. H. Byrd, R. B. Schnabel, and G. A. Shultz. A trust region algorithm for nonlinearly constrained optimization. *SIAM Journal on Numerical Analysis*, 24(5):1152–1170, 1987.

[14] E. F. Camacho and C. B. Alba. *Model predictive control.* Springer Science & Business Media, 2013.

[15] C. Campestrini, G. Walder, A. Jossen, and M. Lienkamp. Temperature influences on state and parameter estimation based on a dual Kalman filter. In *CoFAT*, 2014.

[16] Y.-Y. Cao, J. Lam, and Y.-X. Sun. Static output feedback stabilization: An ILMI approach. *Automatica*, 12:1641–1645, 1998.

[17] J. M. Carrasco, L. G. Franquelo, J. T. Bialasiewicz, E. Galvan, R. C. P. Guisado, M.Á. M. Prats, J. I. Leon, and N. M. Alfonso. Power-electronic systems for the grid integration of renewable energy sources: a survey. *IEEE Transactions on Industrial Electronics*, 53(4):1003–1015, 2006.

[18] A. Cerdeira, M.A. Alema, M. Estrada, and D. Flandre. Integral function method for determination of nonlinear harmonic distortion. *Solid-State Electronics*, 48(12):2225–2234, 2004.

[19] T. H. Chen, C. H. Yang, and N. C. Yang. Examination of the definitions of voltage unbalance. *International Journal of Electrical Power & Energy Systems*, 49:380–385, 2013.

[20] F. J. Christophersen. *Piecewise affine systems.* Springer, 2007.

[21] J. F. G. Cobben. Power quality: about the problems and solutions. 2012.

[22] F. Cucchiella, I. D'Adamo, and S. C. L. Koh. Environmental and economic analysis of building integrated photovoltaic systems in italian regions. *Journal of Cleaner Production*, 98:241–252, 2015.

[23] R. Díaz-Sierra, B. Hernández-Bermejo, and V. Fairén. Graph-theoretic description of the interplay between non-linearity and connectivity in biological systems. *Mathematical Biosciences*, 156:229–253, 1999.

[24] P. Du and N. Lu. Appliance commitment for household load scheduling. *IEEE Transactions on Smart Grid*, 2(2):411–419, 2011.

[25] R. C. Dugan, M. F. McGranaghan, and H. W. Beaty. Electrical power systems quality. *New York, NY: McGraw-Hill,| c1996*, 1996.

[26] W. M. El-Mamlouk, H. E. Mostafa, and M. A. El-Sharkawy. Active power filter controller for harmonic suppression in industrial distribution system. *Ain Shams Engineering Journal*, 2(3-4):161–172, 2011.

[27] F. Feng, R. Lu, G. Wei, and C. Zhu. Online estimation of model parameters and state of charge of LiFePO4 batteries using a novel open-circuit voltage at various ambient temperatures. *Energies*, 8(4):2950–2976, 2015.

[28] A. Figueiredo, I. M. Gléria, and T. M. Rocha. Boundedness of solutions and Lyapunov functions in quasi-polynomial systems. *Physics Letters A*, 268:335–341, 2000.

[29] C. Forgez, D. V. Do, G. Friedrich, M. Morcrette, and C. Delacourt. Thermal modeling of a cylindrical LiFePO4/graphite lithium-ion battery. *Journal of Power Sources*, 195(9):2961–2968, 2010.

[30] C. L. Fortescue. Method of symmetrical co-ordinates applied to the solution of polyphase networks. *Transactions of the American Institute of Electrical Engineers*, 37(2):1027–1140, 1918.

[31] P. Gahinet, A. Nemirovski, A. J. Laub, and M. Chilali. *LMI Control Toolbox Users Guide*. The MathWorks, Inc., 1995.

[32] E. Garcia-Canseco, R. Grino, R. Ortega, M. Salichs, and A. M. Stankovic. Power-factor compensation of electrical circuits: a framework for analysis and design in the nonlinear nonsinusoidal case. *IEEE Control Systems Magazine*, 27(2):46–49, 2007.

[33] I.M. Gléria, A. Figueiredo, and T.M. Rocha Filho. A numerical method for the stability analysis of quasi-polynomial vector fields. *Nonlinear Analysis*, 52:329–342, 2003.

[34] P. Gnaciński, M. Pepliński, D. Hallmann, and P. Jankowski. Induction cage machine thermal transients under lowered voltage quality. *IET Electric Power Applications*, 13(4):479–486, 2019.

[35] J. L. Gouzé. Global stabilization of n-dimensional population models by a positive control. In *Proceedings of the 33rd IEEE Conf. on Decision and Control, Orlando, USA*, pages 1335–1336, 1994.

[36] F. Grognard and J. L. Gouzé. Positive control of Lotka-Volterra systems. In *Proceedings of 16th IFAC World Congress, Prague, Czech Republic*, 2005. on CD.

[37] Y. Han, L. Xu, M. M. Khan, and C. Chen. Control strategies, robustness analysis, digital simulation and practical implementation for a hybrid APF with a resonant AC-link. *Acta Polytechnica Hungarica*, 7(5), 2010.

[38] K. M. Hangos and I. T. Cameron. *Process modelling and model analysis*. Academic Press, London, 2001.

[39] Y. He and Q. G. Wang. An improved ILMI method for static output feedback control with application to multivariable PID control. *IEEE Transactions on Automatic Control*, 51(10):1678–1683, 2006.

[40] M. Herceg, M. Kvasnica, C. Jones, and M. Morari. Multi-parametric toolbox 3.0. In *Proceedings of the European Control Conference*, volume 1, pages 502–510. IEEE, 2013.

[41] B. Hernández-Bermejo. Stability conditions and Lyapunov functions for quasi-polynomial systems. *Applied Mathematics Letters*, 15:25–28, 2002.

[42] B. Hernández-Bermejo and V. Fairén. Nonpolynomial vector fields under the Lotka-Volterra normal form. *Physics Letters A*, 206:31–37, 1995.

[43] B. Hernández-Bermejo and V. Fairén. Lotka-Volterra representation of general nonlinear systems. *Math. Biosci.*, 140:1–32, 1997.

[44] B. Hernández-Bermejo, V. Fairén, and L. Brenig. Algebraic recasting of nonlinear ODEs into universal formats. *J. Phys. A, Math. Gen.*, 31:2415–2430, 1998.

[45] R. Horst and P. M. Pardalos. *Handbook of global optimization*, volume 2. Springer Science & Business Media, 2013.

[46] E. Hosseinzadeh, R. Genieser, D. Worwood, A. Barai, J. Marco, and P. Jennings. A systematic approach for electrochemical-thermal modelling of a large format lithium-ion battery for electric vehicle application. *Journal of Power Sources*, 382:77–94, 2018.

[47] P. D. Hough, T. G. Kolda, and V. J. Torczon. Asynchronous parallel pattern search for nonlinear optimization. *SIAM Journal on Scientific Computing*, 23(1):134–156, 2001.

[48] R. Huisman, C. Huurman, and R. Mahieu. Hourly electricity prices in day-ahead markets. *Energy Economics*, 29(2):240–248, 2007.

[49] A. Isidori. *Nonlinear Control Systems.* Springer-Verlag, 1995.

[50] Sz. Jaskó, T. Schné, and Gy. Simon. Adaptive model-based control for cost-aware household appliances. *Journal of Sustainable Development of Energy, Water and Environment Systems*, 6(3):547–558, 2018.

[51] C. Joe-Wong, S. Sen, S. Ha, and M. Chiang. Optimized day-ahead pricing for smart grids with device-specific scheduling flexibility. *IEEE Journal on Selected Areas in Communications*, 30(6):1075–1085, 2012.

[52] JK Kaldellis, M Simotas, D Zafirakis, and E Kondili. Optimum autonomous photovoltaic solution for the greek islands on the basisof energy pay-back analysis. *Journal of Cleaner Production*, 17(15):1311–1323, 2009.

[53] E. Kaszkurewicz and A. Bhaya. *Matrix Diagonal Stability.* Birkhauser, Boston, 2000.

[54] B. Y. Kim, K. K. Oh, and H. S. Ahn. Coordination and control for energy distribution in distributed grid networks: Theory and application to power dispatch problem. *Control Engineering Practice*, 43:21–38, 2015.

[55] P. G. Kini, R. C. Bansal, and R. S. Aithal. A novel approach toward interpretation and application of voltage unbalance factor. *IEEE transactions on industrial electronics*, 54(4):2315–2322, 2007.

[56] S. Kirkpatrick, C. D. Gelatt, and M. P. Vecchi. Optimization by simulated annealing. *Science*, 220(4598):671–680, 1983.

[57] M. Kocvara and M. Stingl. A code for convex nonlinear and semidefinite programming. *Optimization Methods and Software*, 8:317–333, 2003.

[58] M. Kocvara and M. Stingl. TOMLAB/PENBMI solver (Matlab Toolbox), 2005. PENOPT Gbr.

[59] T. G. Kolda. Revisiting asynchronous parallel pattern search for nonlinear optimization. *SIAM Journal on Optimization*, 16(2):563–586, 2005.

[60] T. G. Kolda and V. J. Torczon. Understanding asynchronous parallel pattern search. In *High Performance Algorithms and Software for Nonlinear Optimization*, pages 323–342. Springer, 2003.

[61] C. Kuhlmann, I. D. L. Bogle, and Z. S. Chalabi. Robust operation of fed batch fermenters. *Bioprocess Engineering*, 19:53–59, 1998.

[62] J. C. Lagarias, J. A. Reeds, M. H. Wright, and P. E. Wright. Convergence properties of the nelder–mead simplex method in low dimensions. *SIAM Journal on optimization*, 9(1):112–147, 1998.

[63] C. Y. Lee, B. K. Chen, W. J. Lee, and Y. F. Hsu. Effects of various unbalanced voltages on the operation performance of an induction motor under the same voltage unbalance factor condition. *Electric Power Systems Research*, 47(3):153–163, 1998.

[64] L. R. Limongi, R. Bojoi, G.Griva, and A Tenconi. Comparing the performance of digital signal processor-based current controllers for three-phase active power filters. *IEEE Industrial Electronics*, 3(1):20–31, 2009.

[65] L. R. Limongi, R. Bojoi, A. Tenconi, and L. Clotea. Single-phase inverter with power quality features for distributed generation systems. In *11th International Conference on Optimization of Electrical and Electronic Equipment*, pages 313–318, 2008.

[66] P. Liu, Y. Chai, P. Gao, and C. Zhang. Research on energy internet based on Lotka-Volterra model. In *2021 3rd International Academic Exchange Conference on Science and Technology Innovation (IAECST)*, pages 1595–1601. IEEE, 2021.

[67] L. Ljung. *System identification: Theory for the user (2nd edition)*. Prentice Hall Inc., New Jersey, 1999.

[68] Y.K. Lo, T.P. Lee, and K.H. Wu. Grid-connected photovoltaic system with power factor correction. *IEEE Transactions on Industrial Electronics*, 55(5):2224–2227, 2008.

[69] A. J. Lotka. *Elements of physical biology*. William and Wilkens, Baltimore, 1925.

[70] Y. Luo and Z. Lu. Stability analysis for Lotka Volterra systems based on an algorithm of real root isolation. *Journal of Computational and Applied Mathematics*, 201:367–373, 2007.

[71] J. Ma, S. J. Qin, and T. Salsbury. Application of economic MPC to the energy and demand minimization of a commercial building. *Journal of Process Control*, 24(8):1282–1291, 2014.

[72] S. S. Madani, E. Schaltz, and S. K. Kær. A review of different electric equivalent circuit models and parameter identification methods of lithium-ion batteries. *ECS Transactions*, 87(1):23–37, 2018.

[73] A. D. Martin, R. S. Herrera, J. R. Vazquez, P. Crolla, and G. M. Burt. Unbalance and harmonic distortion assessment in an experimental distribution network. *Electric Power Systems Research*, 127:271–279, 2015.

[74] M. Mathew, M. Mastali, J. Catton, E. Samadani, S. Janhunen, and M. Fowler. Development of an electro-thermal model for electric vehicles using a design of experiments approach. *Batteries*, 4(2):29, 2018.

[75] The Mathworks, Inc., Natick, Massachusetts. *MATLAB Curve Fitting Toolbox version: 9.6.0,1047502 (R2019a)*, 2019.

[76] The Mathworks, Inc., Natick, Massachusetts. *MATLAB Optimization Toolbox version: 9.6.0,1047502 (R2019a)*, 2019.

[77] The Mathworks, Inc., Natick, Massachusetts. *Simulink version: 9.3*, 2019.

[78] B. Meersman, B. Renders, L. Degroote, T. Vandoorn, and L. Vandevelde. Three-phase inverter-connected DG-units and voltage unbalance. *Electric Power Systems Research*, 81(4):899–906, 2011.

[79] A. H. Mohsenian-Rad and A. Leon-Garcia. Optimal residential load control with price prediction in real-time electricity pricing environments. *IEEE Transactions on Smart Grid*, 1(2):120–133, 2010.

[80] V. I. Norkin, G. C. Pflug, and A. Ruszczyński. A branch and bound method for stochastic global optimization. *Mathematical programming*, 83(1):425–450, 1998.

[81] D. M. Olsson and L. S. Nelson. The Nelder-Mead simplex procedure for function minimization. *Technometrics*, 17(1):45–51, 1975.

[82] M. J. Ortega, J. C. Hernández, and O. G. García. Measurement and assessment of power quality characteristics for photovoltaic systems: harmonics, flicker, unbalance, and slow voltage variations. *Electric Power Systems Research*, 96:23–35, 2013.

[83] S. Panchal, M. Mathew, R. Fraser, and M. Fowler. Electrochemical thermal modeling and experimental measurements of 18650 cylindrical lithium-ion battery during discharge cycle for an ev. *Applied Thermal Engineering*, 135:123–132, 2018.

[84] M. C. . Paz, R. G. Ferraz, A. S. Bretas, and R. C. Leborgne. System unbalance and fault impedance effect on faulted distribution networks. *Computers & Mathematics with Applications*, 60(4):1105–1114, 2010.

[85] L. Pierrat and J. P. Meyer. Unbalance factor it is as simple as ABC. *Revue Générale de l'Électricité*, 1(6):18–26, 1987.

[86] P. Pillay and M. Manyage. Definitions of voltage unbalance. *IEEE Power Engineering Review*, 21(5):50–51, 2001.

[87] B. Pongrácz, G. Szederkényi, and K. M. Hangos. An algorithm for determining a class of invariants in quasi-polynomial systems. *Computer Physics Communications*, 175:204–211, 2006.

[88] A. Purvins, H. Wilkening, G. Fulli, E. Tzimas, G. Celli, S. Mocci, F. Pilo, and S. Tedde. A European supergrid for renewable energy: local impacts and far-reaching challenges. *Journal of Cleaner Production*, page doi:10.1016/j.jclepro.2011.07.003, 2011.

[89] E. M. G. Rodrigues, R. Godina, E. Pouresmaeil, J. R. Ferreira, and J. P. S. Catalão. Domestic appliances energy optimization with model predictive control. *Energy Conversion and Management*, 142:402–413, 2017.

[90] M. Savaghebi, A. Jalilian, J. C. Vasquez, and J. M. Guerrero. Secondary control scheme for voltage unbalance compensation in an islanded droop-controlled microgrid. *IEEE Transactions on Smart Grid*, 3(2):797–807, 2012.

[91] L. H. Saw, K. Somasundaram, Y. Ye, and A. A. O. Tay. Electro-thermal analysis of lithium iron phosphate battery for electric vehicles. *Journal of Power Sources*, 249:231–238, 2014.

[92] C. Scherer and S. Weiland. *Linear Matrix Inequalities in Control.* DISC, http://www.er.ele.tue.nl/sweiland/lmi.pdf, 2000.

[93] T. Schné, Sz. Jaskó, and Gy. Simon. Embeddable adaptive model predictive refrigerator control for cost-efficient and sustainable operation. *Journal of Cleaner Production*, 190:496–507, 2018.

[94] S. K. A. Shezan, S. Julai, M. A. Kibria, K. R. Ullah, R. Saidur, W. T. Chong, and R. K. Akikur. Performance analysis of an off-grid wind-PV (photovoltaic)-diesel-battery hybrid energy system feasible for remote areas. *Journal of Cleaner Production*, 125:121–132, 2016.

[95] K. Shimomachi, R. Hara, H. Kita, M. Noritake, H. Hoshi, and K. Hirose. Development of energy management system for dc microgrid for office building:-day ahead operation scheduling considering weather scenarios. In *Power Systems Computation Conference (PSCC), 2014*, pages 1–6. IEEE, 2014.

[96] A. Siddique, G. S. Yadava, and B. Singh. Effects of voltage unbalance on induction motors. In *Conference Record of the 2004 IEEE International Symposium on Electrical Insulation*, pages 26–29. IEEE, 2004.

[97] A. K. Singh, G. K. Singh, and R. Mitra. Some observations on definitions of voltage unbalance. In *2007 39th North American Power Symposium*, pages 473–479. IEEE, 2007.

[98] D. R. Smith, H. R. Braunstein, and J. D. Borst. Voltage unbalance in 3-and 4-wire delta secondary systems. *IEEE Transactions on Power Delivery*, 3(2):733–741, 1988.

[99] EPEX Spot. Market data. *System price.[Verkkotietokanta][Viitattu 23.11. 2011] Saatavissa: http://www. nordpoolspot. com/Market-data1/Elspot/Area-Prices/ALL1/Hourly/http://www. nordpoolspot. com/Market-data1/Elspot/Area-Prices/ALL1/Hourly*, 2010.

[100] Y. Takeuchi. *Global Dynamical Properties of Lotka-Volterra Systems*. World Scientific, Singapore, 1996.

[101] M. Tianhu, B. Jumpei, and I. Yumiko. Analysis of microgrid contributing to hour-ahead market operation through marginal day-ahead market price-based demand response. *Energy Procedia*, 118:119–127, 2017.

[102] J. Toyoda and H. Saitoh. Proposal of an open-electric-energy-network (OEEN) to realize cooperative operations of IOU and IPP. In *Proceedings of EMPD '98. 1998 International Conference on Energy Management and Power Delivery (Cat. No.98EX137)*. IEEE.

[103] O. Tremblay and L. A. Dessaint. Experimental validation of a battery dynamic model for EV applications. *World Electric Vehicle Journal*, 3(1):1–10, 2009.

[104] O. Tremblay, L. A. Dessaint, and A. I. Dekkiche. A generic battery model for the dynamic simulation of hybrid electric vehicles. In *Vehicle Power and Propulsion Conference, 2007. VPPC 2007. IEEE*, pages 284–289. Ieee, 2007.

[105] B. H. Tsai. Modelling energy consumption and carbon dioxide emissions of fossil fuels and nuclear energy using lotka-volterra equations. *Applied Ecology and Environmental Research*, 20(2):1435–1455, 2022.

[106] H.D. Tuan, P. Apkarian, and Y. Nakashima. A new Lagrangian dual global optimization algorithm for solving bilinear matrix inequalities. *International Journal of Robust and Nonlinear Control*, 10:561–578, 2000.

[107] J.G. VanAntwerp and R.D. Braatz. A tutorial on linear and bilinear matrix inequalities. *Journal of Process Control*, 10:363–385, 2000.

[108] M. Vidyasagar. *Nonlinear systems analysis*. Prentice Hall, 1993.

[109] V. Volterra. Variazioni flultuazioni del numero d'invididui in specie convirenti. *Men Acad Lincei*, 2:31–113, 1926.

[110] A. Von Jouanne and B. Banerjee. Assessment of voltage unbalance. *IEEE Transactions on Power Delivery*, 16(4):782–790, 2001.

[111] A. von Meier. *Electric power systems: a conceptual introduction*. John Wiley & Sons, 2006.

[112] Q. Wang, Bin Jiang, Bo Li, and Yuying Yan. A critical review of thermal management models and solutions of lithium-ion batteries for the development of pure electric vehicles. *Renewable and Sustainable Energy Reviews*, 64:106–128, 2016.

[113] Y. J. Wang. An analytical study on steady-state performance of an induction motor connected to unbalanced three-phase voltage. In *2000 IEEE Power Engineering Society Winter Meeting. Conference Proceedings (Cat. No. 00CH37077)*, volume 1, pages 159–164. IEEE, 2000.

[114] Y. J. Wang. Analysis of effects of three-phase voltage unbalance on induction motors with emphasis on the angle of the complex voltage unbalance factor. *IEEE Transactions on energy conversion*, 16(3):270–275, 2001.

[115] H. Wen, D. Cheng, Z. Teng, S. Guo, and F. Li. Approximate algorithm for fast calculating voltage unbalance factor of three-phase power system. *IEEE Transactions on Industrial Informatics*, 10(3):1799–1805, 2014.

[116] Y. Ye, Y. Shi, N. Cai, J. Lee, and X. He. Electro-thermal modeling and experimental validation for lithium ion battery. *Journal of Power Sources*, 199(0):227–238, 2012.

[117] D. Zhang, S. Dey, H. E. Perez, and S. J. Moura. Real-time capacity estimation of lithium-ion batteries utilizing thermal dynamics. *IEEE Transactions on Control Systems Technology*, 2019.

[118] R. Zhang, B. Xia, B. Li, L. Cao, Y. Lai, W. Zheng, H. Wang, W. Wang, and M. Wang. A study on the open circuit voltage and state of charge characterization of high capacity lithium-ion battery under different temperature. *Energies*, 11(9):2408, 2018.

Publications of the author related to the thesis

[119] I. G. Balázs, A. Fodor, and A. Magyar. Quantification of the flexibility of residential prosumers. *Energies*, 14(16):4860, aug 2021.

[120] R. Bálint, A. Fodor, K. M. Hangos, and A. Magyar. Cost-optimal model predictive scheduling of freezers. *Control Engineering Practice*, 80:61–69, nov 2018.

[121] R. Bálint, K. M. Hangos, and A. Magyar. Optimal scheduling of a household refrigerator using adaptive model predictive technique. 19th International Symposium on Power Electronics 2017, Novi Sad, Serbia, October 2017. IEEE.

[122] R. Bálint and A. Magyar. Refrigerator optimal scheduling to minimize the cost of operation. *Hungarian Journal of Industry and Chemistry*, 44(2):99–104, 2016.

[123] R. Bálint, A. Magyar, and K. M. Hangos. Cost-optimal model predictive scheduling of home appliances. *IFAC PapersOnline*, 50(1):3344–3349, 2017.

[124] A. Göllei, P. Görbe, and A. Magyar. Modeling and optimization of electrical vehicle batteries in complex clean energy systems. *Journal of Cleaner Production*, 34:138–145, oct 2012.

[125] P. Görbe, A. Fodor, A. Magyar, and K. M. Hangos. Experimental study of the nonlinear distortion caused by domestic power plants. *Applied Thermal Engineering*, 70(2):1288–1293, 2014.

[126] P. Görbe, A. Magyar, and P. Csuti. Power quality management of led light sources in frequency domain. *Chemical Engineering Transactions*, 35:1309–1314, 2013.

[127] P. Görbe, A. Magyar, and K. M. Hangos. Line conditioning with grid synchronized inverter's power injection of renewable sources in nonlinear distorted mains. In *10th International PhD Workshop on Systems and Control, Hluboka nad Vltavou, Czech Republic*, pages 1–6, ISBN:978-80-903834-3-2, 2009. ISBN:978-80-903834-3-2.

[128] P. Görbe, A. Magyar, and K. M. Hangos. THD reduction with grid synchronized inverter's power injection of renewable sources. In *20th International Symposium on Power Electronics, Electrical Drives, Automation and Motion (SPEEDAM)*, pages 1381–1386, ISBN:978-1-4244-7919-1, 2010.

[129] P. Görbe, A. Magyar, and K. M. Hangos. Reduction of power losses with smart grids fueled with renewable sources and applying EV batteries. *Journal of Cleaner Production*, 34:125–137, 2012.

[130] Gy. Károlyi, A. I. Pózna, K. M. Hangos, and A. Magyar. An optimized fuzzy controlled charging system for lithium-ion batteries using a genetic algorithm. *Energies*, 15(2):481, jan 2022.

[131] A. Magyar, G. Szederkényi, and K. M. Hangos. Quadratic stability of process systems in generalized Lotka-Volterra form. In *Proceedings of 6th IFAC Symposium on Nonlinear Control (NOLCOS 2004), Stuttgart, Germany*, 2003. http://www.nolcos2004.uni-stuttgart.de.

[132] A. Magyar, G. Szederkényi, and K. M. Hangos. Quasi-polynomial system representation for the analysis and control of nonlinear systems. In *Proceedings of 16th IFAC World Congress, Prague, Czech Republic*, 2005. on CD.

[133] A. Magyar, G. Szederkényi, and K. M. Hangos. Globally stabilizing feedback control of process systems in generalized Lotka-Volterra form. *Journal of Process Control*, 2007.

[134] L. Márton, K. M. Hangos, and A. Magyar. Passivity of Lotka-Volterra and quasi-polynomial systems. *Nonlinearity*, 34(4):1880–1899, feb 2021.

[135] L. Neukirchner, A. Göllei, P. Görbe, and A. Magyar. Carbon footprint reduction via voltage asymmetry compensation of three-phase low voltage grid utilizing small domestic power plants. *Chemical Engineering Transactions*, 45:283–288, 2015.

[136] L. Neukirchner, A. Göllei, P. Görbe, and A. Magyar. Voltage unbalance reduction of a local transformer area with domestic asymmetrical inverter and optimal control design. *Int. J. of Thermal & Environmental Engineering*, 12(2):129–134, 2016.

[137] L. Neukirchner, P. Görbe, and A. Magyar. Examination of different voltage asymmetry norms under transient behavior of three-phase low voltage power systems containing small domestic power plants. In *PowerTech, 2015 IEEE Eindhoven*, pages 1–6. IEEE, 2015.

[138] L. Neukirchner, P. Görbe, and A. Magyar. Voltage unbalance reduction in the domestic distribution area using asymmetric inverters. *Journal of Cleaner Production*, 142:1710–1720, 2017.

[139] L. Neukirchner and A. Magyar. Quasi-polynomial representation-based control of mechanical systems. *Hungarian Journal of Industry and Chemistry*, 42(2):91–95, 2014.

[140] Görbe P., Magyar A., Fodor A., and Hangos K. M. Effect of domestic power plants to the low voltage transformer areas from the nonlinear distortion point of view. *Chemical Engineering Transactions*, 35:1303–1308, 2013.

[141] A. I. Pózna, K. M. Hangos, and A. Magyar. Design of experiments for battery aging estimation. *IFAC-PapersOnLine*, 51(28):386–391, 2018.

[142] A. I. Pózna, K. M. Hangos, and A. Magyar. Temperature dependent parameter estimation of electrical vehicle batteries. *Energies*, 12(19):3755, sep 2019.

[143] A. I. Pózna, A. Magyar, and K. M. Hangos. Model identification and parameter estimation of lithium ion batteries for diagnostic purposes. In *2017 International Symposium on Power Electronics (Ee 2017)*, pages 1–6, Oct 2017.

[144] G. Szederkényi, K. M. Hangos, and A. Magyar. On the time-reparametrization of quasi-polynomial systems. *Physics Letters A*, 334(4):288–294, jan 2005.

[145] G. Szederkényi, A. Magyar, and K. M. Hangos. *Analysis and control of polynomial dynamic models with biological applications*. Academic Press, 2018.